# STUDY OF
# OPTICAL FIBER GRATING SENSORS FABRICATED
# BY FEMTOSECOND LASER PULSES

**LIAO CHANGRUI**

**Ph.D**

**The Hong Kong Polytechnic University**

**2012**

The Hong Kong Polytechnic University

Department of Electrical Engineering

# STUDY OF OPTICAL FIBER GRATING SENSORS FABRICATED BY FEMTOSECOND LASER PULSES

LIAO Changrui

A thesis submitted in partial fulfillment of the requirements for the degree of Doctor of Philosophy

April, 2011

# CERTIFICATE OF ORIGINALITY

I hereby declare that this thesis is my own work and that, to the best of my knowledge and belief, it reproduces no material previously published or written, nor material that has been accepted for the award of any other degree or diploma, except where due acknowledgement has been made in the text.

_____ (Signed)

LIAO Changrui (Name of Student)

# Abstract

This thesis investigates the optical fiber grating sensors fabricated by use of femtosecond (fs) laser pulse irradiation. Three types of optical fibers have been used in the investigation, i.e. single mode fiber (SMF), photonic crystal fiber (PCF) and micro and nano optical fiber (MNF). For a high temperature sensor use, fiber Bragg gratings (FBGs) written in $H_2$-free and $H_2$-loaded SMF by use of IR fs radiation with a phase mask have been presented. Type II-IR FBGs fabricated in $H_2$-free and $H_2$-loaded SMFs can both sustain long-term annealing at 1000℃ while their high reflectivity is maintained.

Temporal thermal response of the FBGs has been investigated theoretically and experimentally. A fast testing system is developed to measure the thermal response time by means of periodic $CO_2$ laser irradiation. Temporal thermal response is independent of the heating power and the heating direction. The measured value of the temporal thermal response is ~240ms for heating and ~280ms for cooling. The simulation result based on lumped system equation is in good agreement with the experimental data.

All solid photonic bandgap fiber (AS-PBGF) is an optical fiber that confines the light to the fiber core by the photonic bandgap of the cladding material. FBGs have been successfully inscribed in such fiber by IR fs radiation and two reflection peaks are obtained due to dual core-mode guidance. Long period fiber gratings (LPGs) have also been inscribed in this fiber by use of fs laser with line-scanning method. The coupling from fundamental core mode to $LP_{11}$ core mode is readily obtained and the resonant wavelength is highly sensitive to tensile strain but nearly insensitive or

only slightly sensitive to temperature, curvature, and external RI.

FBG has been successfully fabricated in microfiber (MF) by IR fs radiation. The FBG can be directly exposed to the surrounding medium without etching treatment and shows a high RI sensitivity. It demonstrates a number of propagation modes in the transmission spectrum and higher-order mode shows a higher sensitivity. Another RI sensor has been developed by twisting a pair of MFs to form a coupler. Transmission spectrum of the device is highly sensitive to surrounding RI. The highest sensitivity obtained is 2377nm/RIU at 1.3680 for 4.2μm-diameter MFs and sensitivity is increased up to 2735nm/RIU for a smaller fiber diameter of ~2.8μm.

A multi-parameter (RI and temperature) fiber sensor has been developed by embedding a Mach-Zehnder interferometer (MZI) in an FBG. The compact fiber in-line MZI is fabricated in SMF by IR fs laser ablation. The RI sensitivity of 9148nm/RIU is obtained between 1.30 and 1.325, and temperature sensitivity achieved is 12pm/$^{o}$C ranging from 30 to 90$^{o}$C.

# Acknowledgement

First of all, I would like to express my sincere gratitude to my supervisor Dr. D. N. Wang for giving me the precious opportunity to research in this fascinating area and for his invaluable supervision and encouragement throughout the whole period of my research in the Hong Kong Polytechnic University. He has set for me a high standard of clarify of thinking and expression and I know the skills will always serve me well in the years to come.

I would like to acknowledge Dr. Yuhua Li from Huazhong University of Science and Technology. Without her help and recommendation, I can't get this precious chance to pursue my PhD in Hong Kong. I own many thanks to my colleagues in Fiber Optics Laboratory for their kindly collaboration and technical support.

Most of all, I want to express my gratitude to my family. Thanks to my wife Xu Lei for her thoughtful kindness and continuous support. Thanks to my parents for giving me life and their unconditional encouragement and support makes me come this far. Dear my father, may you rest in peace.

# Contents

# List of Figures

# List of Tables

# Chapter 1

# Introduction

## 1.1 Research Motivation and Contributions

Femtosecond (fs) laser micromachining was first demonstrated on silica and silver surface in 1994. Now fs laser micromachining has been widely used in photonic-device fabrication on transparent materials with the resolution of surface ablation being in nanometer order. Bulk glasses and crystals have high purity and large transparent window so that they are usually used as base materials. A wide variety of fs laser micromachined devices have been reported in glasses and crystals including waveguides, active devices, filters and resonators. Optical fiber, which is one of the most important components in optical communication system and fiber sensor system, is usually constructed by transparent glass material and makes a good guidance of light in the core. Thus optical fiber should be a perfect machining base and the photonic devices achieved in optical fiber are compactable with other optical fiber system. However the study of fs laser micromachining on optical fibers is still in the initial stage.

Fiber Bragg grating （FBG） is a very popular optical component in the field of optical networks, wavelength-division-multiplexing systems and optical fiber sensor system due to their high optical quality, relative ease of fabrication, fiber compatibility and low cost. However, conventional FBGs are usually fabricated by using ultraviolet (UV) laser irradiation which requires photosensitivity of the core material, and thermal stability of the UV laser induced FBGs is also poor. Recently

fs laser technology is exploited to write FBGs in optical fiber without requirement of photosensitivity and the achieved gratings shows great thermal stability. The fs laser inscribed FBGs are thus found to be a promising candidate in ultrahigh temperature sensing applications.

All solid photonic bandgap fiber (AS-PBGF) is a new type of optical fiber in which the air holes of a solid core index guiding photonic crystal fiber (PCF) are filled with the material which has larger RI than that of the background material. These fibers offer unique properties for investigating nonlinear propagation effects, active device applications and novel fiber components but sensing is a relatively unexplored area. The all-solid fiber structure brings a lot of convenience in fiber grating inscription because of no air-hole cladding scattering of light. Therefore it is meaningful job to investigate the fiber gratings fabricated on this fiber including FBG and long period fiber grating (LPG) by use of fs laser irradiation and their sensing property.

There has been recent interest in the fabrication of optical micro and nano fibers (MNFs) and in their applications in optical devices. Comparing with the lithographically fabricated waveguides, such MNFs have smaller loss for a given index contrast and potential ability of micro-assemblage in 3D. Therefore, MNF-based devices are much more compact than those fabricated by lithographic technology. Currently, the study of MNF-based devices is still in the initial stage. Fs laser technology, as an ultra-precision machining tool, would provide great convenience for the development of MNF devices.

The main contributions made during the author’s PhD study are summarized as follow:

- The morphology and thermal stability of a series of FBGs fabricated by use of fs

laser pulse radiation of $H_2$-free and $H_2$-loaded single mode fibers (SMFs) have been investigated. The results are highly relevant to the use of such gratings, for example they are useful in the development of new and better FBG-based sensor devices by allowing the selection of the optimum writing conditions to create gratings for the application required.

- Temporal thermal response of Type II-IR FBG has been investigated both theoretically and experimentally. The temporal thermal response is found to be independent of the heating power and the heating direction, although the grating produced destroys the axial symmetry of the fiber. The measured value of the temporal thermal response is ~240 ms for heating and ~280 ms for cooling.

- Both FBG and LPG have been successfully inscribed in AS-PBGF by use of fs laser radiation. There are two reflection peaks in the reflection spectrum of FBG due to dual core-mode guidance. The LPG based on coupling from $LP_{01}$ core mode to $LP_{11}$ core mode is highly sensitive to tensile strain while being nearly insensitive or only slightly sensitive to temperature, curvature and external refractive index (RI).

- FBGs have been firstly fabricated in microfibers (MFs) by fs laser radiation. The gratings may have a number of propagation modes in their transmission spectrum, depending on fiber diameter, and higher-order mode has a higher RI sensitivity. Moreover, the RI sensitivity is inversely proportional to fiber diameter. The maximum sensitivity obtained is ~231.4nm/RIU at the RI value of 1.44 when MF diameter is ~2 μm.

- A novel RI sensor based on a pair of twisted silica MFs has been proposed and

achieved in experiment. The RI change of the surrounding medium can be measured by wavelength shift of transmission spectrum. The highest sensitivity obtained for the MFs with a diameter of ~4.2μm is 2377 nm/RIU at the RI value of 1.3680. A further sensitivity improvement to 2735 nm/RIU can be obtained when the diameter of MF is reduced to ~2.8μm.

- A dual-parameter fiber sensor based on a Mach-Zehnder interferometer (MZI) embedded in an FBG is proposed and experimentally demonstrated for simultaneous RI and temperature measurement. The interesting properties of the sensor include good operation linearity, extremely high RI sensitivity up to 9148nm/RIU in the RI range between 1.30 and 1.325 and precise sensing location that is determined by the created MZI cavity.

## 1.2 Thesis Outline

It is the author's intention that this dissertation be readable for the audience that has a general knowledge in the filed of physics and optics. The fundamentals of fs laser technique, FBG and MF are therefore reviewed along with a short introduction of their recent research progress in chapter 2.

**Chapter 3** The fabrication of FBG in SMF by use of fs laser irradiation through a phase mask is introduced in Section 3.1. The morphology characteristics of the fabricated FBGs are investigated in Section 3.2. Short-term and long-term annealing tests are implemented to study their thermal stability in Section 3.3. In Section 3.4 temporal thermal response of Type II-IR FBG is investigated experimentally and theoretically. Finally, a summary of Chapter 3 is presented in Section 3.5.

**Chapter 4** Operation principle of AS-PBGF is presented in Section 4.1. Then a

quarter mode is constructed for the AS-PBGF in the commercial FEM software to study its mode property in Section 4.2. An FBG is inscribed in AS-PBGF by use of fs laser radiation together with its spectral property being discussed in Section 4.3. Following a LPG is fabricated in this fiber by use of fs laser with line-scanning method. We test its response to tensile strain, temperature, curvature and external RI respectively in Section 4.4. Finally, a summary of Chapter 4 is presented in Section 4.5.

**Chapter 5** In Section 5.1 FBGs are inscribed in MFs for RI sensing and the sensing performance is investigated. In Section 5.2 we report another novel RI sensor which is constructed based on two twisted MFs and the RI measurement is also demonstrated in this part. Finally, a summary of Chapter 5 is presented in Section 5.3.

**Chapter 6** Operation principle of the multi-parameter sensor based on a MZI embedded in an FBG is illustrated in Section 6.1. The fabrication details including inscription of FBG and drilling of MZI cavity are described in Section 6.2. Simultaneous measurement of RI and temperature is experimentally demonstrated in Section 6.3. Finally, a summary of Chapter 6 is presented in Section 6.4.

**Chapter 7** In the last chapter, we summarize the research work accomplished in this dissertation.

## 1.3 Publications

*Journal Papers*

1. **Changrui Liao**, Dongning Wang, Xiaoying He, MinWei Yang, “Twisted optical micro/nanofibers for refractive index sensing,” IEEE Photon. Technol. Lett., vol. 23 no. 13, pp. 848-850, 2011.
2. **C. R. Liao**, Ying Wang, D. N. Wang, M. W. Yang, “Fiber In-Line Mach-Zehnder Interferometer Embedded in FBG for Simultaneous Refractive index and Temperature Measurement,” IEEE Photon. Technol. Lett., vol. 22 no. 22, pp. 1686-1688, 2010.
3. **Changrui Liao**, Ying Wang, D. N. Wang, Long Jin, “Femtosecond Laser inscribed Long-Period Gratings in All-Solid Photonic Bandgap Fibers,” IEEE Photon. Technol. Lett., vol.22 no.6, pp.425-427, 2010.
4. **Changrui Liao**, Yuhua Li, D. N. Wang, Tong Sun, K. T. V. Grattan, “Morphology and Thermal Stability of Fiber Bragg Gratings for Sensor Applications Written in $H_2$-Free and $H_2$-Loaded Fibers by Femtosecond Laser,” IEEE Sensors Journal, vol.10 no.11, pp.1675-1681, 2010.
5. **Changrui Liao**, Dong-ning Wang, Yuhua Li, Tong Sun, Kenneth. T. V. Grattan, “Temporal thermal response of Type II-IR fiber Bragg gratings,” Appl. Opt., vol.48 no.16, pp.3001-3007, 2009.
6. Ying Wang, **C. R. Liao**, D. N. Wang, “Femtosecond laser-assisted selective infiltration of microstructures optical fibers,” Opt. Express, vol.18, issue.17, pp. 18056-18060, 2010.
7. X. Fang, **C. R. Liao**, D. N. Wang, “Femtosecond laser fabricated fiber Bragg grating in microfiber for refractive index sensing,” Opt. Lett., vol.35, no.7, pp.1007-1009, 2010.
8. Yuhua Li, **C. R. Liao**, D. N. Wang, T. Sun, K. T. V. Grattan, “Study of

spectral and annealing properties of fiber Bragg gratings written in $H_2$-free and $H_2$-loaded fibers by use of femtosecond laser pulses," Opt. Express, vol.16, no.26, pp. 21239-21247, 2008.

9. Xia Fang, X. Y. He, **C. R. Liao**, Minwei, Yang, D. N. Wang, Ying Wang, "A new method for sampled fiber Bragg grating fabrication by use of both femtosecond laser and $CO_2$ laser," Opt. Express, vol.18, no.3, pp. 2646-2654, 2010.
10. Ying Wang, Yuhua Li, **Changrui Liao**, D. N. Wang, Minwei Yang, Peixiang Lu, "High-temperature sensing using miniaturized fiber in-line Mach-Zehnder interferometer," IEEE Photon. Technol. Lett., vol.22 no.1, pp.39-41, 2010.
11. Y. H. Li, M. W. Yang, **C. R. Liao**, D. N. Wang, J. Lu, and Peixiang Lu, "Prestressed fiber Bragg grating with high temperature stability," IEEE J. Lightwave Technol.vol. 29, no. 10, pp. 1555-1559, 2010.
12. Xiaoying He, Xia Fang, **Changrui Liao**, D. N. Wang, Junqiang Sun, "A tunable and switchable single-longitudinal-mode dual-wavelength fiber laser with a simple linear cavity," Optics Express, vol.17, no.24, pp.21773-21781, 2009.
13. X. Y. He, D. N. Wang, **C. R. Liao**, "Tunable and Switchable Dual-Wavelength Single-Longitudinal-Mode Erbium-Doped Fiber Lasers," IEEE J. Lightwave Technol. vol.29, no.6, pp.842-849, 2011.
14. Minwei Yang, D. N. Wang, Ying Wang, **Changrui Liao**, "Long period fiber grating formed by periodically structures microholes in all-solid photonic bandgap fiber," Optics Express, vol.18, no.3, pp.2183-2188, 2010.
15. M. W. Yang, D. N. Wang, Y. Wang, **C. R. Liao,** "Fiber in-line Mach-Zehnder interferometer constructed by selective infiltration of two air holes in photonic crystal fiber," Opt. Lett., vol.36, no.5, pp.636-638, 2011.

16. Shujing Liu, Long Jin, Wei Jin, Dongning Wang, **Changrui Liao**, Ying Wang, "Structural long period gratings made by drilling micro-holes in photonic crystal fibers with a femtosecond infrared laser," Optics Express, vol.18, no.6, pp.5496-5503, 2010.

*Conference Papers*

17. **Changrui Liao**, Dongning Wang, Xiaoying He and Minwei Yang, "Twisted optical microfiber for refractive index sensing," 7753-293, 21st International Conference on Optical Fiber Sensors (OFS'21), Ottawa, Canada, 2011.
18. **C. R. Liao**, Ying Wang, D. N. Wang, Minwei Yang, "Multi-parameter sensor using fiber in-line MZ interferometer embedded in fiber Bragg grating," pp. 7653 10 1-4, Proc. SPIE, vol. 7653, The Fourth European Workshop on Optical Fibre Sensors (EWOFS'4), Porto, Portugal, 2010.
19. **C. R. Liao**, X. Fang, D. N. Wang, "Femtosecond laser induced microfiber Bragg grating for refractive index sensing," pp. 7653 1Z 1-4, Proc. SPIE, vol. 7653, The Fourth European Workshop on Optical Fibre Sensors (EWOFS'4), Porto, Portugal, 2010.
20. Xiaoying He, **Changrui Liao**, Yuhua Li, D. N. Wang, "Tunable Dual-wavelength Erbium-Doped Fiber Ring Laser with Chirped Fiber Bragg Sagnac Loop," The 15th Optoelectronics and Communications Conference (OECC'15), Sapporo, Japan, pp. 310-311, 2010.
21. Yuhua Li, **Changrui Liao**, D. N. Wang, J. Lu, Peixiang Lu, "Fiber Bragg grating for high temperature applications," The 15th Optoelectronics and Communications Conference (OECC'15), Sapporo, Japan, pp. 808-809, 2010.
22. Wei Hong, Dongning Wang, Dingshan Gao, Yuhua Li, **Changrui Liao**, Ying Wang, Shujing Liu, Xia Fang, Lina Ma, "Investigation on transmission properties of a single mode fiber with a cross-sectional micro-channel using

time-domain finite difference (FDTD) method," The 14th Optoelectronics and Communications Conference (OECC'14), Hong Kong, China, pp. ThLP51 1-2, 2009.

23. Shujing Liu, Wei Jin, Long Jin, D. N. Wang, **Changrui Liao**, Ying Wang, "Fabrication of long-period fiber gratings by using of a femtosecond laser source," The 14th Optoelectronics and Communications Conference (OECC'14), Hong Kong, China, pp. WQ6 1-2, 2009.

# Chapter 2

# Background Review

In this chapter, we are going to review fs laser technique, fiber grating and MNF, which are research focuses of this dissertation. The basic principles together with their main properties and the related research progress will be reviewed one by one.

## 2.1 Femtosecond Laser Technique

### 2.1.1 Development of Femtosecond Laser Technique

The generation of fs laser pulses is the greatest breakthrough in the field of laser technique at the end of $20^{th}$ century. Ultrashort pulse duration allows fast temporal resolution, high pulse repetition rate and high peak intensity that provides us new experimental methods and extreme physical environment. Study of fs laser is becoming the frontiers of science and technology all over the world.

In 1981, it is the first time in Bell lab to achieve optical pulses shorter than 0.1ps by colliding pulse mode locking (CPM) in dye laser [1]. In 1987, the scientists in the same group got the optical pulses to 6fs by using cubic phase compensation technique in dye laser [2]. However, the complicated structure of dye laser makes it be in poor operation and large size that limits this technique to be used in practice.

In 1980's the appearance of many solid-state laser crystals makes great promotion of ultrashort laser technique. Ti:Sapphire ($Ti:Al_2O_3$) crystal is an

attractive gain medium for laser operation in the near-infrared spectral region. Its broad gain bandwidth means that in addition to a large tuning range it is especially well suited to ultrashort pulse generation and amplification. Comparing with dye laser, the laser based on Ti:Sapphire crystal owns much wide emission bandwidth, simple structure, high beam quality and good reliability.

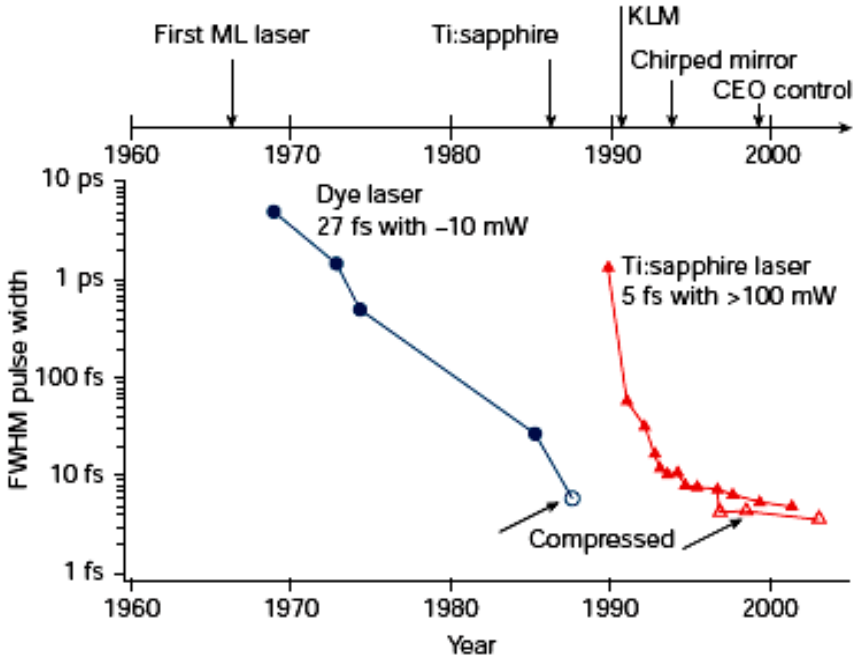


Fig. 2.1 Development of ultrashort optical pulses technique over time.

In the early time of the research in Ti:Sapphire laser, fs optical pulses were generated by using different mode locking methods such as synchronously pumped mode-locking [3], passive mode-locking [4], linear external cavity mode-locking [5], colliding-pulse mode-locking [6] et al. In 1991, D. E. Spence et al. used intracavity dispersion compensation in a mode-locked Ti:Sapphire laser to produce pulse durations as short as 60fs and peak powers of90 kW. The mode locking mechanism is realized due to the Kerr effect of Ti:Sapphire crystal, which is a milestone of ultrashort laser technique [7]. In 1992, Kerr Lens Mode

locking (KLM) theory was raised by Haus in MIT that revealed the mode locking mechanism of Ti:Sapphire laser [8].

KLM allowed the community to shorten pulses to the few fs regime. Because the Kerr lens produces a ‘non-resonant’ saturable absorber, it is inherently broadband, being broader than any other saturable absorber available today. With ultrashort dye lasers, pulses as short as 27fs with around 10mW average power were generated, but pulses around 5-6fs with around 100mW average power can be produced with Ti:Sapphire lasers.

KLM has some significant drawbacks. Generally, KLM lasers are not self-starting, that is, pulse formation does not start by itself, and additional perturbation to briefly increase laser noise is required. This is typically achieved by mechanically ‘shaking’ one of the laser cavity mirrors. The appearance of semiconductor saturable absorbers (SESAMs) [9-11] solved the self-starting problem of KLM lasers and the long-term operation stability of KLM lasers was greatly improved. On the basis of KLM and SESAMs, the performance frontiers of pulsed solid-state lasers have been pushed forward by orders of magnitude during the past decade.

Ultrahigh peak power of laser pulses is another important parameter in some physical researches such as extreme physics, laser controlled thermonuclear fusion reaction and dynamics of semiconductor carriers et al. Chirped pulse amplification (CPA) technique is utilized to amplify an ultrashort laser pulse up to the petawatt level. In CPA, an ultrashort laser pulse is stretched out in time prior to introducing it to gain medium and the stretched pulse whose intensity is sufficiently low, is safely introduced to the gain medium and amplified by a

factor $10^6$ or more. Finally, the amplified laser pulse is recompressed back to the original pulse width through the reversal process of stretching [12]. With the rapid development of CPA technique, the peak power of laser pulse is increasing.

In 1991, A. Sullivan in Univ. Calif. used the technique of CPA in a Ti:Sapphire based oscillator and four-stage amplifier system to produce pulses with a peak power of 3TW, an energy of 0.45J and a pulse width of 95fs [13]. In 1998, K. Yamakawa's group adopted three-stage amplifier to achieve laser pulse output (19fs, 100TW and 10Hz). In recent years, the peak power of amplifier system has increased to be as high as PW (1PW=$10^{15}$W) [14, 15]. The focused intensities delivered over the years by tabletop systems are displayed in Fig. 2.2 [16].

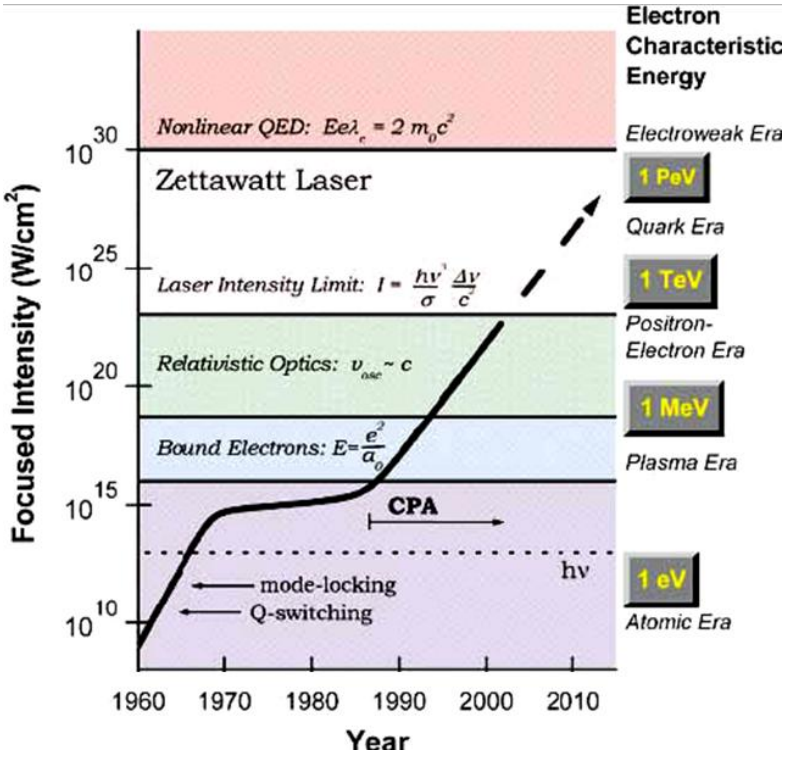


Fig. 2.2 Laser-focused intensity vs years for tabletop systems. [16]

## 2.1.2 Features of Femtosecond Laser Micromachining

Fs laser micromachining is greatly different from long-pulse laser machining. The

ultrahigh laser power is implanted into a small area and the moment accumulation of ultrahigh laser intensity changes the absorption and movement of electrons so as to avoid the negative effects from the occurrence of linear absorption, energy transfer and diffusion in material [17, 18]. The features of fs laser micromachining are summarized as [19]:

1. There is no thermal effect in laser fabrication that leads to no damage to the surrounding material. High machining accuracy and satisfying machining repeatability can be obtained. Many investigations on fs laser micromachining illustrates heat diffusion to surrounding material becomes weaken as pulse duration decreases and therefore heat affected zone is minimized. Due to the rapid energy delivery, the material is heated to be evaporated without material melting so that this fabrication method shows good repeatability.

2. The machining region could be smaller than the focus size of laser beam that consequently overcome the diffraction limit. The structure modification in submicron is achievable. Due to ultrahigh peak power, multiphoton absorption effect makes a leading role in fs laser interaction with material. Fig. 2.3 shows the principle of laser processing with the resolution below the size of the focused laser spot $d_0$. When the laser intensity is kept above the ablation threshold, material modification takes place only in the center of focus beam, where the laser energy density exceeds the intensity of modification threshold. It is possible to conquer optical diffraction limit as long as the laser intensity is well controlled.

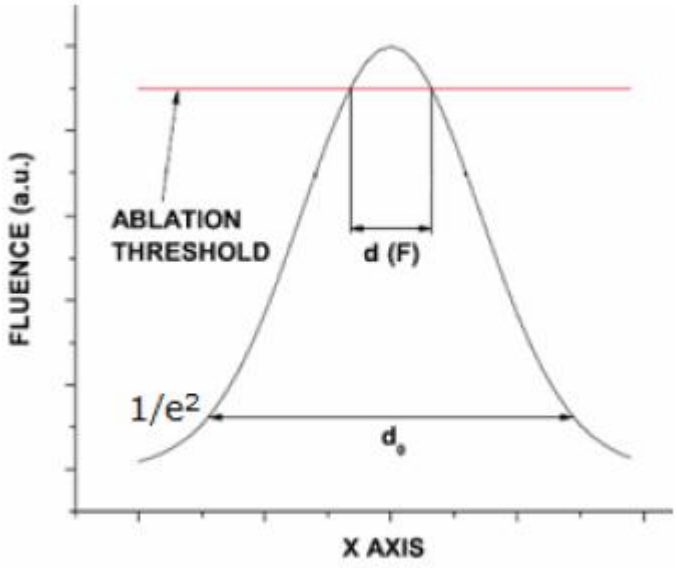


Fig. 2.3 The principle of laser ablation below the diffraction limits.

3. Fs laser micromachining is available for all the materials. The ablation threshold of any material is a definite value based on multiphoton absorption mechanism. As long as laser pulse width is short enough and the peak power is high enough, any material can be manufactured by fs laser including glass, ceramics, dielectrics, semiconductors, polymers and even biological tissues.

## 2.1.3 Femtosecond Laser Fabricated Optical Fiber Devices

Fs laser micromachining has two mechanisms, which are material removal and RI modification. This fabrication is available for both absorptive and transparent materials. Over the past decade, this technique has been widely used in the fabrication of photonic devices in glasses [20-23] and crystals [24-27], including waveguides, active devices, filters and resonators. In this dissertation, silica fiber is the transparent substrate for fs laser micromachining. Prior to introduction of fs laser fabricated glass fiber devices, physical mechanisms underlying the nonlinear interaction of fs laser pulses with glasses are discussed.

When fs laser pulses enter glasses, absorption can take place through nonlinear phenomena, such as multiphoton, tunnelling and avalanche ionization. However the physical mechanisms by which it can induce permanent RI changes in glasses are not yet fully understood. If the absorbed energy is too high, catastrophic material damage occurs, leading to the formation of voidlike structures [28]; for a lower energy, there is a regime where the material maintains its good optical quality, and there are permanent RI changes. There are several mechanisms to explain such change such as colour center formation, thermal effect and direct photostructural change. In practical case, all the mechanisms discussed above play a role in RI change and it is difficult to determine their relative contributions.

Based on the induced RI change, fs laser micromachining is now finding applications in a variety of areas of optical fiber device fabrication. FBGs are the most representative grating device and the FBGs inscribed by fs laser show great superiority. Due to the narrow reflection bandwidth and the low insertion loss, it is widely used in optical communication, optical fiber sensing and fiber lasers. In 2003, the first FBG inscribed by fs laser on standard Ge-doped telecom fiber was achieved in Mihailov's group [29]. The gratings are stable and does not erase after two weeks at 300$^{o}$C. Soon after, direct point-by-point inscription of FBGs by infrared fs laser is reported by Bennion's group and this method requires neither phase mask nor photosensitised fibers and hence offers remarkable technological flexibility [30].

In 2007, Lai *et al*. demonstrated point-by-point inscription of FBG in SMF with the first order Bragg resonances within the C-band using IR fs laser [31]. The structures of the first order and the second order Bragg grating are shown in Fig. 2.4.

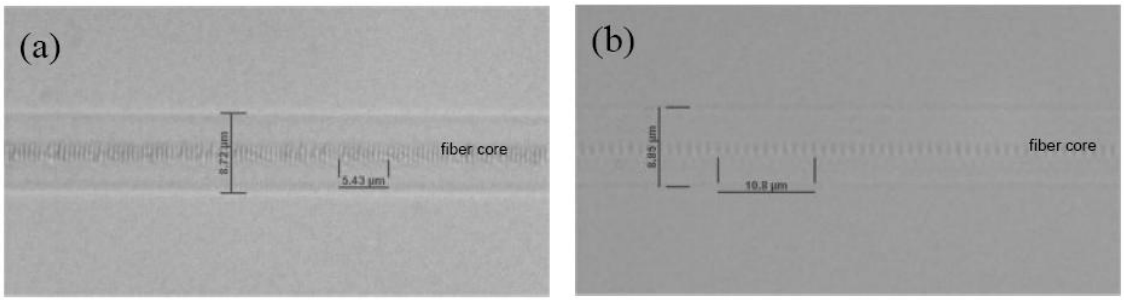


Fig. 2.4 Microscope images of (a) the first order Bragg grating structure and (b) the second order Bragg grating structure inscribed in standard single mode fibers. [31]

Recently, FBGs have been successfully inscribed in different types of optical fibers such as fluoride fibers [32], sapphire fiber [33], rare-earth-doped fibers [34, 35], micro-structured fibers [36-38], and even coated fibers [39]. The sapphire fiber high melting temperature (~2050$^{o}$C) is superior to that of silica fibers, which can be potentially written with FBG to operate up to 2000$^{o}$C [40, 41]. The grating structure is shown in Fig. 2.5.

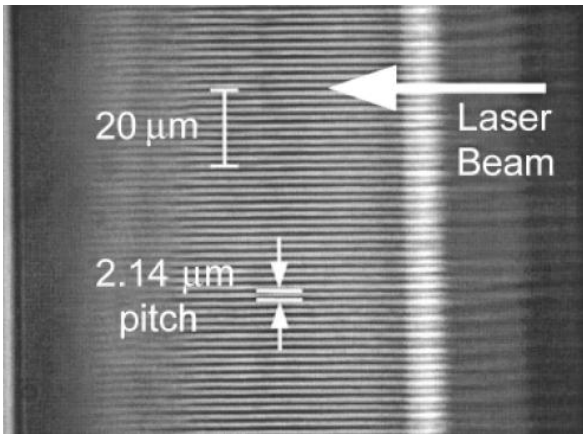


Fig. 2.5 Microscope images of the grating structure written in 150 μm diameter sapphire fiber with 125fs, 800nm laser pulses with a 4.28 μm phase mask. [40]

The holey fiber structure of PCF shows remarkable properties to be usefully employed in both communications and sensing systems. In 2005, fs laser at 267nm was firstly employed by L. B. Fu *et al* to fabricate FBGs in hydrogen-loaded pure-silica PCF [42]. Hydrogen loading did enhance the photosensitivity, possibly by

creating defect-based photosensitivity pathway in bulk silica.

At the end of 2006, Mihailov *et al.* demonstrated the FBG writing in PCF and PCF tapers by the same method [43]. With infrared side exposure of PCF, light scattering by the cladding holes is crucial but this effect can be mitigated by either using fiber geometry with fewer intervening holes between the core and outer surface or tapering the PCF adiabatically and collapsing the holes. In 2007, the same authors demonstrated the fabrication with the same method of high-birefringence FBGs in tapered standard PCF [44]. High-birefringence FBGs are an important element in the area of photonic applications.

An interesting solution to reduce the amount of scattering during FBG writing is to fill the holes with suitable index matching liquid. In 2007, Groothoff *et al*. adopted this method to reduce the scattering to the air barrier and successfully inscribed FBG in $Yb^{3+}$-doped core, co-doped with Al and Ge, air clad fiber with infrared fs laser [45]. The SEM of this air-clad fiber is shown in Fig 2.6(a) with the transmission spectrum shown in Fig. 2.6(b).

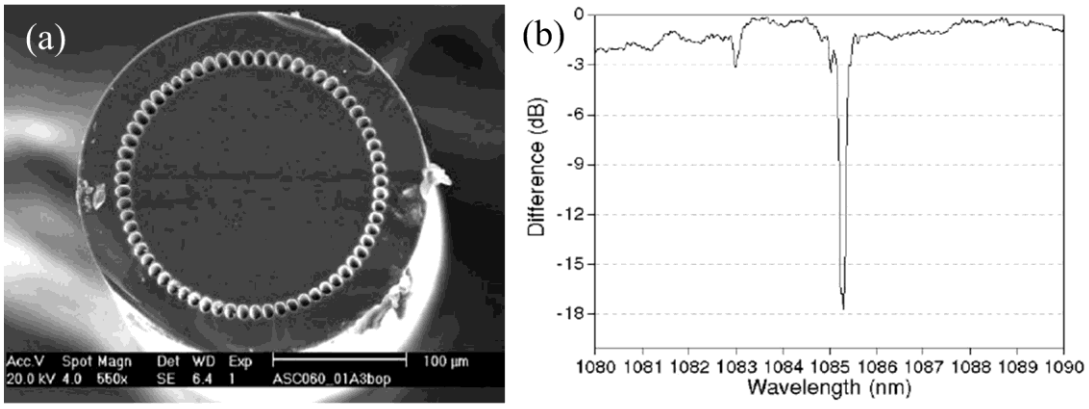


Fig. 2.6 (a) SEM of the air-clad fiber and (b) Transmission spectrum for 2nd order FBG. [45]

Some applications such as fiber lasers and amplifiers require the inscription of FBG in rare-earth doped fibers however a high concentration of photosensitive dopant in these fibers is difficult to achieve. An FBG is firstly inscribed on a nonphotosensitive Er-doped fiber with a transmission loss of -18.9dB at 1554.5nm and a FWHM bandwidth of 0.15nm [46]. The highly reflective FBG (R~98.7%) being a cavity mirror allows efficient laser operation and a high signal-to-noise ratio. The schematic diagram of fiber laser is shown in Fig. 2.7(a) and the spectrum of laser output is demonstrated in Fig. 2.7(b).

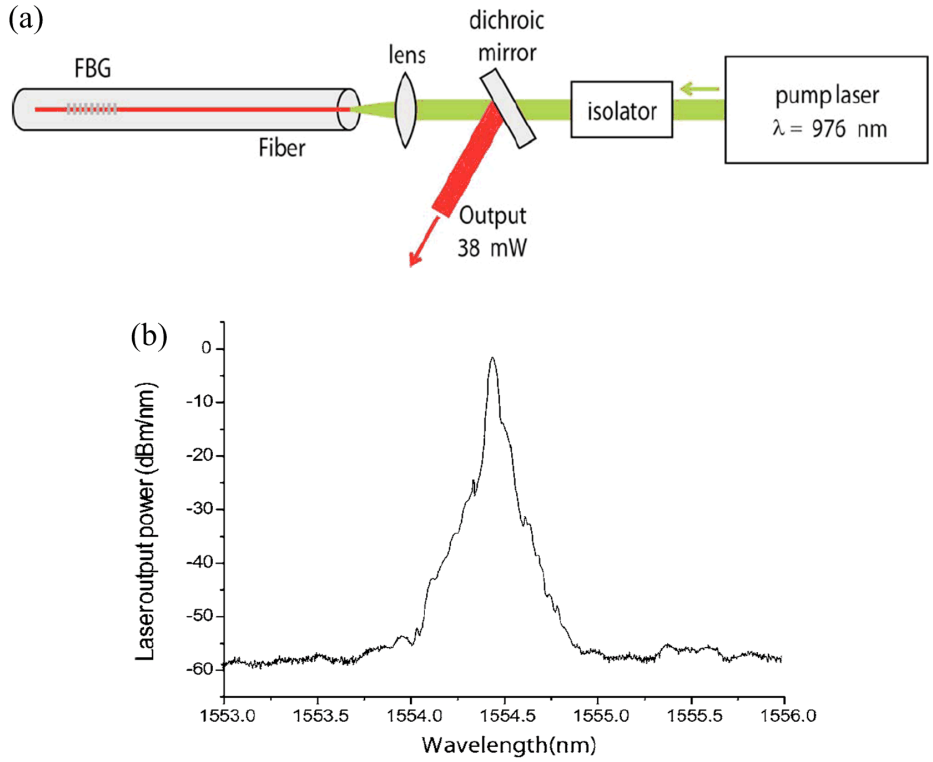


Fig. 2.7 (a) Schematic diagram of fiber laser using a 0.85 m long Er-doped fiber containing the fs-FBG. (b) Spectrum of the laser output at a pump power of 250 mW (output power 26 mW). The laser wavelength corresponds to the grating reflection wavelength. [46]

Besides the inscription of FBGs, fs laser is also widely used to write LPGs of which grating period is approximately 100 to 1000 μm. The grating is usually used as gain-flatting filters for Er-doped amplifiers. The first experimental realization of LPGs

written in SMF *via* focused irradiation of infrared fs laser pulses was carried out by Kondo *et al.* in 1999 and the following annealing test confirmed no degradation of grating performance on temperature from 20 to 500$^{o}$C [47]. Successively, LPGs have been successfully inscribed in the fiber with pure silica core [48] and the near-single-mode $GeO_2$ glass fiber [49] by fs laser inscription. In 2008, Allsop *et al*. reported a series of symmetric and asymmetric LPGs inscribed in photonic crystal fiber (ESM fiber from Crystal Fiber A/S) as directional bend sensors [50]. Due to its all silica structure the sensor owns very low temperature sensitivity, thus reducing cross-sensitivity. In light of the fast growth of photonic crystal fiber and its special structure property, fs laser writing of LPGs are attracting much more attention currently.

Recently, fs laser precise ablation has been developed for wide use of microstructuring and deemed to be one of the most effective approaches to fabricate microstructures into optical fibers. In 2006, Lai *et al.* firstly fabricated microchannels in SMFs by fs laser processing and chemical etching [51]. The etching rate of the laser modified zone is 200 times more susceptible than the unexposed one. The microchannel with the fiber is shown in Fig. 2.8.

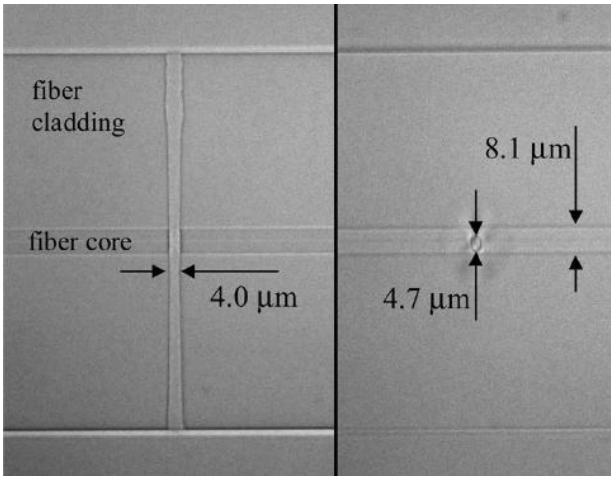


Fig. 2.8 Microscope images of the microchannel within the fiber. [51]

Fs laser fabrication of optical devices can be either destructive or non-destructive. In terms of the destructive fabrication, the laser ablation effect is directly used to sculpture solid materials into the desired 3-D shapes. Destructive fabrication is above the material ablation threshold. Wei *et al.* fabricated a Fabry-Perot cavity with a cavity length of ~ 40 μm and a notch depth of ~ 72 μm by fs laser micromachining in SMF [52]. Fig. 2.9 shows the optical image of the fabricated fiber inline Fabry-Perot cavity.

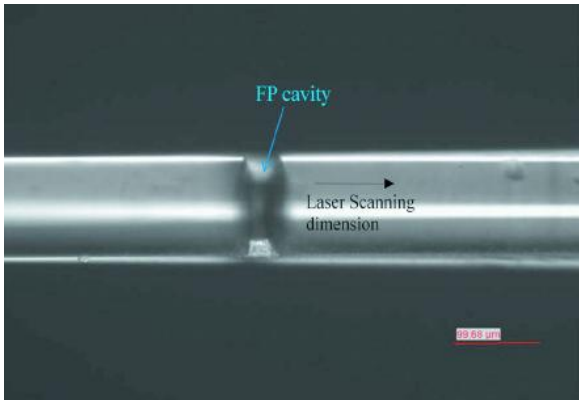


Fig. 2.9 Microscope images of the Fabry-Perot cavity within the fiber. [52]

In 2008, a real complex 3D microcantilever is achieved with a two-step fs laser micromachining process in Said's group [53]. The fabrication procedure is much fast than FIB milling and is easily adaptable for series production. The SEM image of this device is shown in Fig. 2.10.

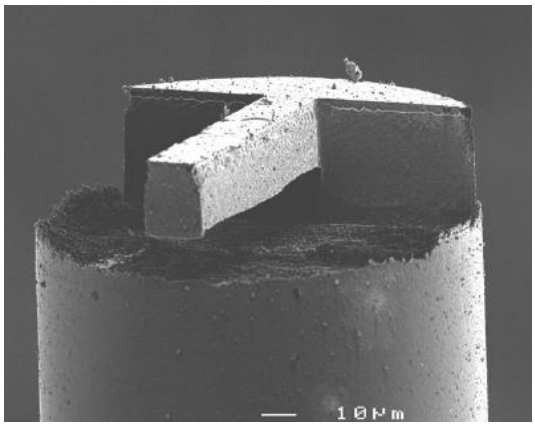


Fig. 2.10 SEM images of a fiber-top microcantilever fabricated by a two-step fs-laser micromachining process. [53]

## 2.2 Fiber Bragg Grating

According to the value of grating period, the optical fiber gratings are classified as FBGs and LPGs. FBGs are a kind of reflection device of which grating period is <1 μm while LPGs are a type of transmission device that has a longer period of being from tens of microns to hundreds of microns. Study of FBGs fabricated by fs laser is one focus of this dissertation. This part briefly reviews the operation principle, fabrication techniques and category of FBGs.

### 2.2.1 Operation Principle

An FBG, in a simplest form, consists of a periodic perturbation of the RI of the core of the optical fiber. This type of uniform FBGs is considered as the fundamental building block for most grating structures. The structure of a uniform FBG has been illustrated in Fig. 2.11.

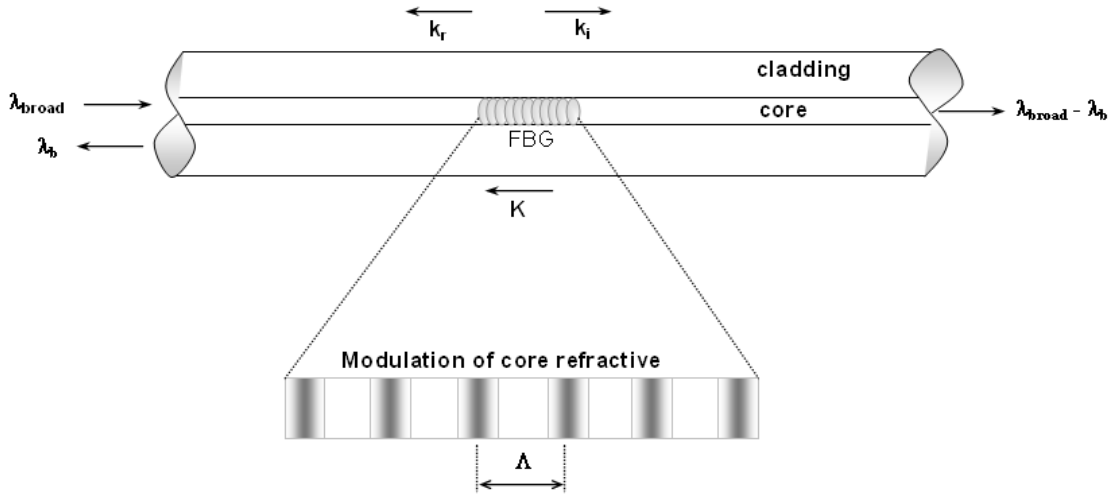


Fig. 2.11 A simple illustration of a uniform FBG.

The guided light along the core of the optical fiber will be scattered by each grating plane (modulated RI region). If a certain phase matching condition, called the Bragg condition (discussed later), is not satisfied, the reflected light from each of the

subsequent grating planes becomes out of phase among them and eventually cancels out. When the Bragg condition is satisfied, the contributions of reflected light from each grating plane will be in-phase and will create a back-reflected peak light component with a centre wavelength defined by the grating parameters. The Bragg condition appears as

$$\lambda_b = 2n_{eff}\Lambda \tag{2.1}$$

where $n_{eff}$ is the effective RI of the fiber core and $\lambda_b$ is the wavelength of the light that back-reflects from the Bragg grating, called as the Bragg wavelength and $\Lambda$ is the spacing between the grating planes.

## 2.2.2 Fabrication Methods

**Interference technique**

The first manufacturing method, specifically used for uniform gratings, is the used of two-beam interference [54, 55]. The UV laser is split into two beams which interfere with each other creating a period intensity distribution along the interference pattern. The RI of the photosensitive fiber changes according to the intensity of light that is exposed to. This method allows for quick and easy changes to the Bragg wavelength by adjusting the incident angle of the laser beam.

**Phase mask technique**

This is one of the most effective techniques for writing fiber gratings which employs a diffractive optical element, called phase mask, for spatially modulating the laser beam to produce the grating [56, 57].

A normal phase mask has a one-dimensional periodic surface-relief structure, with a period of $\Lambda_{PM}$, etched into a high quality fused silica that is transparent to the incident laser. The profile of the periodic surface-relief pattern is so chosen when an

UV light is incident on the phase mask, the zero-order diffracted beam is suppressed to less than few percent (typically less than 3%) of the transmitted optical power and the diffracted plus and minus first orders are maximised (each typically containing more than 35% of the transmitted optical power). The near-field fringe pattern developed by the interference of the diffracted plus and minus first order beams photoimprints a modulation in the RI of the fiber core. A cylindrical lens is used to focus the laser-induced interference fringe pattern along the core. The schematic diagram of this technique is described in Fig. 2.12.

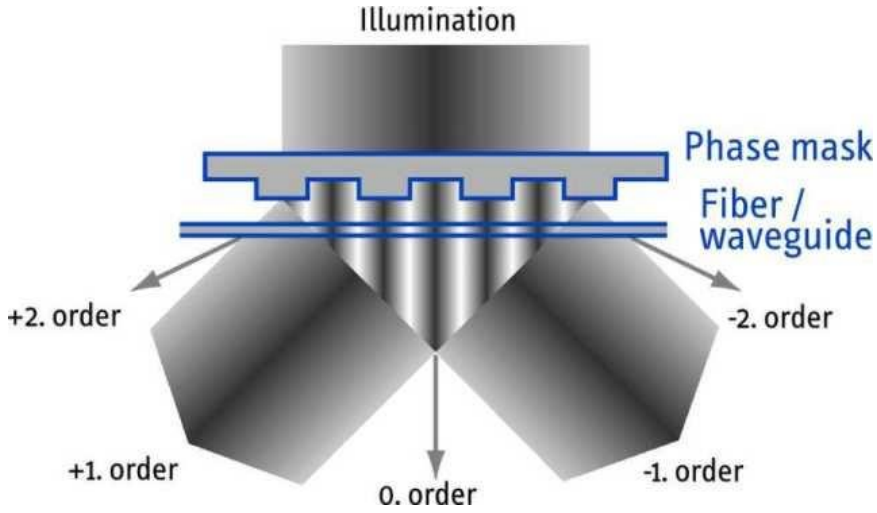


Fig. 2.12. Schematic of fabrication of FBGs using a phase mask.

**Point-by-point technique**

The point-by-point writing method [58] for the fabrication of FBGs can be made possible by inducing a change in the RI of each grating plane, one step at a time, along the length of the fiber core. In a typical experimental arrangement, a single pulse of UV light from an excimer laser passes through a slit and converges onto the core of the fiber, after being focussed through a lens, to modulate the core RI locally. At the same time, the fiber has to be moved along the fiber-axis using a translation stage, with a velocity matching to the frequency of the excimer laser so that each pulse of the UV light produces a grating plane with a desired period. The schematic

of point-by-point fabrication of gratings is described in Fig. 2.13. The main advantage of this method is great flexibility to form gratings of any length and any pitch.

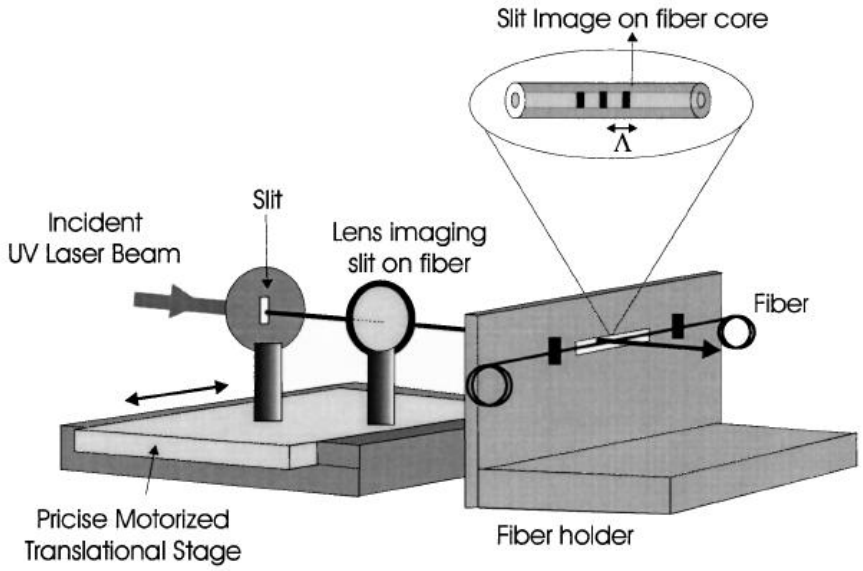


Fig. 2.13. Schematic of point-by-point fabrication of FBGs. [58]

## 2.2.3 Category of Fiber Bragg Gratings

The category method in this context refers to the underlying photosensitivity mechanism by which RI modulation is introduced in fiber. The different fabrication conditions have significant effect on physical attributes of the achieved gratings like thermal stability. Categories of FBGs are summarized as:

**Type I gratings**

These gratings are usually formed in normal photosensitive optical fibers under the irradiation of moderate laser energy. They are formed through what is thought to be colour center formation or densification [59]. Typically, its reflection spectrum is equal to 1-T where T is the transmission spectrum. The reflection and transmission spectra are complementary and there is negligible loss of light by reflection into

cladding or by absorption. These gratings exhibit temperature stability up to 500$^{o}$C before they are rapidly erased that is a consequence of the instability of colour centers at elevated temperatures [60]. Type I FBGs are often used in telecoms, low temperature sensing, biodiagnostics and lasers.

**Type II gratings**

Type II gratings are formed under the single-pulse irradiation of high laser energy. The reflection and transmission spectra of these gratings are not complementary to each other. The short wavelengths are strongly coupled into the fiber cladding. This is known as a damage grating which is produced with laser intensity exceeding the damage threshold of the glass material leading to fracturing, void formation and/or filamentation [59, 61]. Examine of such a grating by an optical microscope shows a significant localised damage track at the core-cladding interface. These FBGs are tested to be extremely thermally stable (can survive up to 800$^{o}$C with no decay in reflectivity) [62]. Type II FBGs can be used in high power fiber laser and ultrahigh temperature sensing.

**Fs-Laser Inscribed FBG**

Fig. 2.14 makes a comparison of the photosensitivity of pure silica and Ge-doped silica. Different mechanisms of index change are explained here. Modification of dielectrics with fs laser pulses is resulting from multi-photon ionization process, where simultaneous absorption of several photons produces a free electron [63]. The nature of multi-photon ionization makes fs laser be able to inscribe FBGs in a broader range of optical fibers than UV writing process. For type I fs laser gratings, these gratings are formed through an intermediate level of electron generation, below that necessary to strong ionize the medium. The induced index change is shown to have temperature stability similar to that of traditional UV type I grating [64] with a

difference which can be explained by different categories of the formed colour centers. Increasing fs laser intensity to a high level ($\sim 4.5\times10^{13} W/cm^2$) there will be a sharp transition into a regime where the material modification appears to result from a damage process similar to what would be expected from a highly ionized absorbing medium. These gratings have similar high temperature stability as the traditional type II grating [64].

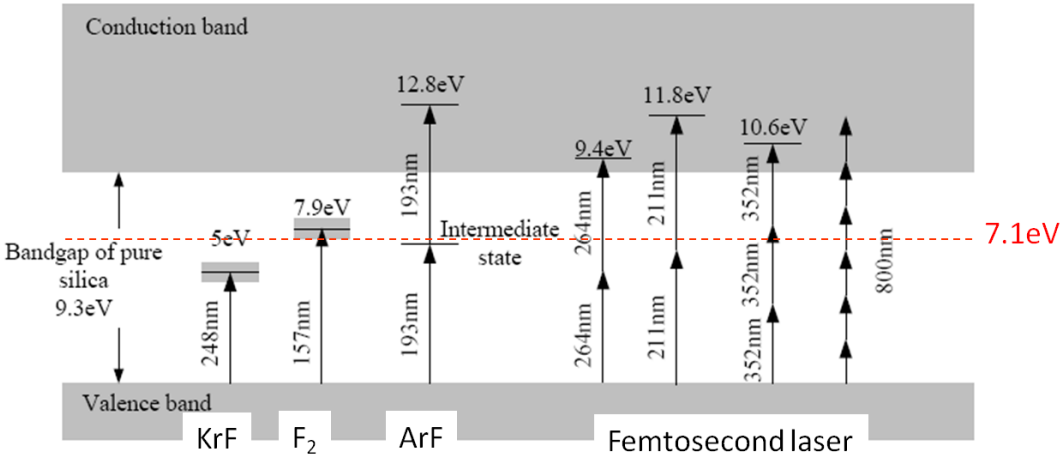


Fig. 2.14. Schematic diagram of photosensitivity of pure silica and Ge-doped silica. The bandgap of index change is lower in Ge-doped silica (7.1eV) comparing with pure silica (9.3eV). The index change can be achieved in the highly Ge-doped silica fiber by 248nm KrF laser irradiation and while the index change is able to be realized in the commercial SMF without special photosensitization by $F_2$ laser irradiation. Two-step photon absorption is employed by 193nm ArF laser to introduce index change in pure silica. Differently, multi-photon absorption takes place in fs-laser interaction with pure silica to induce index change.

# 2.3 Micro and Nano Optical Fiber

## 2.3.1 Device Properties

For tapered MNFs, Ge-doped core is negligible so that the whole tapered fiber can

be considered as the new core and the environment such as air is usually used as cladding. When the core diameter decreases below the light wavelength, a considerable fraction of the light propagates outside the core. In recent years, MNFs have attracted great attention because of their unique optical and mechanical properties, including the following:

**Strong light confinement**

The light can be confined in the very thin fiber over long length; therefore it is easy to observe nonlinear interactions e.g. supercontinuum generation [65, 66] at relatively modest power level.

**Large evanescent field**

A large fraction of light can propagate outside the surface of MNFs, being the evanescent field. This can be exploited for atom guides [67], particle manipulation [68], sensors [69, 70], and high-Q resonators [71-73].

**Great configurability**

MNFs have relatively high-mechanical strength and it can be easily bent to be a radius of the order of a few micrometers. Thus, some compact optical fiber devices e.g. 2D [74] and 3D [75] resonators could be readily achieved.

**Low-loss connection**

MNFs are manufactured by adiabatically stretching optical fibers and they maintain original size at the input and output ends. Therefore it is convenient to connect to the standard fiber by simple splicing. Insertion loss smaller than 0.1dB are commonly observed.

## 2.3.2 Fabrication Methods

To date, the techniques of manufacture of MNFs are well established and three top-down techniques have been developed to manufacture MNFs: a two-step process [76], the "flame-brushing" technique [77, 78] and laser-heated taper drawing a sapphire tube heated by a $CO_2$ laser [79].

In the two-step drawing process [76], the MF with a diameter of several micrometers is tapered using a flame-heated pulling. Then, to obtain a steady condition for the further reduction of the fiber diameter, a tapered sapphire fiber with a tip is chosen to absorb the thermal energy from the flame. When one end of the micrometer-diameter fiber is wound around the sapphire tip at the softening temperature of glass, the sapphire tip is moved about 0.5 mm out of flame to prevent the melting of MF. Applying a certain drawing force perpendicular to the axis of the sapphire tip, the MF is drawn to form the nanowire with a diameter down to 50 nm.

In the "flame-brushing" method [77], hydrogen gas torch is usually used due to its cleanness, easy control and high temperature. The schematic diagram is shown in Fig. 2.15. When the flame is scanning to-and-fro within a certain region of a glass fiber, the axial tension is given by pulling force applied at the sides. So the fiber can be elongated with reduced diameter at the hot zone by taper drawing. By controlling the stretched length of fiber and the length of flame scanning we can obtain the MNFs with the desired length and diameter.

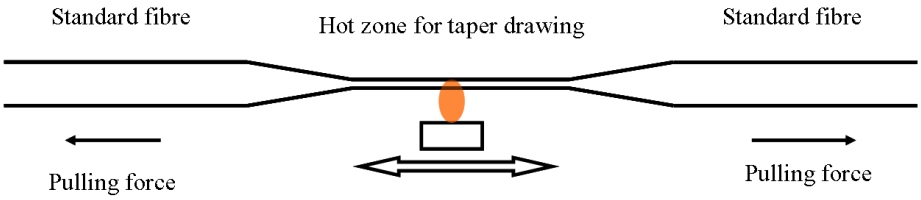


Fig. 2.15. Schematic of flame-heated taper drawing of optical fiber. [77]

Later, a carbon dioxide laser beam is used as a heating source to replace the hydrogen gas torch. This approach can reduce or eliminate the 1380-nm-wavelength

OH absorption in tapered fiber, as well as to avoid contamination and random turbulence-induced non-uniformity of a flame-heated system.

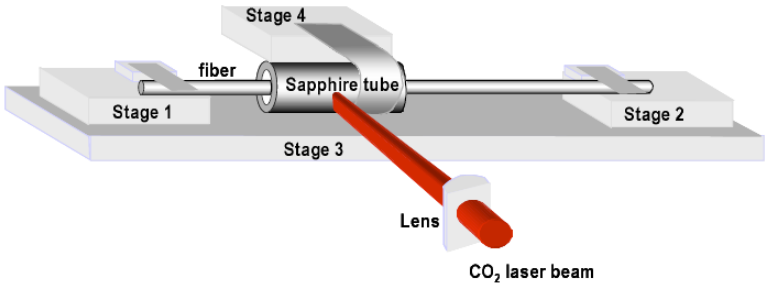


Fig. 2.16. Schematic of drawing MNF using a sapphire tube heated with a CO2 laser. [79]

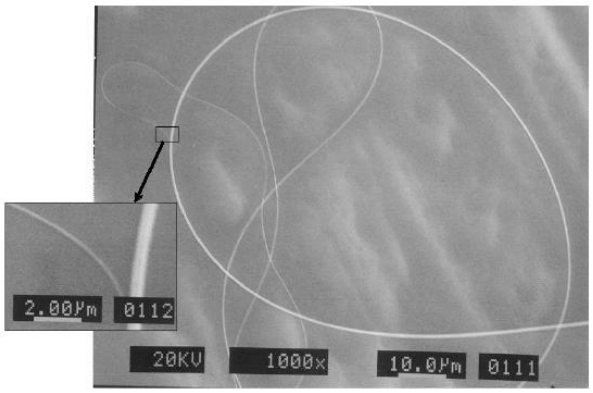


Fig. 2.17. SEM image of the MNF drawn by sapphire tube method. [79]

As we know, drawing of very thin fibers using direct heating by laser beam is impossible because the minimum diameter of fiber is limited by the power of the beam. So an indirect melting of a silica fiber using a laser is developed that requires a sapphire tube heated by a $CO_2$ laser [79]. Fig. 2.16 illustrates a setup of this fabrication method. An optical fiber is placed into the sapphire capillary tube which is heated by a $CO_2$ laser. The size of the tube is chosen depending on the taper parameters. In contrast the fiber taper is much smaller than the mass of the heated section; hence the temperature inside the sapphire tube is not affected by the fiber diameter variation during taper drawing. Fig. 2.17 shows a SEM image of the MNF which is drawn from a regular SMF. The diameter of MNF decreases from 700nm to

less than 100nm.

### 2.3.3 MNF-based Devices

The MNF-based photonic devices have been widely investigated recently. The physically drawn optical MNFs are essentially one good linear waveguide which is one of the simplest optical components for optical circuits and devices. MNF can serve as both free-standing and supported waveguides and Table 2.1 makes a summary of the possible schemes.

Table 2.1. Possible schemes for using an MNF as a linear waveguide.

| Supporting form | Supporting Medium | Examples |
|---|---|---|
| Freestanding | Gas | Air |
| | Liquid | Water |
| Surface support | Nanostructures | Silica aerogel |
| | Solids | $MgF_2$, UV-cured polymer |
| Embedded | Solidification after embedded | UV-cured polymer, CDMS |

Based on the strong evanescent field of MNF, an efficient power coupling takes place within a short interaction length between two MNFs when they come close enough. Fig. 2.18 illustrates a micro-coupler assembled with two tellurite glass MNF which are supported on an $MgF_2$ substrate [80]. The diameters of the two MNFs are 350nm and 450nm, respectively. A 633nm-wavelength light is launched into the bottom left arm and then divides into two with an interaction length of less than 4 μm. Compared with the fused coupler which requires an interaction length of the order of 100 μm, the MNF coupler largely reduces the device size.

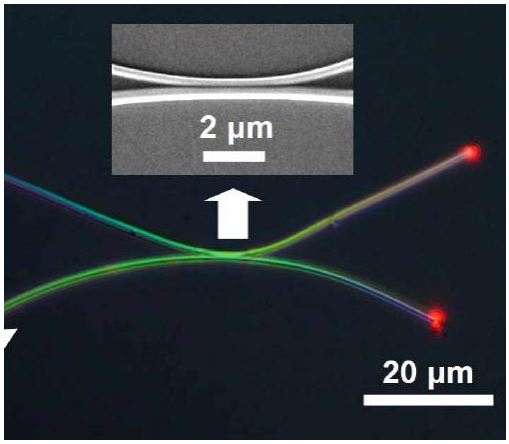


Fig. 2.18. Optical microscope image of a microcoupler assembled with two tellurite glass MNFs on the $MgF_2$ substrate. [80]

The MZI is constructed when two micro-couplers are connected in cascade. Fig. 2.19 shows an optical microscope image of a typical MZI assembled by two silica MNFs with diameter of 1 μm, with a whole dimension of ~300 μm [81]. The two MNFs are placed on a low-index substrate in parallel with a certain length of overlap at two points by using van der Waals force and electrostatic attraction.

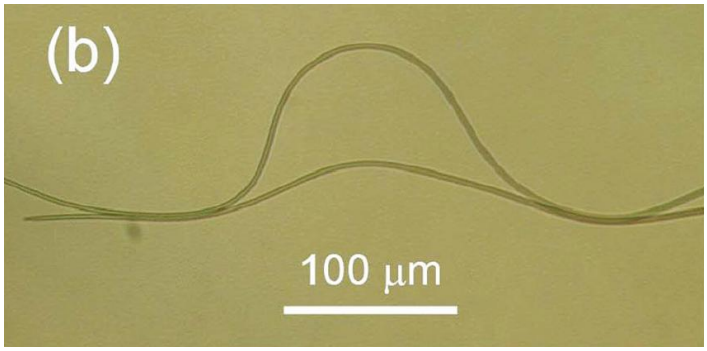


Fig. 2.19. Optical microscope image of a MZI assembled with two silica MNFs. [81]

High-Q resonators are widely studied for their broad range of applications from optical communications to nonlinear optics, and sensing. A simple resonator can be achieved by bending the MNFs into a self-coupling loop. There are two different single-loop resonators which are the loop resonator [72, 75] and the knot resonator [81]. The knot one exhibits an enhanced temporal stability because of the friction

that different sections of the MNF exert on one another.

By using the flame-brushing or the modified flame-brushing technique the MNFs with extremely long lengths can be achieved. Hence, more complicated resonator i.e. coil resonator can be fabricated. The microcoil resonator is a 3D resonator consisting of many self-coupling turns, and it can be created by wrapping an MNF on a low-index dielectric rod [70, 71, 73]. Fig. 2.20 displays a coil resonator by coiling a MNF with diameter of 10 μm on a 1.1mm diameter silica rod [82].

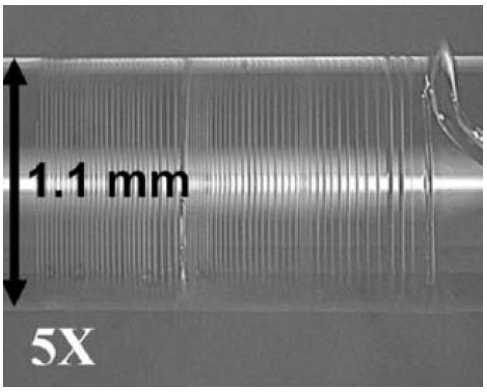


Fig. 2.20. Optical microscope image of an MNF-coil resonator. [82]

Besides the positive optical devices, the MNFs are also used in active devices such as fibre laser. Jiang *et al.* successfully made a 1.5 μm wavelength MF laser formed by tightening a doped MF into a knot in air [83]. The 2-mm-diameter knot that is assembled with a 3.8-μm-dimmeter Er: Yb-doped phosphate glass MF serves as both active medium and the resonating cavity for lasing. Single-longitudinal-mode laser with threshold of about 5mW and output power higher than 8 μW is achieved. Fig. 2.21 shows the schematic diagram of the MF knot laser.

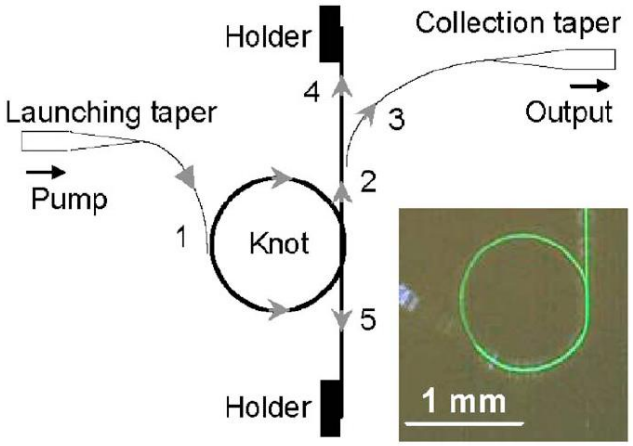


Fig. 2.21 Schematic diagram of the structure of the Er: Yb-doped phosphate glass MF knot laser. [83]

## 2.4 Summary

We presented a brief review of fs laser micromachining, fiber grating and MNF. For fs laser micromachining, we focused on the unique machining mechanism allowing this fabrication method to be provided with ultrahigh accuracy, ultrahigh spatial resolution and “cold” process. Then the research efforts in fs laser micromachining of optical fiber devices are briefly reviewed. Fiber grating and MNF are the main optical components investigated here for sensing applications. With regard to FBG, basic principle is given with different fabrication techniques and grating category based on the thermal stability. The optical and mechanical properties of MNFs are introduced followed by fabrication methods. MNF-based photonic devices in recent years are reviewed in the end.

# Reference

[1] R. L. Fork, B. I. Greene, C. V. Shank, "Generation of optical pulses shorter than 0.1 psec by colliding pulse mode locking," *Appl. Phys. Lett.*, vol. 38, pp. 671-672 (1981).

[2] R. L. Fork, C. H. Brito Cruz, P. C. Becker et al. "Compression of optical pulses to six femtoseconds by using cubic phase compensation," *Opt. Lett.*, vol. 12, pp. 483-485 (1987).

[3] R. Roy, P. A. Schulz, A. Walther, "Acousto-optic modulator as an electronically selectable unidirectional device in a ring laser," *Opt. Lett.*, vol. 12, pp. 672~674 (1987).

[4] N. Sarukura, Y. Ishida, H. Nakano et al. "CW passive mode locking of a Ti:sapphire laser," *Appl. Phys. Lett.*, vol. 56, pp. 814-815 (1990).

[5] P. M. W. French, S. M. J. Kelly, J. R. Taylor, "Mode locking of a continuous-wave titanium-doped sapphire laser using a linear external cavity," *Opt. Lett.*, vol. 15, pp. 378-380 (1990).

[6] K. Naganuma, K. Mogi, "50-fs pulse generation directly fron a colliding-pulse mode-locked Ti:sapphire laser using an antiresonant ring mirror," *Opt. Lett.*, vol. 16, pp. 738-740 (1991).

[7] D. E. Spence, P. N. Kean, W. Sibbett, "60-fsec pulse generation from a self-mode-locked Ti:sapphire laser. *Opt. Lett.*, vol. 16, pp. 42-44 (1991).

[8] H. A. Haus, J. g. Fujimoto, E. P. Ippen, "Structures for additive pulse mode locking," *J. Opt. Soc. Am. B*, vol. 8, pp. 2068-2076 (1991).

[9] I. D. Jung, F. X. Kärtner, N. Matuschek et al. "Self-starting 6.5-fs pulses from a Ti:saphhire laser," *Opt. Lett.*, vol. 22, pp. 1009-1011 (1997).

[10] D. H. Sutter, G. Steinmeyer, L. Gallmann et al. "Semiconductor saturable-absorber mirror-assisted Kerr-lens mode-locked Ti:sapphire laser producing pulses in the two-cycle regime," *Opt. Lett.*, vol. 24, pp. 631-633 (1999).

[11] V. L. Kalashnikov, D. O. Krimer, I. G. Poloyko, "Soliton generation and picosecond collapse in solid-state lasers with semiconductor saturable absorbers," *J. Opt. Soc. Am. B*, vol. 17, pp. 519-523 (2000).

[12] D. Strickland, G. Mourou, "Compression of amplified chirped optical pulses," *Opt. Commun.*, vol. 56, pp. 219-221 (1985).

[13] A. Sullivan, H. Hamster, H. C. Kapteyn et al, "Multiterawatt, 100-fs laser," *Opt. Lett.*, vol. 16, pp. 1406-1408 (1991).

[14] V. V. Lozhkarev, K. Yamakawa, Y. Akahane et al, "0.85-PW, 33-fs Ti:sapphire laser," *Opt. Lett.*, vol. 28, pp. 1594-1596 (2003).

[15] M. Martinez, E. Gaul, T. Ditmire et al, "The Texas Petawatt Laser," *Proc. Of SPIE*, 5991: 59911N (2005).

[16] T. Tajima, G. Mourou, "Zettawatt-exawatt lasers and their applications in ultrastrong-field physics," *Phys. Rev. Special Topics-Accelerators and Beams*, vol. 5, pp. 031301 (2002).

[17] J. R. Goldman, J. A. Prybyla, "Ultrafast Dynamics of Laser-Excited Electron Distribution in Silicon," *Phy. Rev. Lett.*, vol. 72, pp. 1364-1367 (1994).

[18] D. Von der Linde, K. Sokolowski-Tinten, J. Bialkowski, "Laser-solid interaction in the femtosecond time regime," *Appl. Surface Sci.*, vol. 109/110, pp. 1-10 (1997).

[19] X. Liu, D. Du, G. Mourou, "Laser ablation and micromachining with ultrashort laser pulses," *IEEE J. Quantum Electron.*, vol. 33, pp. 1706-1716 (1997).

[20] K. Hirao, K. Miura, "Writing waveguides and gratings in silica and related materials by a femtosecond laser," *J. Non-Cryst. Solids* vol. 239, pp. 91-95, (1998).

[21] J. W. Chan, T. R. Huser, S. H. Risbud, J. S. Hayden, and D. M. Krol, "Waveguide fabrication in phosphate glasses using femtosecond laser

pulses," *Appl. Phys. Lett.* vol. 82, pp. 2371-2373, (2003).

[22] V. R. Bhardwaj, E. Simova, P. B Corkum, D. M. Rayner, C. Hnatovsky, R. S. Taylor, B. Schreder, M. Kluge, J. Zimmer, "Femtosecond laser-induced refractive index modification in multicomponent glasses," *J. Appl. Phys.* vol. 97, pp. 083102, (2005).

[23] A. Zoubir, M. Richardson, C. Rivero, A. Schulte, C. Lopez, K. Richardson, N. Ho, and R. Vallee, "Direct femtosecond laser writing of waveguides in As2S3 thin films" *Opt. Lett.* vol. 29, pp. 748-750, (2004).

[24] T. Gorelik, M. Will, S. Nolte, A. Tuennermann and U. Glatzel, "Transmission electron microscopy studies of femtosecond laser induced modifications in quartz," *Appl. Phys. A.* vol. 76, pp. 309-311, (2002).

[25] R. R. Thomson, S. Campbell, I. J. Blewett, A. K. Kar and D. T. Reid, "Optical waveguide fabrication in z-cut lithium niobate (LiNbO3) using femtosecond pulses in the low repetition rate regime," *Appl. Phys. Lett.* vol. 88, pp. 111109, (2006).

[26] J. Burghoff, C. Grebing, S. Nolte and A. Tunnermann, "Efficient frequency doubling in femtosecond laser-written waveguides in lithium niobate," *Appl. Phys. Lett.* vol. 89, pp. 081108, (2006).

[27] Amir H. Nejadmalayeri and Peter R. Herman, "Ultrafast laser waveguide writing: lithium niobate and the role of circular polarization and picosecond pulse width," *Opt. Lett.* vol. 31, pp. 2987-2989, (2006).

[28] E. N. Glezer, M. Milosavljevic, L. Huang, R. J. Finlay, T.-H. Her, J. P. Callan, and E. Mazur, "Three-dimensional optical storage inside transparent materials," *Opt. Lett.* vol. 21, pp. 2023-2025, (1996).

[29] S. J. Mihailov, C. W. Smelser, P. Lu, R. B. Walker, D. Grobnic, H. Ding, G. Henderson, "Fiber Bragg grating made with a phase mask and 800-nm femtosecond radiation," *Opt. Lett.* vol. 28, pp. 995-997, (2003).

[30] A. Martinez, M. Dubov, I. Khrushchev, and I. Bennion, “Direct writing of fiber Bragg gratings by femtosecond laser,” *Eletron. Lett.* vol. 40, pp. 1170-1172, (2004).

[31] Y. Lai, K. Zhou, K. Sugden, and I. Bennion, “Point-by-point inscription of first-order fiber Bragg grating for C-band applications,” *Opt. Express*, vol. 15, pp. 18318-18325, (2007).

[32] S. J. Mihailov, C. W. Smelser, D. Grobnic, R. B. Walker, P. Lu, H. M. Ding, J. Unruh, “Bragg graings written in all-$SiO_2$ and Ge-doped core fibers with 800nm femtosecond radiation and a phase mask,” *J. Ligthwave Technol.* vol. 22, pp. 94-100, (2004).

[33] D. Grobnic, S. J. Mihailov, C. W. Smelser, H. M. Ding “Sapphire fiber bragg grating sensor made using femtosecond laser radiation for ultrahigh temperature applications,” *J. Ligthwave Technol.* vol. 16, pp. 2505-2507, (2004).

[34] E. Wikszak, J. Thomas, J. Burghoff, B. Ortac, J. Limpert, S. Nolte, U. Fuchs, and A. Tunnermann, “Erbium fiber laser based on intracore femtosecond-written fiber Bragg grating,” *Opt. Lett.* vol. 16, pp. 2390-2392, (2006).

[35] D. Grobnic, S. J. Mihailov, R. B. Walker, C. W. Smelser, C. Lafond, and A. Croteau, “Bragg gratings made with a femtosecond laser in heavily doped Er-Yb phosphate glass fiber,” *Photon. Technol. Lett.* vol. 19, pp. 943-945, (2007).

[36] L. B. Fu, G. D. Marshall, J. A. Bolger, P. Steinvurzel, E. C. Magi, M. J. Withford, and B. J. Egleton, “Femtosecond laser writing Bragg gratings in pure silica photonic crystal fibers,” *Electron. Lett.* vol. 41, pp. 638-640, (2005).

[37] T. Geernaert, K. Kalli, C. Koutsides, M. Komodromos, T. Nasilowski, W. Urbanczyk, J. Wojcik, F. Berghmans, H. Thienpont, “Point-by-point fiber Bragg grating inscription in free-standing step-index and photonic crystal

fibers using near-IR femtosecond laser," *Opt. Lett.* vol. 35, pp. 1647-1649, (2010).

[38] Y. Wang, H. Bartelt, M. Becker, S. Brueckner, J. Bergmann, J. Kobelke, and M. Rothhardt, "Fiber Bragg grating inscription in pure-silica and Ge-doped photonic crystal fibers," *Appl. Opt.*. vol. 48, pp. 1963-1968, (2009).

[39] A. Martinez, I. Y. Khrushchev, I. Bennion, "Direct inscription of Bragg gratings in coated fibers by an infrared femtosecond laser," *Opt. Lett.* vol. 31, pp. 1603-1605, (2006).

[40] D. Grobnic, S. J. Mihailov, C. W. Smelser, and H. Ding, "Sapphire fiber Bragg grating sensor made using femtosecond laser radiation for ultrahigh temperature applications," *Photon. Technol. Lett.* vol. 16, pp. 2505-2507, (2004)

[41] S. J. Mihailov, D. Grobnic, and C. W. Smelser, "High-temperature multiparameter sensor based on sapphire fiber Bragg gratings," *Opt. Lett.* vol. 35, pp. 2810-2812, (2010).

[42] L. B. Fu, G. D. Marshall, J. A. Bolger, P. Steinvurzel, E. C. Mägi, M. J. Withford, and B. J. Eggleton, "Femtosecond laser writing Bragg gratings in pure silica photonic crystal fibres," *Electron. Lett.* vol. 41, pp. 638-640, (2005).

[43] S. J. Mihailov, D. Grobnic, H. Ding, C. W. Smelser, and J. Broeng, "Femtosecond IR laser fabrication of Bragg gratings in photonic crystal fibers and tapers," *Photon. Technol. Lett.* vol. 18, pp. 1837-1839, (2006).

[44] D. Grobnic, H. Ding, S. J. Mihailov, C. W. Smelser, and J. Broeng, "High birefringence fibre Bragg gratings written in tapered photonic crystal fibre with femtosecond IR radiation," *Electron. Lett.* vol.43, pp. 16-17, (2007).

[45] N. Groothoff, J. Canning, N. Jovanovic, G. D. Marshall, M. J. Withford, "Gratings in large diameter air-clad optical fiber using a femtosecond laser,"

*BGPP*, BWC3, (2007).

[46] E. Wikszak, J. Thomas, J. Burghoff, B. Ortac, J. Limpert, and S. Nolte, "Erbium fiber laser based on intracore femtosecond-written fiber Bragg grating," *Opt. Lett.* vol. 31, pp. 2390-2392, (2006).

[47] Y. Kondo, K. Nouchi, T. Mitsuyu, M. Watanabe, P. G. Kazansky, and K. Hirao, "Fabrication of long-period fiber gratings by focused irradiation of infrared femtosecond laser pusles," *Opt. Lett.* vol. 24, pp. 646-648, (1999).

[48] F. Hindle, E. Fertein, C. Przygodzki, F. Durr, L. Paccou, R. Bocquet, P. Niay, H. G. Limberger, M. Douay, "Inscription of long-period gratings in pure silica and Germano-silicate fiber cores by femtosecond laser irradiation," *Photon. Technol. Lett.* vol. 16, pp. 1861-1863, (2004).

[49] R. Sou, Y. Lai, K. Zhou, L. Zhang, I. Bennion, X. Jiang, J. Lousteau, A. Jha, "Long-period gratings in near-single-mode GeO2 glass fiber by IR femtosecond laser inscription," *BGPP*, pp. BWB5, (2007)

[50] T. Allsop, K. Kalli, K. Zhou, Y. Lai, G. Smith, M. Dubov, D. J. Webb, I. Bennion, "Long period gratings written into a photonic crystal fibre by a femtosecond laser as direction bend sensors," *Opt. Commun.* vol. 281, pp. 5092-5096, (2008).

[51] Y. Lai, K. Zhou, and I. Bennion, "Microchannels in conventional single-mode fibers," *Opt. Lett.* vol. 31, pp. 2559-2561, (2006).

[52] T. Wei, Y. Han, H. L. Tsai, and H. Xiao, "Miniaturized fiber inline Fabry-Perot interferometer fabricated with a femtosecond laser," *Opt. Lett.* vol. 33, pp. 536-538, (2008).

[53] A. A. Said, M. Dugan, S de Man, and D. Iannuzzi, "Carving fiber-top cantilevers with femtsecond laser micromachining," *J. Micromech. Microeng.* vol. 18, pp. 035005, (2008).

[54] G. Meltz, W. W. Morey, W. H. Glenn, "Formation of Bragg grating in optical

fibers by a transverse holographic method," *Opt. Lett.* vol. 14, pp. 823-825, (1989).

[55] M. L. Dockney, J. W. James, and R. P. Tatam, "Fiber Bragg grating fabricated using a wavelength tunable source and a phase-mask based interferometer," *Meas. Sci. Technol.* vol. 7, pp. 445-448, (1996).

[56] K. O. Hill, B. Malo, F. Bilodeau, D. C. Johnson, J. Albert, "Bragg gratings fabricated in monomode photosensitive optical fiber by UV exposure through a phase mask," *Appl. Phys. Lett.* vol. 62, pp. 1035-1037, (1993).

[57] D. Z. Anderson, V. Mizrahi, T. Erdogan, and A. E. White, "Production of in-fibre gratings using a diffractive optical element," *Electron. Lett.* vol. 29, pp. 566-568, (1993).

[58] B. Malo, K. O. Hill, F. Bilodeau, D. C. Johnson, and J. Albert, "Point-by-point fabrication of micro-Bragg gratings in photosensitive fiber using single excimer pulse refractive index modification techniques," *Electron. Lett.* vol. 29, pp. 1668-1669, (1993).

[59] J. Canning, "Fiber gratings and devices for sensors and lasers," Laser Photon. Rev., vol. 2, pp. 275–289 (2008).

[60] B. Malo, J. Albert , D. C. Johnson, F. Bilodeau, K. O. Hill, "Elimination of photoinduced absorption in Ge-doped silica fibres by annealing of ultraviolet colour centres," *Elec. Lett.*, vol. 28, pp. 1598-1599 (1992).

[61] J. L. Archambault, L. Reekie, and P. St. J. Russell, "100% reflectivity Bragg reflectors produced in optical fibers by single excimer laser pulses," *Elec. Lett.*, vol. 29, pp. 453-455 (1993).

[62] J. L. Archambault, L. Reekie, and P. St. J. Russell, "High reflectivity and narrow bandwidth fibre gratings written by single excimer pulse," *Elec. Lett.*, vol. 29, pp. 28-29 (1993).

[63] M. Lenzner, J. Krüger, S. Sartania, Z. Cheng, Ch. Spielman, G. Mourou, W.

Kautek, and F. Krausz, “Femtosecond optical breakdown in dielectrics,” Phys. Rev. Lett. vol.80, pp. 4076-4079 (1998).

[64] C. W. Smelser, S. J. Mihailov, and D. Grobnic, “Formation of Type I-IR and Type II-IR gratings with an ultrafast IR laser and a phase mask,” Opt. Express, vol. 12, pp. 5377-5386 (2005).

[65] S. Leon-Saval, t. Birks, W. Wadsworth, P. St. J. Russell, and M. Mason, “Superconinuum generation in submicron fibre waveguides,” *Opt. Express* vol. 12, pp. 2864-2869 (2004).

[66] M. A. Foster, J. M. Dudley, B. Kibler, Q. Cao, D. Lee, R. Trebino, and A. L. Gaeta, “Nonlinear pulse propagation and supercontinuum generation in photonic nanowires: experiment and simulation,” *Appl. Phys. B* vol. 81, pp. 363-367 (2005).

[67] V. I. Balykin, K. Hakuta, F. Le Kien, J. Q. Liang, and M. Morinaga, “Atom trapping and guiding with a subwavelength-diameter optical fiber,” *Phys. Rev. A* vol. 70, pp. 011401 (2004).

[68] G. Brambilla, G. S. Murugan, J. S. Wilkinson, and D. J. Richardson, “Optical manipulation of microspheres along a subwavelength optical wire,” *Opt. Lett.* vol. 32, pp. 3041-3043 (2007).

[69] J. Villatoro and D. Monzón-Hernández, “Fast detection of hydrogen with nano fiber tapers coated with ultra thin palladium layers,” *Opt. Express* vol. 13, pp. 5087–5092 (2005).

[70] F. Xu, P. Horak, and G. Brambilla, “Optical microfiber coil resonator refractometric sensor,” Opt. Express 15, 7888–7893 (2007). *Opt. Express* vol. 15, pp. 7888-7893 (2007).

[71] M. Sumetsky, “Optical fiber microcoil resonator,” *Opt. Express* vol. 12, pp. 2303–2316 (2004).

[72] M. Sumetsky, Y. Dulashko, and A. Hale, “Fabrication and study of bent and

coiled free silica nanowires: self-coupling microloop optical interferometer," *Opt. Express* vol. 12, pp. 3521–3531 (2004).

[73] F. Xu and G. Brambilla, "Embedding optical microfiber coil resonators in Teflon," *Opt. Lett.* vol. 32, pp. 2164–2166 (2007).

[74] M. Sumetsky, Y. Dulashko, and A. Hale, "Fabrication and study of bent and coiled free silica nanowires: self-coupling microloop optical interferometer," *Opt. Express* vol. 12, pp. 3521-3531 (2004).

[75] M. Sumetsky, Y. Dulashko, J. M. Fini, and A. Hale, "Optical microfiber loop resonator," *Appl. Phys. Lett.* vol. 86, pp. 161108 (2005).

[76] L. M. Tong, R. R. Gattass, J. B. Ashcom, S. L. He, J. Y. Lou, M. Y. Shen, I. Maxwell, and E. Mazur, "Subwavelength-diameter silica wires for low-loss optical wave guiding," *Nature*, vol. 426, pp. 816-819 (2003).

[77] G. Brambilla, V. Finazzi, D. Richardson, ""Ultra-low-loss optical fiber nanotapers," *Opt. Express*, vol. 12, pp. 2258-2263 (2004).

[78] S. Leon-Saval, T. Birks, W. Wadsworth, P. St J Russell, M. Mason, "Supercontinuum generation in submicron fibre waveguides," *Opt. Express*, vol. 12, pp. 2864-2869 (2004).

[79] T. E. Dimmick, G. Kakarantzas, T. A. Birks, P. St. J. Russell, "Carbon dioxide laser fabrication of fused-fiber couplers and tapers," *Appl. Opt.* vol. 38, pp. 6845-6848 (1999).

[80] L. M. Tong, L. Hu, J. Zhang, J. Qiu, Q. Yang, J. Lou, Y. Shen, J. He, and Z. Ye, "Photonic nanowires directly drawn from bulk glasses," *Opt. Express* vol. 14, pp. 82-87 (2006).

[81] Y. Wu, Y. J. Rao, Y. H. Chen, and Y. Gong, "Miniature fiber-optic temperature sensors based on silica/polymer microfiber knot resonators," *Opt. Express* vol. 17, pp. 18142-18147 (2009).

[82] M. Sumetsky, Y. Dulashko, S. Ghalmi, "Fabrication of miniature optical fiber

and microfiber coils," *Opt. Laser Eng.* vol. 48, pp. 272-275 (2010).

[83] X. Jiang, Q. Yang, G. Vienne, Y. Li, L. M. Tong, J. Zhang, L. Hu, "Demonstration of microfiber knot laser," *Appl. Phys. Lett.* vol. 89, pp. 143513 (2006).

# Chapter 3

# High Temperature Sensor based on Femtosecond Laser Inscribed FBG

FBG is now one of the key components in the well established field of optical fiber sensors. Recently, fs laser radiation has been used to write fiber gratings in $H_2$-free fibers [1-6]. The work in this chapter aims to build on that published work and to create a better understanding of the characteristics of gratings designed for high temperature sensors. The morphology, thermal stability and thermal temporal response of the FBGs written by use of a 120 fs IR laser through a phase mask under different fabrication conditions have been investigated.

## 3.1 Fabrication of FBGs in Single Mode Fiber

The experimental setup developed for writing FBGs through the phase mask is shown in Fig. 3.1. The fs laser pulses (120fs, 1mJ, 1kHz repetition rate at λ=800nm) are produced by a Ti: Sapphire CPA laser system (Spectra-Physics). The laser beam is focused onto the fiber core by a cylindrical lens (f = 40mm) through a 1080nm pitched phase mask. For Gaussian beam optics, the radius of the focal spot size would be:

$$\omega \approx \lambda f / \pi\omega_0 \tag{3.1}$$

where $\lambda$ is the wavelength, $f$ is the focal length of the cylindrical lens and $\omega_0$ is the $1/e$ Gaussian beam radius. With $\omega_0$ being 5mm in this experiment, the beam area

at the focus is about $\sim 4.1\times10^{-4} cm^2$. The laser energy is attenuated as required by rotating a half wave-plate followed by a linear polarizer. The fiber used without the polymer coating was fixed behind a phase mask at a distance of ~300μm. The transmission spectra of the FBGs being created were measured in line by using light from a combination of a multi-SLED with a wavelength range from 1270nm to 1620nm (Amonics, CWDM Super-wideband Light Source) and the resulting spectra due to the grating were detected by using an Optical Spectrum Analyzer (OSA) with a resolution of ~0.01nm (Yokogama, AQ6319). After laser inscription, the breakage of the index axial symmetry due to laser irradiation was examined by measuring of the grating spectral PDL. Finally the grating was cleaved in the middle of the grating area to analyze the cross-section morphology by use of an optical microscope (Nikon 80i) with a colour charge-coupled-device (CCD) camera. The microscope was equipped with four objectives (4×, 10×, 20× and 60×) and one 10× eyepiece tube: thus the magnification that can be obtained is from 40 to 600.

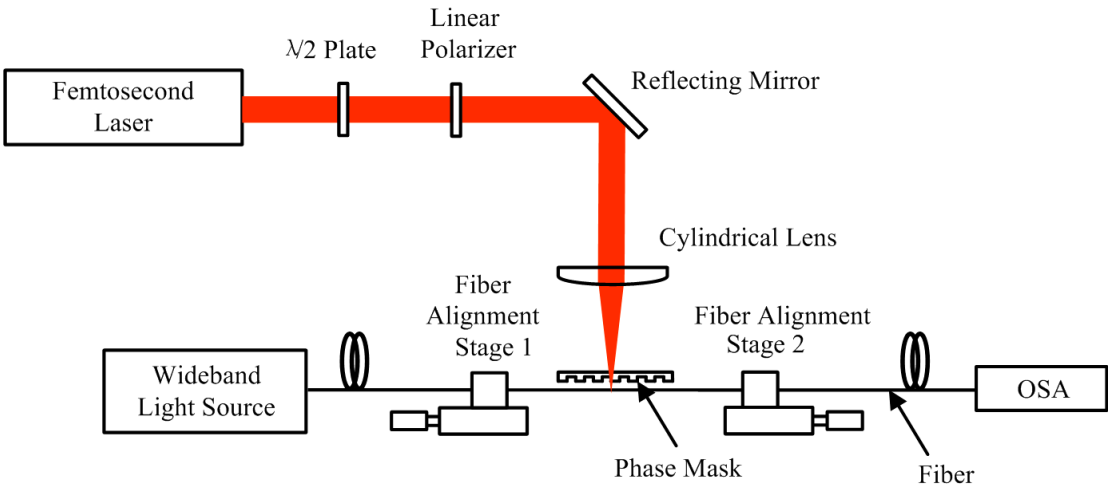


Fig. 3.1 Scheme of experimental setup for inscribing FBGs by using fs laser pulses through a phase-mask.

The following fibers were used in the experiment: 1) pristine Ge-doped telecom SMF-28 fiber; and 2) $H_2$-loaded Ge-doped telecom SMF-28 fiber, where the fiber

was loaded with hydrogen at a pressure of 140bar (~2000psi), at 120$^{o}$C over a period of 96h.

## 3.2 Morphology Characteristics

Type I-IR, type II-IR and the hybrid grating structures have been achieved in both $H_2$-free and $H_2$-loaded SMFs. The hybrid grating containing both type I-IR and type II-IR index change components is firstly observed in IR fs laser inscription. The fabrication condition and the spectral properties of the FBGs are summarized in Table 3.1. More than five samples in each inscription condition are fabricated and analyzed in order to assure the accuracy and repeatability of the results.

Table 3.1 Fabrication condition and spectral property of the FBGs fabricated by 120fs, 800nm laser pulses *via* a phase mask

| Grating Type | Fabrication condition | | | | Spectral property | |
|---|---|---|---|---|---|---|
| | Fiber used | Focusing location | Laser intensity, $10^{12}W/cm^2$ | Exposure dose, $kJ/cm^2$ | Transmission Loss, *dB* | PDL, *dB* |
| Type I | $H_2$-free SMF-28 | core | 8.9 | 1500 | 8.6 | 1.4 |
| Type II | | core | 14.0 | 40 | 15.9 | 3.6 |
| Hybrid | | cladding | 14.0 | 40 | 12.3 | 2.6 |
| Type I | $H_2$-loaded SMF-28 | core | 5.1 | 880 | 20.1 | 0.4 |
| Type II | | core | 13.0 | 37 | 22.4 | 1.8 |
| Hybrid | | cladding | 14.0 | 40 | 21.0 | 2.8 |

The hybrid grating is usually neglected because it cannot be distinguished by viewing the grating spectra. In order to characterize the mechanism for fs laser interaction with the two types of fibers selected, the morphology both along the fiber axis and on the cross section have been directly examined. The material birefringence induced by fs irradiation was examined by measuring the grating spectral PDL, which further revealed the relationship between the grating spectra, the morphology and the thermal stability.

In the case of $H_2$-free SMF-28 fiber, an 8.6dB FBG is inscribed using an intensity of $8.9\times10^{12}W/cm^2$ and an exposure dose of $1500kJ/cm^2$ (30min irradiation time, 1.8 million pulses). Assuming a uniform FBG of 3mm length, the RI modulation in the core is estimated to be $\sim5.7\times10^{-4}$. The background loss is $<0.2dB$. When the pulse energy is increased, a 15.9dB type II FBG is achieved with an intensity of $14.0\times10^{12}W/cm^2$ and an exposure dose of $40kJ/cm^2$ (30s irradiation time, 30000 pulses). The background loss is ~2dB and the index modulation is determined to be $\sim8.7\times10^{-4}$. The spectral properties and the corresponding grating morphology are shown in Fig. 3.2.

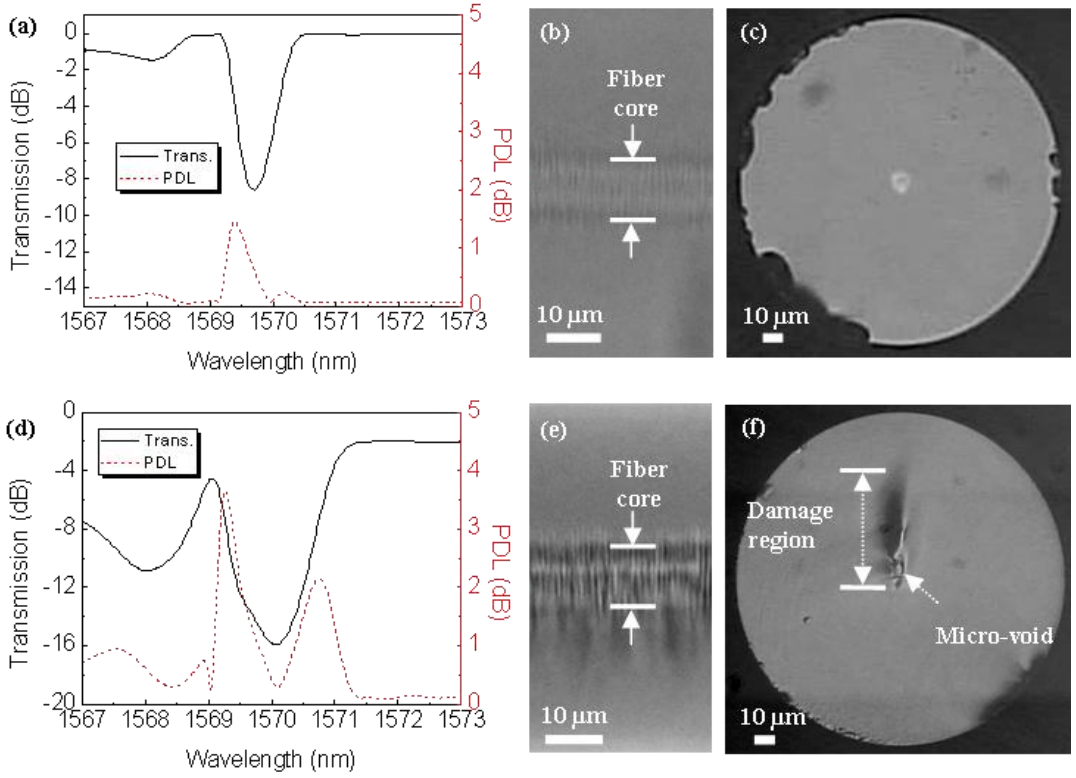


Fig. 3.2 Type I-IR and type II-IR FBG inscribed in $H_2$-free SMF-28 fiber. (a) Transmission spectra and PDL of type I FBG; (b), (c) The axial and cross sectional morphology of Type I-IR FBG; (d) Transmission spectra and PDL of type II-IR FBG; (e), (f) The axial and cross sectional morphology of type II-IR FBG.

Comparing Fig. 3.2 (a) and (d), it can be seen that the transmission spectra of type II-IR FBG show much stronger cladding modes than those of the Type I-IR, although the two gratings do not have the same strength. This phenomenon has been validated in Ref. [7], where, for the same strength as that of Type I-IR, type II-IR FBG exhibited stronger cladding modes. These strong cladding modes are induced by the non-uniform index change across the core which can be clearly observed by comparing the cross sectional morphology in Fig. 3.2 (c) and (f). In Fig. 3.2 (c), the visibility of Type I-IR grating is so poor that the trace of the index change cannot be directly observed by the optical microscope. By immersing the grating in the RI matching liquid ( $n_{ind} = 1.40$ ) the visibility is seen to have improved considerably, as shown in Fig. 3.2 (b). It is found that the grating structure is almost localized in the Ge-doped core, which may result from the highly nonlinear defect formation in the multi-photon absorption process [8].

Type II-IR FBG is a damage grating which involves the following mechanism: firstly, the plasma comes into being through a multi-photon and avalanche photo-ionization process; then, the transfer of the plasma energy to the lattice generates a localized high temperature and pressure which lead to shock waves and densification, i.e. a micro-explosion inside the glass materials [9]. Comparing Figs. 3.2 (b) and 3.2(e), it becomes clear that a much more ‘obvious’ grating structure can be observed under the higher laser intensity exposure. Fig. 3.2 (f) shows that the groove structure induced by the severe laser ablation goes beyond the core and the material modification in the core is highly disordered, being quite analogous to the birefringence zone of type II damage [10]. It is followed by a single track of tens-of-micron length which may be due to the Rayleigh range for the focused beam ( $Z_R = \pi\omega^2 / \lambda \approx 70\mu m$ ). The non-uniformity ‘damaged’ index change between the core and the cladding enhances the high cladding-mode coupling and thus introduces

a larger wavelength-independent scattering loss. At the same time a large PDL of ~3.6dB is also achieved.

The spectral PDL comes from two sources: the intrinsic birefringence of the fiber and the birefringence in the laser induced index modulation [11]. For $H_2$-free fiber, the induced birefringence by the IR laser plays a leading role. In Fig. 3.2 (d) the bandwidth of PDL peak on the short wavelength side is broader than that of the PDL peak on the longer wavelength side; thus the laser-induced index change is predicted to be negative based on the simulation result between the spectral PDL of an FBG and the sign of induced index in Ref. [12]. The reason may be the formation of micro-voids in the core of the index change filled with a vacuum of air ($n_{ind}=1$), this being shown in Fig. 3.2 (f).

When fs laser beam was not focused on the core but on the cladding, the Bragg effect can still take place where the incident laser intensity was sufficiently high. The FBG obtained is a hybrid structure including both type I-IR and type II-IR components. Such a 12.3-dB ($\Delta n_{ind}=7.2\times10^{-4}$) FBG was fabricated in the $H_2$-free SMF-28 fiber with an intensity of $14.0\times10^{12}W/cm^2$ and an exposure dose of $40kJ/cm^2$ (30s irradiation time, 30000 pulses). The background loss is $<0.2dB$. Fig. 3.3 demonstrates the spectral properties and the corresponding morphology of this hybrid FBG.

In Fig. 3.3 (c), the cross sectional morphology gives a clear evidence of the hybrid structure. The crack indicating damage (type II-IR component) is located in the cladding, followed by a less visible line (type I-IR component) across the core. The type I index component which is located in the core region might be formed because

of the reduced pulse energy following the laser beam defocusing in the core. The spectral property of the hybrid FBG is similar to that of the pure Type I-IR discussed above like weak cladding mode coupling. However, the PDL is increased to some extent, this being ~2.6dB. It is believed that the type I-IR index change plays a major role in this type of gratings.

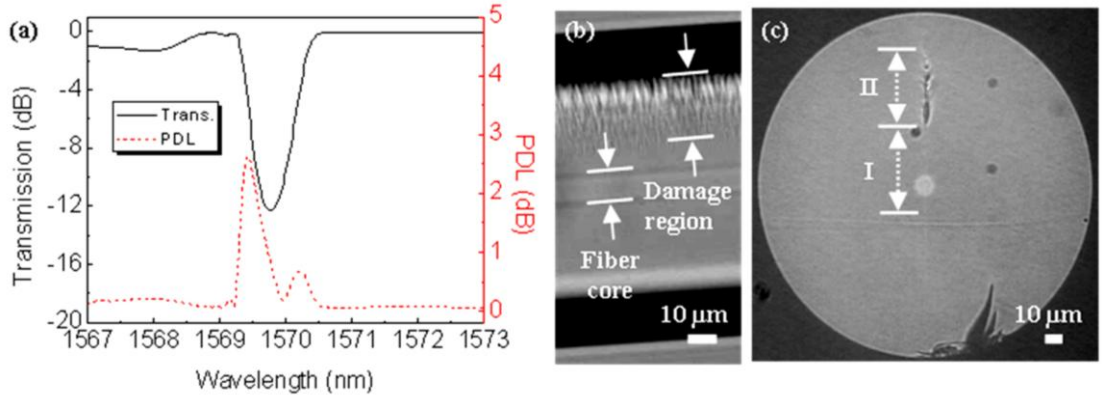


Fig. 3.3 Hybrid FBG inscribed in $H_2$-free SMF-28 fiber. (a) Transmission spectra and PDL; (b), (c) the axial and cross sectional morphology.

For $H_2$-loaded SMF-28 fiber, hydrogen loading significantly enhances the photosensitivity of the Ge-doped fiber so as to lead to lowering of grating writing threshold [13]. During the laser inscription, purple light is easily observed in the laser-fiber interaction area and the brightness is seen to increase as the intensity of the incident fs laser rises and white light generation (self-focusing/ionization) is very weak, even though the used fs laser intensity is high enough to achieve the formation of a damage grating in $H_2$-free fiber. This phenomenon may indicate that in the case of $H_2$-loaded fiber, colour centre formation is predominant for the RI change rather than ionization. A type I-IR FBG with 20.1dB reflectivity is written in the $H_2$-loading SMF-28 fiber with an intensity of $5.1\times10^{12} W/cm^2$, an exposure dose of $880 kJ/cm^2$ (30min irradiation duration, 1.8 million pulses). The background loss is $< 0.1 dB$. When the laser energy is increased, a 22.4dB Type II-IR FBG is inscribed

with an intensity of $13.0\times10^{12} W/cm^2$ and an exposure dose of $37 kJ/cm^2$ (30-s irradiation duration, 30000 pulses). The background loss is ~0.6dB. The spectral properties and the corresponding grating morphology are compared in Fig. 3.4.

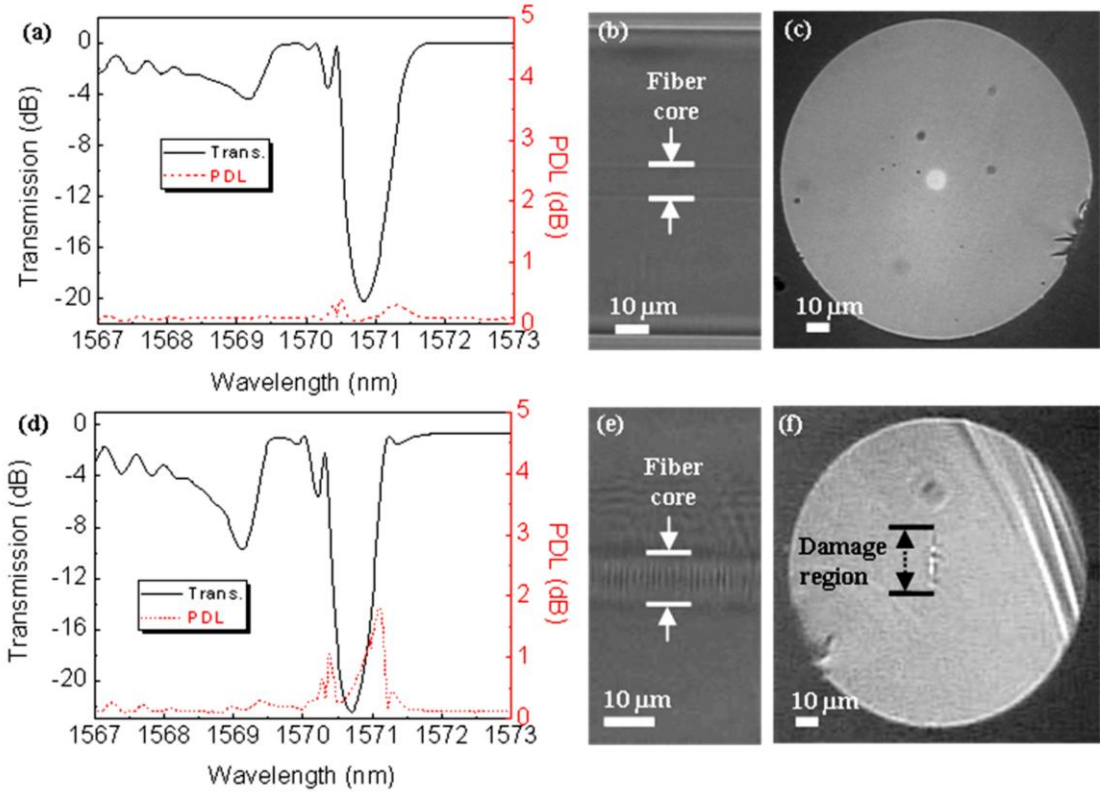


Fig. 3.4 Type I-IR and type II-IR FBG inscribed in $H_2$-loaded SMF-28 fiber. (a) Transmission spectra and PDL of Type I-IR FBG; (b), (c) The axial and cross sectional morphology of Type I-IR FBG; (d) Transmission spectra and PDL of type II-IR FBG; (e), (f) The axial and cross sectional morphology of type II-IR FBG.

Comparing Figs. 3.4 (a) and 3.4(d), it can be seen that the cladding mode coupling is stronger in the $H_2$-loading type II-IR FBG, this being similar to the $H_2$-free fiber case. For $H_2$-loading type I-IR FBG, the index change resulting from an enhanced colour centre formation in the presence of hydrogen [13] is strictly confined in the core but its fringe visibility is even worse than that in Fig. 3.2 (b). The grating cannot be observed by the optical microscope directly or by the use of RI matching liquid (see

Figs. 3.4 (b) and 3.4(c)). The PDL of the $H_2$-loaded type I-IR FBG is as small as ~0.4dB and this means that the induced birefringence by fs laser is smaller than or on the same order as the fiber intrinsic birefringence [12]. The unique polarization independency shows significant potential in the fabrication of optical fiber devices.

The morphology of the type II-IR FBG in $H_2$-loaded SMF-28 fiber is represented in Figs. 3.4 (e) and 3.4(f). Being similar to the morphology in Fig. 3.2 (f), the crack representing the damage is localized across the core to the cladding so as to achieve a large PDL of 1.8dB. For a better comparison, damage region of the mentioned type II-IR FBGs written in $H_2$-free and $H_2$-loaded SMFs is enlarged in Fig. 3.5. It is found that the material modification in the $H_2$-loaded fiber seems much weaker than that observed in $H_2$-free fiber with a similar exposure condition. The morphology difference may be accounted for the observed purple light and the weak white light generation in grating inscription. Colour centre formation in Ge-doped core is enhanced for $H_2$ loading; on the other hand, multiphoton ionization being trigged by self focusing is suppressed. That means $H_2$ loading effectively enhances the absorption of laser energy for Ge-doped core to induce a large index modulation and to decrease fiber damage. The consequently reduced damage in the $H_2$-loaded type II-IR grating thus represents a real advantage of using $H_2$ loading.

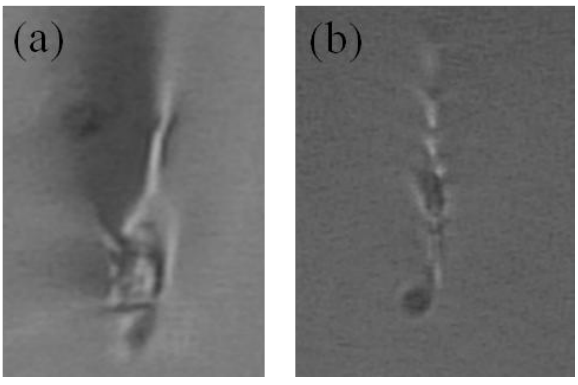


Fig. 3.5. Enlarged view of the damage region in the cross section. (a) Type II-IR FBG in $H_2$-free SMF; (b) Type II-IR FBG in $H_2$-loaded SMF.

The hybrid structure is also found in the $H_2$-loaded case where a 21.0dB ($\Delta n_{ind} = 1.0\times10^{-3}$) FBG is inscribed in the $H_2$-loaded SMF-28 fiber with an intensity of $14.0\times10^{12} W/cm^2$ and an exposure dose of $40 kJ/cm^2$. The background loss is $< 0.8 dB$. Fig. 3.6 shows the spectral properties and the corresponding morphology of this FBG. It can be seen that the laser processing area consists of a crack of micron lateral dimensions in the cladding, followed by a short region with a slight stress zone across the core. Being different from the case seen in Fig. 3.3 (c), the damage crack is closer to the core so that it is considered that the proportion of the type II index change component is increased. In Fig. 3.6 (a) the spectral property of the hybrid grating is similar to that of the damage grating, i.e. strong cladding modes and a large PDL are seen.

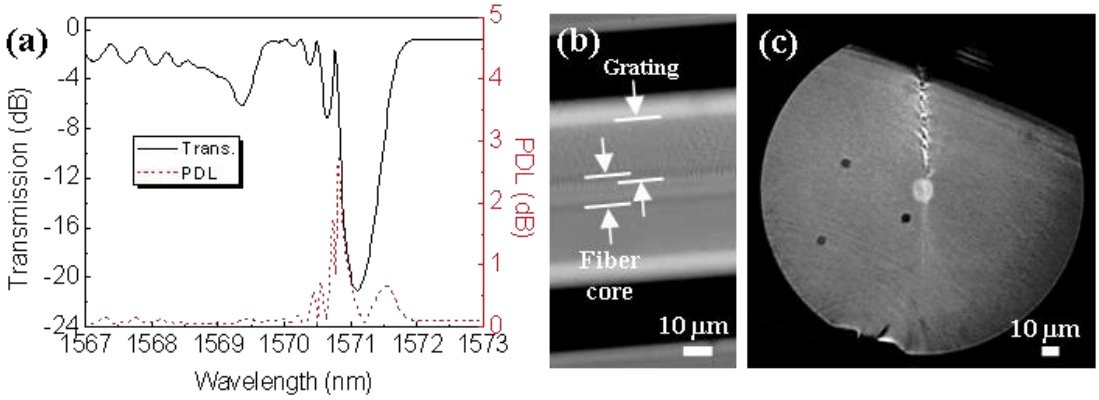


Fig. 3.6 Hybrid FBG inscribed in $H_2$-loading SMF-28 fiber. (a) Transmission spectra and PDL; (b), (c) The axial and cross sectional morphology.

## 3.3 Thermal Stability

Thermal stability of fs laser-inscribed FBGs is dependent on the inscription conditions such as the pulse duration, the pulse energy and the fiber alignment [14-16]. Study of the thermal stability of the fs inscribed FBGs has been carried out by use of the short-term annealing and long-term annealing approaches [17].

The annealing test is performed in a tube furnace (CARBOLITE MTF 12/38/250) equipped with an internal ceramic tube of 38mm diameter cantered within the furnace tube, which enabled temperatures as high as 1200$^{o}$C to be reached (See Fig. 3.7). The gratings are loosely placed in the inner tube so that no external stresses are applied to them. The temperature in close proximity to the gratings is monitored using the thermocouple probe built into the feedback and control circuit of the furnace and thus the gratings are placed in the middle of furnace tube, thus being close to the thermocouple. The experiment is performed in ambient air with a heating rate of 20$^{o}$C/min.

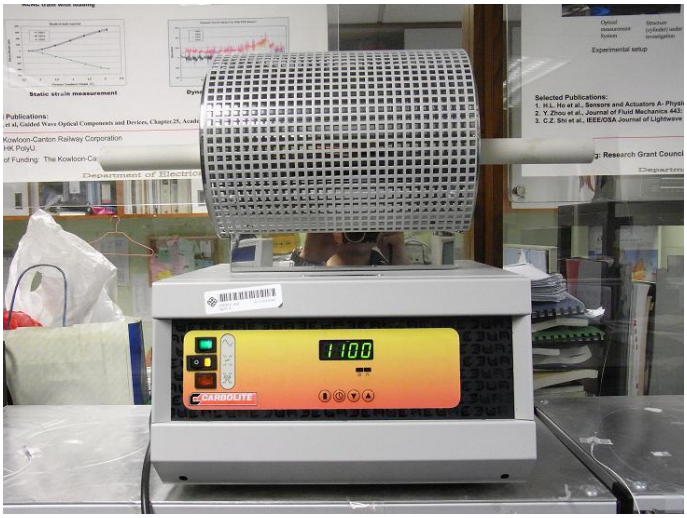


Fig. 3.7 Image of CARBOLITE MTF furnace

## 3.3.1 Short-term Annealing

In the short-term annealing, the FBGs are subjected to short-term exposure (30min at each temperature) at 100$^{o}$C, 200$^{o}$C, and then progressively to 1000$^{o}$C with a temperature increment of 100$^{o}$C. The calculated $\Delta n_{mod}$ obtained from the transmission spectra is plotted versus temperature in Fig. 3.8, where the initial $\Delta n_{mod}$ of the FBG used is normalized to unity.

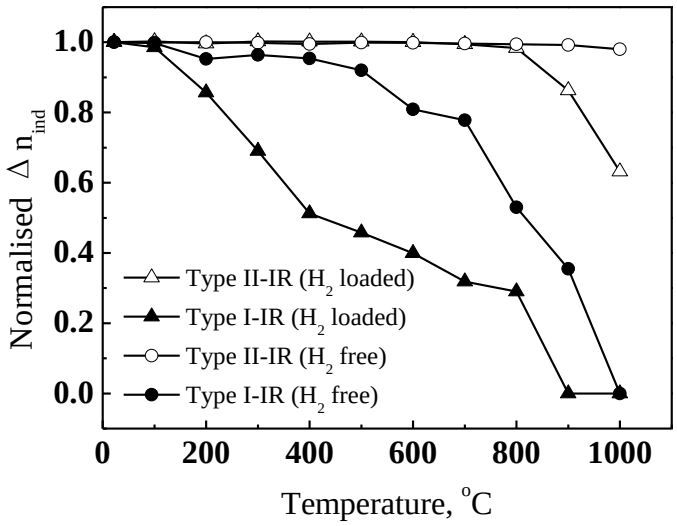


Fig. 3.8 Short-term annealing study of FBGs inscribed in the $H_2$-free and $H_2$-loaded SMF-28 fibers.

When the temperature is increased, it is observed that in both $H_2$-free and $H_2$-loaded fibers, type II-IR FBGs are more thermally stable than type I-IR FBGs. It is observed particularly that type II-IR FBGs written in $H_2$-free fibers own the highest thermal stability, this being followed by $H_2$-loaded type II-IR FBGs and then $H_2$-free type I-IR FBGs. $H_2$-loaded type I-IR gratings has the poorest thermal stability. A 50% decrease of the normalized index change is reached at temperatures of 400℃ and 800℃, for the $H_2$-loaded and the $H_2$-free SMF-28 fibers, respectively. In particular, stability of $H_2$-loaded FBGs is seen to decrease rapidly and the grating completely disappeared when the temperature approaches to 900℃. In summary, Type I-IR FBGs can be easily fabricated (especially in hydrogenated fibers), have high spectral quality and good reproducibility but they have relatively low thermal stability. The index change induced in Type I-IR gratings is likely due to the highly nonlinear defect formation resulting from a multiphoton absorption process. These defects, like those associated with type I-UV exposures, can be annealed out below the glass transition temperature.

While type I-IR FBGs due to multi-photon absorption are almost erased as the

temperature exceeded 900℃, type II-IR FBGs reveals ultra-high thermal stability. Type II-IR gratings written in $H_2$-loaded fibers are almost unaffected by thermal exposure at temperatures of up to 800℃ as are those written in $H_2$-free fibers. Above this a portion of the RI change of this grating is annealed out, resulting in a degradation of grating reflectivity from $\Delta n_{mod} = 1.7\times10^{-3}$ to $1.2\times10^{-3}$ within a few minutes of the temperature reaching 900℃. This is probably due to a large portion of the initial total index change coming from an annealable index change rather than a permanent damage type index change [16]. However the type II-IR gratings written in $H_2$-free fibers remain stable at temperatures up to 1000℃ because of their ultrastable local damage structure.

The FBGs fabricated in $H_2$-free fibers have relatively good thermal stability, and the Type I-IR FBGs can sustain temperatures of 500℃ with 96% of its initial $\Delta n_{mod}$ remaining, showing an almost negligible decay rate while type II-IR FBGs can retain more than 98% of its initial $\Delta n_{mod}$ after a 30min exposure at a temperature of 1000℃.

## 3.3.2 Long-term Annealing

A long-term thermal stability test is also carried out by heating the gratings (type II-IR FBGs in $H_2$-free and $H_2$-loaded fibers) to 700℃ and then kept them at that temperature for 12h. The results obtained show that there is almost no degradation of the grating strength in both of the fibers. The gratings are subsequently heated to 1000℃ (and remain at that temperature for 12h) with the evolution of the grating reflectivity and the resonant wavelength being recorded, as shown in Figs. 3.9 (a) and 3.9 (b), respectively. The calculated $\Delta n_{mod}$ determined from the reflection spectra is plotted as a function of annealing time. It can be noted that the thermal stability of the $H_2$-loaded type II-IR FBGs are substantially increased over the high temperature range considered arising from the 700$^{o}$C annealing treatment and thus could sustain

high temperature of up to 1000 ℃. After 12h, there is only a slight degradation of the grating strength for the duration of the test. This property is similar to that of regenerated gratings created during high temperature annealing of type I gratings [18, 19]. However, the tested gratings are indeed type II "damage" gratings in $H_2$-loaded fibers. In the experiment carried out here, the resonance wavelength is also measured every hour during the annealing process, and shown to be approximately constant regardless of the annealing time at 1000 ℃ as shown in Fig. 3.9(b). A closer look at this figure, i.e. the insert, reveals the slow drift toward longer wavelengths for both $H_2$-free and $H_2$-loaded gratings and that the former varies rapidly.

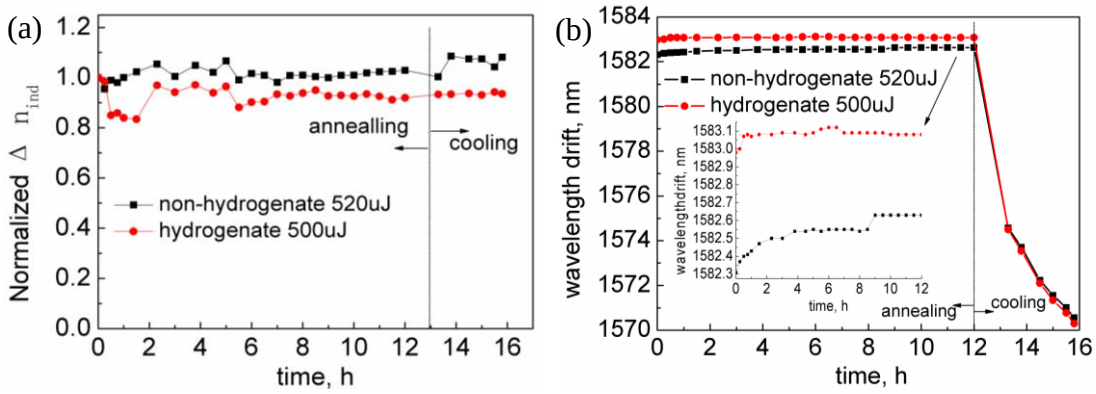


Fig. 3.9 Isothermal evolution of the reflection and resonant wavelength of type II-IR FBGs inscribed in $H_2$-free and $H_2$-loaded fibers over a 12h-period at 1000°C annealing followed by 4h cooling. (a) The response in terms of reflectivity; (b) The wavelength drift response.

The evolution of the reflectivity and the resonant wavelength of type II-IR FBGs inscribed in both $H_2$-free and $H_2$-loaded fibers can also be observed during the annealing process. Fig. 3.10 demonstrates the reflection spectra at the beginning and the end of the long-term annealing process at 1000 ℃, along with the original spectra both at room temperature and then after 4 h cooling. The spectral quality for both gratings is found to be greatly improved arising from the high temperature annealing treatment. The reason for this is that the thermally activated defects induced by the high intensity pulses are annealed out, leaving a very smooth interface between the

structurally altered region and the unaffected region within the material.

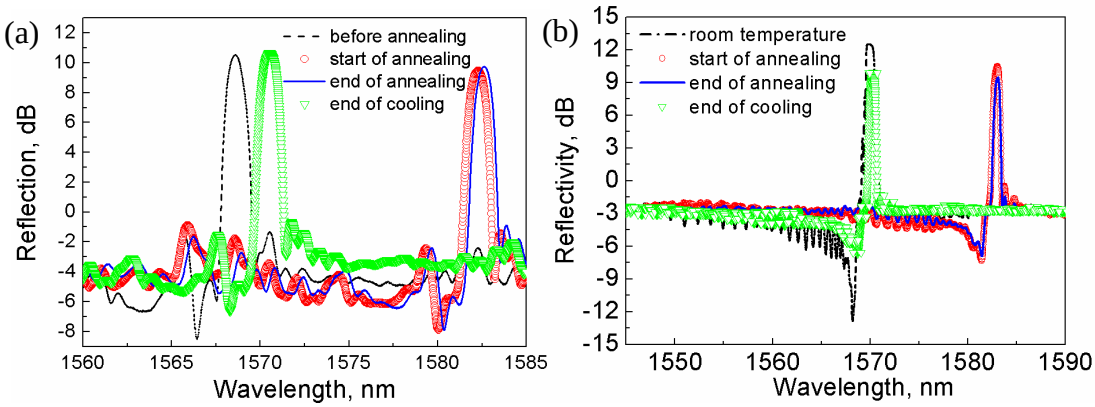


Fig. 3.10 Spectral evolution of Type II-IR FBGs inscribed in (a) $H_2$-free and (b) $H_2$-loaded fibers at four times shown during the annealing process.

The temperature is subsequently increased beyond 1000 ℃ and stabilized at 1150 ℃. The gratings, however, are gradually erased, as expected, during this very high temperature heat-treatment process. Type II-IR FBGs inscribed in the hydrogenated fibers decayed rapidly and disappeared within several minutes, while the $H_2$-free FBGs decreased relatively slowly and the corresponding spectral response is recorded in Fig. 3.11. The FBG written in the $H_2$-free fiber decreased rapidly and its reflection reached 0dB after a period of 442min. It should be noted that the grating is not completely erased as there was ~ 5dB insertion loss of the grating, seen from the insert in Fig. 3.11(a). The Bragg resonance of the grating shifts slowly towards a shorter wavelength with the annealing time, as shown in Fig. 3.11(b), which coincides with the grating decay. However, the shift is not monotonic and fluctuations in the resonance wavelength are observed during the annealing process. $\lambda_{Bragg}$ is related to the effective index and the grating period, both of which change with the temperature: however their high temperature behavior is still not well understood.

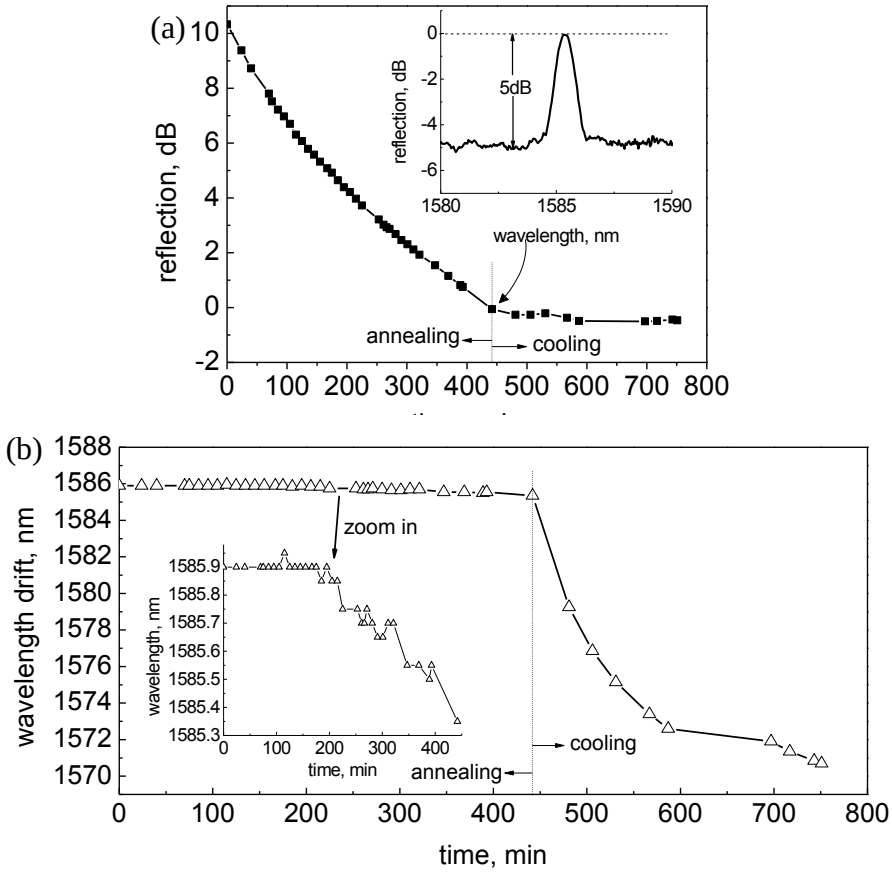


Fig. 3.11 Isothermal evolution of (a) the reflection and (b) resonant wavelength of type II-IR FBGs inscribed in $H_2$-free fibers during 442min (at 1150$^{o}$C) annealing and 180min cooling.

## 3.4 Temporal Thermal Response

Temperature change of most systems occurs much more slowly than does the Bragg wavelength shift of the grating, and hence there is no need to consider the temporal response of the Bragg wavelength shift. However, there are some rapidly changing, dynamic systems where knowledge of the temporal thermal response of the sensing elements used is especially important, such as in internal combustion engines [20], where the sensing elements should have a fast response time in order to follow closely the fast temperature change of the system. Thus, an ideal temperature sensor should exhibit both high temperature stability and a fast response time, commensurate with the dynamic temperature changes being measured.

A Type II-IR FBG with reflectivity of ~13.2dB is used in the temporal response test. There is no annealing treatment done to the grating after laser fabrication. The reflection spectrum and the morphology of the FBG are shown in Fig. 3.12. This linear damage in the cladding has destroyed the axial symmetry to the fiber axis that might become an influencing factor in the temperature sensing applications under consideration. Consequently for a better understanding of the process occurring, it is essential to study the relationship between the temporal response and the heating directionality.

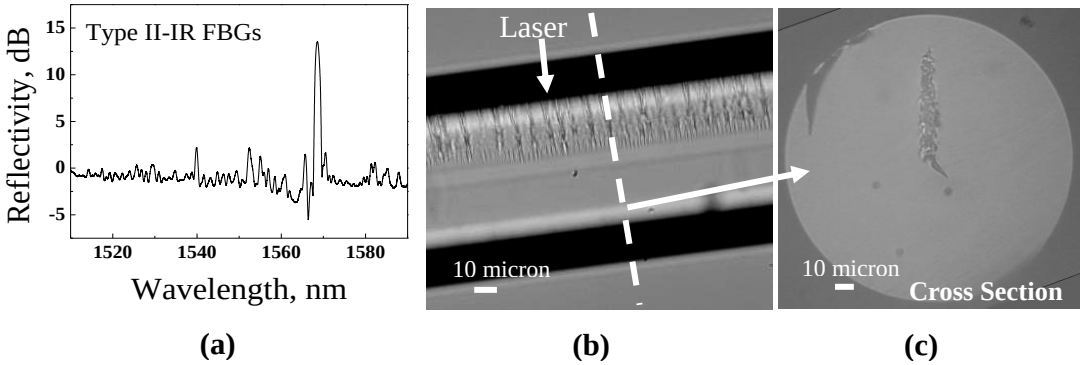


Fig. 3.12 Reflection spectrum and morphology of Type II-IR FBG fabricated by a fs laser with a phase mask method.

## 3.4.1 Calibration

The calibration process is implemented to make sure there is a good correspondence between the Bragg wavelength shift and the temperature change occurring in the tube furnace used. To effectively measure $\lambda_{Bragg}$ as a function of temperature, the FBG is heated from room temperature -25$^{o}$C up to 1150$^{o}$C in steps and the reflection spectrum is taken in each case after 10min, to allow for temperature stabilization. Cycling heating experiment is implemented to eliminate the error in the calibration.

Fig. 3.13 shows the variation of $\lambda_{Bragg}$ as a function of temperature. The triangles on

the graph are the recorded data, and the solid line is a quadratic fit to the data. Generally speaking, the optical fibers have two regions of different types of behavior: one, for temperatures up to about 800°C, where the Bragg wavelength shifts almost linearly with the increase of the temperature; the other, for the higher temperatures up to ~1200°C, where the Bragg wavelength shift has a nonlinear dependence on temperature due to the thermo-optic coefficient of the fused silica glass [21]. The good quadratic relationship seen ($R^2$=0.999) indicates the high potential of the type II FBG in the ultra-high temperature sensing applications investigated.

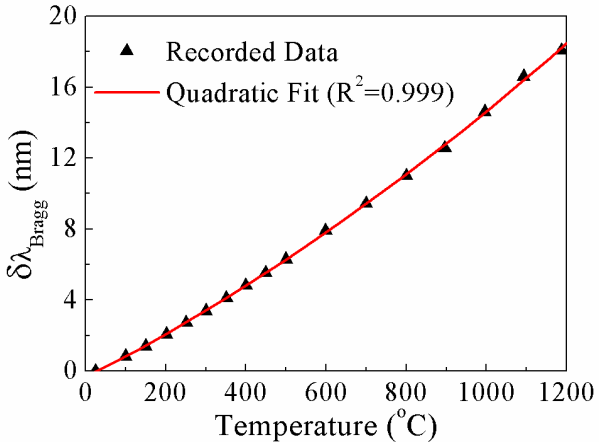


Fig. 3.13 Graph showing the change of $\lambda_{Bragg}$ as a function of temperature. The triangles are the recorded data, and the solid line is the quadratic fit.

## 3.4.2 Heating and Cooling Experimental Results

Fig. 3.14 shows the experimental setup used to measure the temporal thermal response. Exposing the grating to a step change in temperature is a challenge in the experiment. A $CO_2$ laser used in CW operation is chosen as the heating source as its output could be conveniently modulated using an optical chopper (New Focus, 3501) when heating and cooling the fiber. The lasing wavelength of $CO_2$ laser is in the far infrared ($\lambda_{laser}$=10.6 μm) and the fused silica fiber absorbs almost all of the incident laser energy [22]. The laser beam passes through a convex lens to broaden the beam

diameter to irradiate the grating more uniformly and the grating is fixed in the center of laser beam.

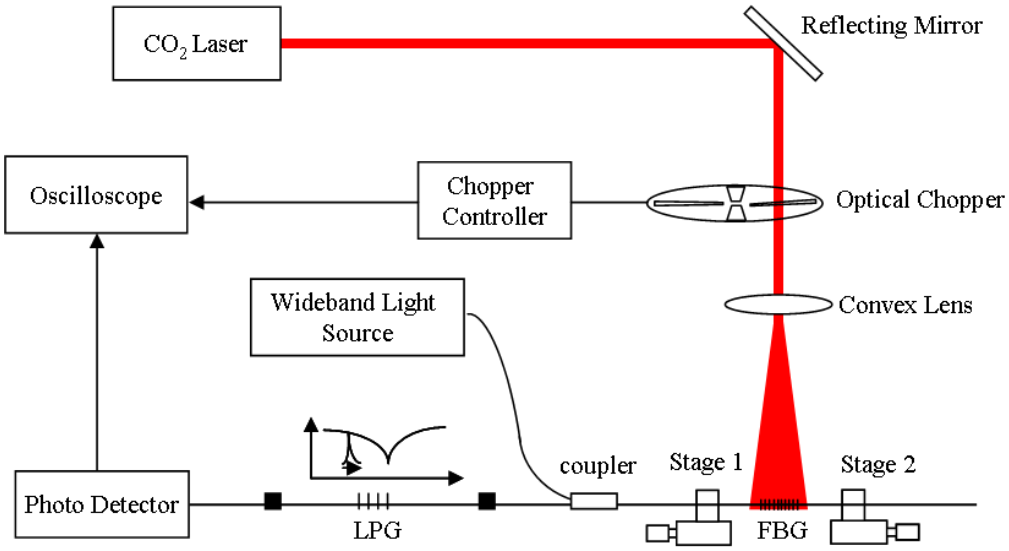


Fig. 3.14 Experimental setup for temporal thermal response measurement

To observe and record the fast signal change with the temperature, it is necessary to use a high speed demodulation system. To do so, a specified LPG, acting as an edge filter, is connected with the tested FBG. $\lambda_{Bragg}$ is around 1570nm at room temperature and the wavelength is expected to shift to 1575nm under the maximum power irradiation, and thus one LPG is designed and fabricated with a linear falling edge profile at wavelengths between 1570nm and 1575nm in the transmission spectrum. As long as the FBG spectrum is shifted to longer wavelengths by using the $CO_2$ laser heating, the reflection wavelength signal of the FBG is filtered along the falling edge of the LPG, causing the detector output power change. Such a signal is easily recorded on the oscilloscope, as shown in Fig. 3.15. The temporal response of this system overall is also dependent on the response characteristics of the photodetector used but overall it has been designed to provide a sufficient demodulating speed for this application.

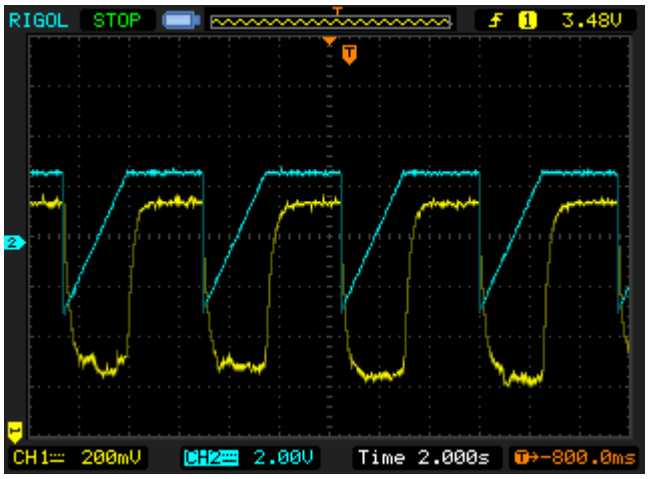


Fig. 3.15 Typical response of the detected optical power (lower trace) with the incident $CO_2$ laser signal (upper trace). Laser is ON at the rising edge of the signal and OFF at the constant high level.

The 'time constant' is used to quantify the temporal thermal response, which is defined as the time for the temperature to change to $1-\frac{1}{e}$ or 63.2 % of the difference between their initial and final temperatures, during a sudden change in the surrounding temperature [23]. To study the time constant at different final temperatures, the FBG is heated by use of different laser powers. Because the laser power cannot be adjusted in the CW operation, the incident power irradiating the FBG is adjusted by changing the height of grating (the more close to the convex lens, the higher is the laser power the FBG receives). Experiments are implemented at three heights for the purpose of comparison and the results obtained are demonstrated in the Fig. 3.16 insert. The beam diameter at each height is ~10, 8, and 5 mm, respectively, and Corning SMF-28 with a diameter of 125 μm is used. Thus the related dimensions of the beam to grating are around 220/1, 140/1, and 55/1, respectively. The spectrum drifts obtained at the three heights are also shown in Fig. 3.16. The calibration curve indicates that the final temperatures of the grating in the three cases are 330, 415, and 460 ℃, respectively; the corresponding powers absorbed by the FBG are estimated to be 19, 24, and 27mJ, respectively.

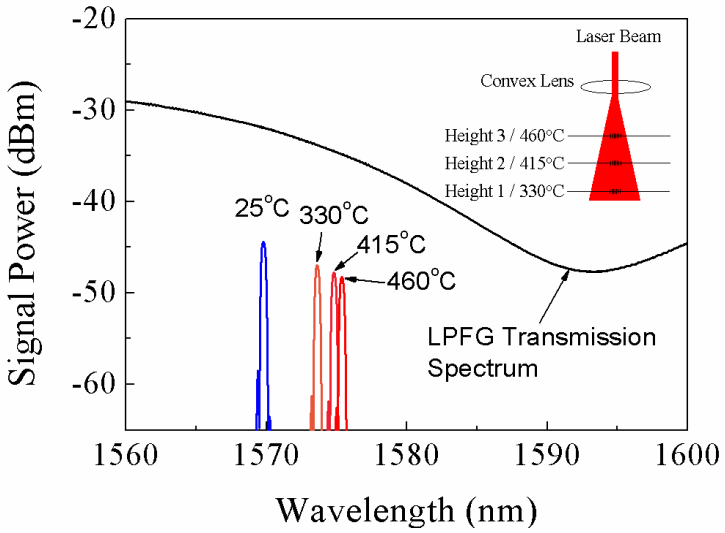


Fig. 3.16 Spectrum of the LPG superimposed with the ones of the FBG at room temperature, 330°C, 415°C and 460°C. The insert shows the relationship between the height of FBG and the final temperature FBG attained.

Fig. 3.17 demonstrates the voltage signal recorded by the oscilloscope as a function of time at three different heating powers. To facilitate the observation, the voltage signal is reversed vertically before data analysis. The dots represent the recorded data; the solid curve represents the five-point smoothing of the data. When the heating power is increased by raising the FBG, the switching time increases (this is defined as the time for $\lambda_{Bragg}$ to shift from its rest position to the point at which the photodetector voltage is at maximum). The switching time is another important parameter for applications such as temperature measurement because the final temperature will be known only after the switching time has elapsed. In Fig. 3.17, the switching time for the lower final temperature of 330 ℃ is ~750ms, which is then increased to 780ms for the medium level of 415 ℃. In the case of a higher final temperature of 460 ℃, this value increases slightly to 790ms. However, the temporal thermal response for heating the grating is found to be independent of the heating power and the final temperature. Thus the temporal thermal response of the heating system is measured to be 230±25ms.

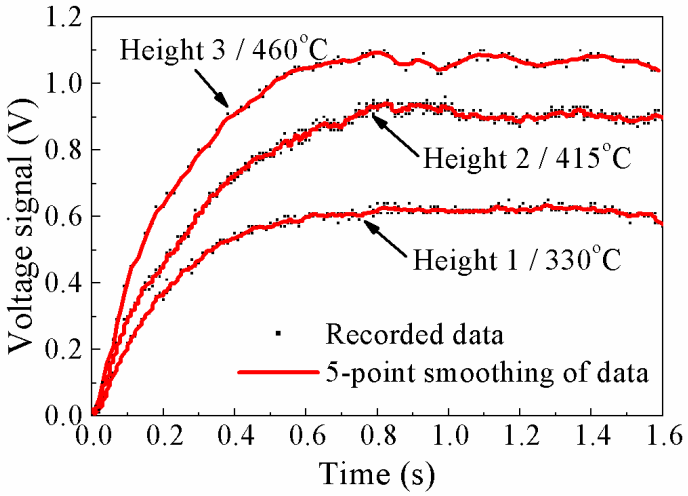


Fig. 3.17 Heating curves as a function of time for a Type II-IR FBG, which is heated by $CO_2$ laser beam at different height thus attaining different final temperature.

The cooling is closely followed by the heating phase. Before the cooling starts, the FBG should have reached a steady state, with the voltage signal being stable at a maximum for some time. When the $CO_2$ laser beam is shuttered (i.e., off), the FBG returned to room temperature quickly by dissipating the heat to the surrounding air. The reflection spectrum is shifted backward to its initial position, and the voltage signal falls to zero.

Fig. 3.18 shows the results of the FBG cooling. The dots represent the recorded data; the solid curve represents the five-point smoothing of the data. Being similar to the result obtained in the heating, the switching time values for different initial temperatures are very close. Corresponding to the different initial temperatures 330, 415, and 460 ℃, respectively, the switching times are measured to be nearly 1.34, 1.34, and 1.36s, respectively. We also find that the temporal thermal response is independent of the initial temperature and is measured to be 275±25ms, which is slower than the value obtained for the heating phase.

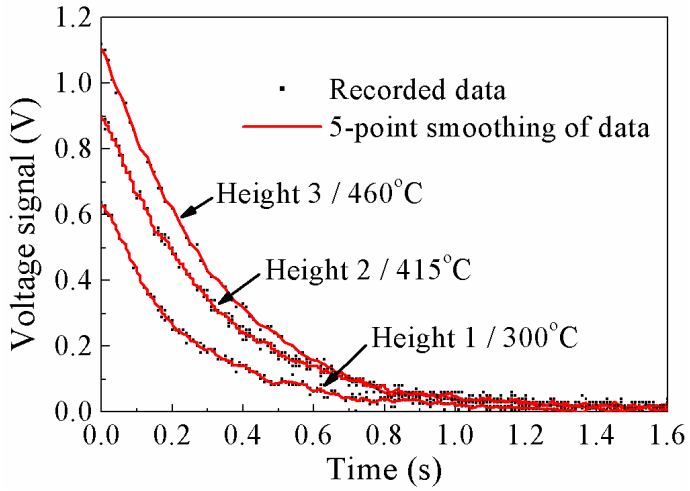


Fig. 3.18 Cooling curves as a function of time of a Type II-IR FBG with different initial temperature.

In fs laser-based phase mask inscription method, the axial symmetry of the fiber is destroyed, as has been discussed above. The RI modulation is created in both the core and on one side of the cladding. To quantify the effect due to the axial asymmetry, the temporal thermal response is measured by rotating the FBG, in steps of 30°. The grating groove is parallel to the incident $CO_2$ laser in the beginning, which is illustrated in the insert of Fig. 3.19, showing the results of heating and cooling the fiber in terms of the incident laser power from various directions. The triangles on the graph are the measured data during the laser heating, and the squares on the graph are the measured data from the cooling. By comparing the two curves, it is found that the temporal thermal response is essentially independent of the directionality (even though there is some slight fluctuation that might be induced by the change of the irradiation condition with the fiber rotation). During the heating process, the measured temporal thermal response is ranged from 200ms to 250ms, with an average value of 230 ± 25ms. Similarly during the cooling, this same parameter ranged from 250ms to 300ms and the average value is calculated to be 275 ± 25ms. These results illustrate that the Type II-IR FBG have uniform temporal thermal response, this being essentially independent of heating direction.

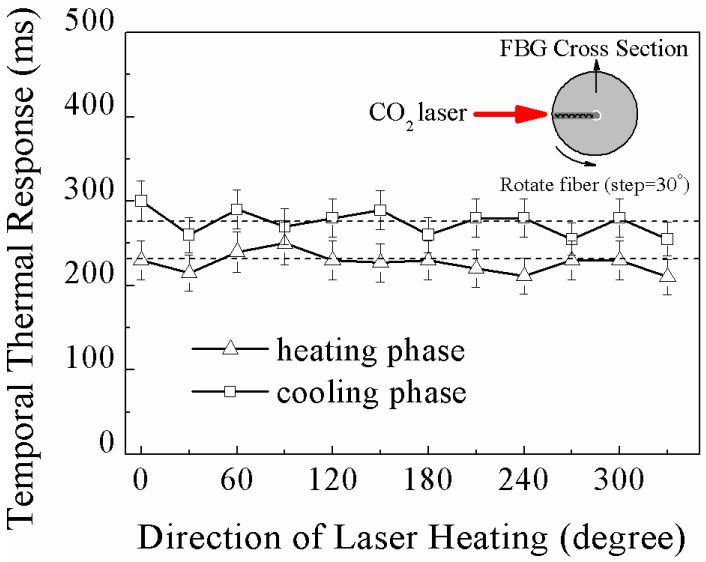


Fig. 3.19 Temporal thermal response of a Type II-IR FBG as a function of the laser heating direction. The triangles are the data in the heating and the squares are the data in the cooling.

### 3.4.3 Theory of Fiber Heating and Cooling

Heating and cooling of a fiber resulting from periodical $CO_2$ laser irradiation can be described by lumped system equation in the one-dimensional case [24, 25]:

$$\frac{dT(t)}{dt} = -\frac{1}{\tau}(T(t) - T_{air}) + \Xi(t)$$
$$\tau = \frac{c\rho V_f}{A_f h} = \frac{c\rho r}{2h}, \Xi(t) = \frac{q(t)}{c\rho} \tag{3.2}$$

with the initial condition,

$$T(0) = T_{air} \tag{3.3}$$

where *T(t)* is the fiber temperature as a function of time, $T_{air}$ is the temperature of the ambient air (=300K), c is the specific heat of the fiber (=837 J $kg^{-1}$ $K^{-1}$), ρ is the density of the fiber (=2200 kg $m^{-3}$), $V_f$ is the volume of the fiber, $A_f$ is the surface of the fiber, h is the convection coefficient (=400 W $m^{-2}$ $K^{-1}$) [24], *r* is the radius of the fiber and *q(t)* is the heat generation rate per unit volume. $\tau$ denotes the relaxation time and $\Xi(t)$ represents the periodical heating of $CO_2$ laser beam.

The laser heating is expressed by use of an isosceles-trapezoid waveform with rising / falling time of ~ 30ms. The heating power in one period of ~ 4s can be determined by the following equation:

$$\Xi(t) = \frac{k}{A_b rc\rho} P(t)$$

$$P(t) = \begin{cases} P_0 \cdot \dfrac{t}{30} & 0 < t \le 30ms \\ P_0 & 30ms < t \le 2000ms \\ P_0 \cdot (-\dfrac{t}{30} + \dfrac{203}{3}) & 2000ms < t \le 2030ms \\ 0 & 2030ms < t \le 4000ms \end{cases} \quad (3.4)$$

where *P(t)* is the heating power as a function of time, $P_0$ is the incident heating power before chopper, *k* is the power absorption rate (=0.1mm$^{-2}$), and $A_b$ is the cross-section of the laser beam ( =10 ).

For SMF-28 fiber (r ≈ 60 μm), assuming that the FBG is heated by $CO_2$ laser at different powers, $P_0$ is set to be 1, 0.7, and 0.5W in Eq.(3.4). Fig. 3.20 shows, through the simulation results that, for both of heating and cooling, the temporal thermal response is independent of the heating power, being equal to 160ms (heating phase) and 160ms (cooling phase). This time value is somewhat different from the experimental measured one but in good agreement with the simulation result ~ 140ms in Ref. 24. Sumetsky *et al.* [24] used an ideal rectangular waveform of heating power in simulation without considering the rising / falling time of power modulation; therefore there is a discrepancy of 20ms comparing with our simulation result. Besides the effect from the rising / falling time, there are other error sources affecting the response measurement. First, the falling edge of the transmission spectrum of LPG is not perfectly linear but convex, thus the measured temporal response should be slightly longer than the actual value. Second, fluctuation of $CO_2$ laser power and noise in the system would deteriorate stability of the voltage signal

on the oscilloscope, causing unavoidable measurement error. Due to the existence of these error sources, it is reasonable to explain the difference between the experimental measured value and the calculated one. However we do see our result as essentially being consistent with the others [23-25], which are all in the range of 100 - 200×$10^{-3}$s (within experimental error) and there are differences in the fiber used [23], the type of exposure [26] and other experimental conditions.

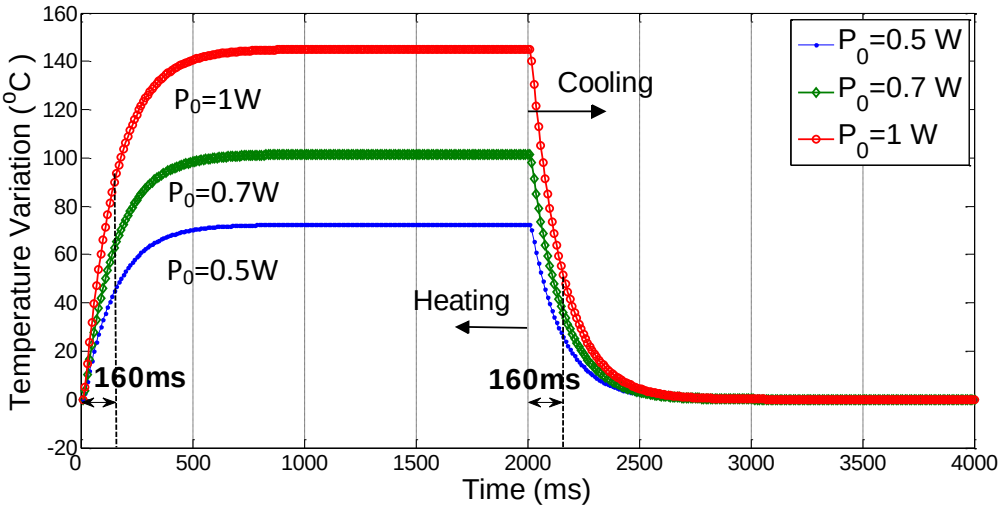


Fig. 3.20 Simulation of the heating and cooling curve of a SMF-28 optical fiber heated at various laser powers.

The effect of fiber size on the temporal thermal response has also been studied through using this simulation, with the results shown in Fig. 3.21. Assuming an identical incident laser power (P = 1W), the temporal thermal response of the fiber (r = 30 μm) is measured to be 80ms (heating phase) and 80ms (cooling phase) which is significantly faster than the previous simulation result of 160ms (heating and cooling phase) of the fiber with a radius of 60 μm. The results thus illustrate that the temporal thermal response is highly dependent on the fiber size (diameter), to be more accurate, the thermal mass of the fiber. As a result, an efficient method to enhance the temporal thermal response of the fiber sensors is to decrease the size of the optical fiber sensor itself, which can be achieved by writing an FBG in an optical

nanowire, for example. However, as the fiber size reduces much this fiber sensor would become much more sensitive to the noise of temperature signal; therefore the accuracy of temperature measurement would be deteriorated. To strike a good balance between the temporal response and the temperature accuracy, the fiber size should be carefully designed based on what is necessary for practical measurement.

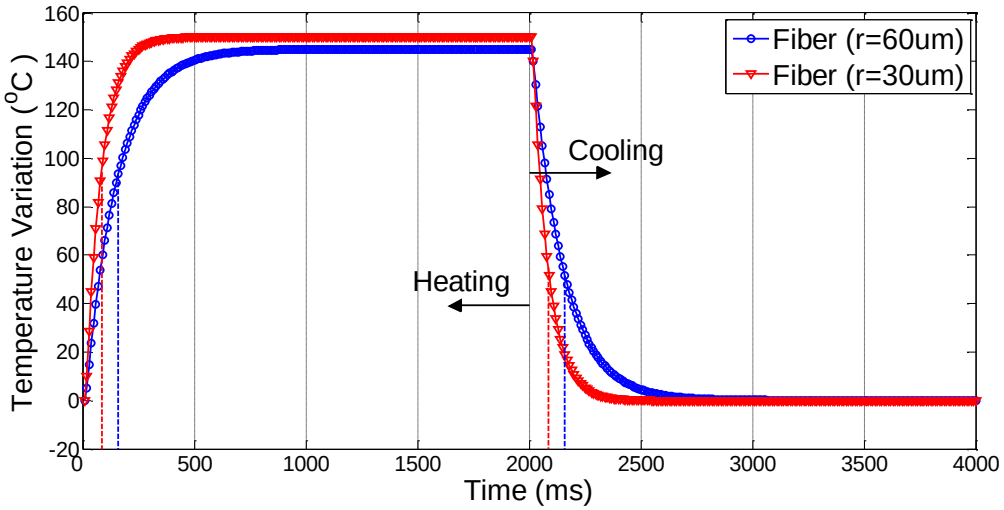


Fig. 3.21 Simulation of the heating and cooling curve of two optical fibers with different size at the same heating power.

## 3.5 Summary

We have introduced the fabrication of FBGs in $H_2$-free and $H_2$-loaded SMFs by using fs laser radiation through a phase mask. Then some characteristics of these FBGs were discussed in detail, including the grating morphology and the spectral property. Aiming to find some applications in ultra-high temperature sensing, thermal stability of the gratings was investigated by use of short-term and long-term annealing approaches. It is found that after pre-annealing type II-IR FBGs both in $H_2$-free and $H_2$-loaded fibers can sustain long-term annealing (for more than 12 hours) at temperatures of more than 1000 ℃. Finally the temporal thermal response of type II-IR FBG which has great potential to be used as high temperature sensors is experimentally investigated *via* a fast testing system that incorporates periodic $CO_2$ laser irradiation and the theoretical simulation based on lumped system equation is used to explain the experimental results. The FBGs described in this chapter are fabricated in conventional SMFs and in the next chapter we will discuss the fiber gratings inscribed in AS-PBGF which is based on a novel light-guidance mechanism.

# Reference

[1] Y. Kondo, K. Nouchi, T. Mitsuyu, M. Watababe, P. G. Kazansky, and K. Hirao, "Fabrication of long-period fiber gratings by focused irradiation of infrared femtosecond laser pulses," *Optics Lett.*, vol. 24, pp. 646-648, (1999).

[2] S. J. Mihailov, C. W. Smelser, P. Lu, R. B. Walker, D. Grobnic, H. Ding, G. Henderson, and J. Unruh, "Fiber Bragg gratings made with a phase mask and 800-nm femtosecond radiation," *Optics Lett*. vol. 28, pp. 995-997, (2003).

[3] K. A. Zagorulko, P. G. Kryukov, Y. V. Larionov, A. A. Rybaltovsky, and E. M. Dianov, "Fabrication of fiber Bragg gratings with 267nm femtosecond radiation," *Opt. Express* vol. 12, pp. 5996-6001, (2004).

[4] A. Martinez, M. Dubov, I. Khrushchev, and I. Bennion, "Direct writing of fibre Bragg gratings by femtosecond laser," *Electron. Lett.*, vol. 40, pp. 1170-1172, (2004).

[5] E. Wikszak, J. Burghoff, M. Will, S. Nolte, A. Tünnermann, and T. Gabler, "Recording of fiber Bragg gratings with femtosecond pulses using a point by point technique," *in Proceedings of IEEE Conf. on Lasers and Electro-Opt.*, (2004).

[6] J. Thomas, E. Wikszak, T. Clausnitzer, U. Fuchs, U. Zeitner, S. Nolte, and A. Tünnermann, "Inscription of fiber Bragg gratings with femtosecond pulses using a phase mask scanning technique," Appl. Phys. A, vol. 86, pp. 153-157, (2007).

[7] C. W. Smelser, S. J. Mihailov, and D. Grobnic, "Formation of Type I-IR and Type II-IR gratings with an ultrafase IR laser and a phase mask," *Opt. Express*, vol. 13, pp. 5377-5386, (2005).

[8] J. Albert, "Permanent photoinduced refractive-index changes for Bragg gratings in silicate glass waveguides and fibers," *MRS Bull.* vol. 23, pp. 36,

(1998).

[9] J. W. Chan, T. Huser, S. Risbud, and D. M. Krol, “Structural changes in fused silica after exposure to focused femtosecond laser pulses,” *Opt. Lett.* vol. 26, pp. 1726-1728, Nov. 2001.

[10] L. Sudrie, M. Franco, B. Prade, and A. Mysyrowicz, “Study of damage in fused silica induced by ultra-short IR laser pulses,” *Opt. Commun.*, vol. 191, pp. 333-339, (2001).

[11] P. Lu, D. S. Waddy, S. J. Mihailov, and H. Ding, “Characterization of the growths of UV-induced birefringence in effective mode index and index modulation in fiber Bragg gratings,” *Photon. Technol. Lett.*, vol. 17, pp. 2337-2339, (2005).

[12] P. Lu, D. Grobnic, and S. J. Mihailov, “Characterization of the birefringence in fiber Bragg gratings fabricated with an ultrafast-infrared laser,” *J. Lightw. Technol.*, vol. 25, pp. 779-786, (2007).

[13] C. W. Smelser, S. J. Mihailov, and D. Grobnic, “Hydrogen loading for fiber grating writing with a femtosecond laser and a phase mask,” *Opt. Lett.*, vol. 29, pp. 2127-2129, (2004).

[14] S. J. Mihailov, C. W. Smelser, D. Grobnic, R. B. Walker, P. Lu, H. Ding and J. Unruh, “Bragg gratings written in all-SiO2 and Ge-doped core fibers with 800-nm femtosecond radiation and a phase mask,” *J. Lightwave Technol.* vol. 22, pp. 94-100, (2004).

[15] C. W. Smelser, S. J. Mihailov, and D. Grobnic, “Formation of Type I-IR and Type II-IR gratings with an ultrafast IR laser and a phase mask,” *Opt. Express* vol. 13, pp. 5377-5386, (2005),

[16] D. Grobnic, C. W. Smelser, S. J. Mihailov, R. B. Walker, “Long-term thermal stability tests at 1000 ℃ of silica fibre Bragg gratings made with ultrafast laser radiation,” *Meas. Sci. Technol.* vol. 17, pp. 1009-1013, (2006).

[17] P. Lu, D. Grobnic, and S. J. Mihailov, "Characterization of the Birefringence in Fiber Bragg Gratings Fabricated With an Ultrafast-Infrared Laser," *J. Lightwave Technol.* vol. 25, pp. 779-786, (2007).

[18] J. Canning, S. Bandyopadhyay, "Fibre Bragg Grating Sensor for High Temperature Application," *In Australian Conference on Optical Fibre Technology (ACOFT) &Opto-Electronics Communications Conference (OECCC),* Darling Harbour, Sydney, Australia, (2008).

[19] B. Zhang and M. Kahrizi, "High-temperature resistance fiber Bragg grating temperature sensor fabrication," *IEEE Sens.* J. vol. 7, pp. 586-591, (2007).

[20] A. J. V. Wyk, P. L. Swart, and A. A. Chtcherbakov, "Fiber Bragg grating gas temperature sensor with fast response," *Meas. Sci. Technol.* vol. 17, pp. 1113-1117, (2006).

[21] D. Grobnic, C. W. Smelser, S. J. Mihailov, and R. B. Walker, "Long-term thermal stability tests at 1000oC of silica fibre Bragg gratings made with ultrafast laser radiation," *Meas. Sci. Technol.* vol. 17, pp. 1009-1013, (2006).

[22] G. M. H Flockhart, R. R. J. Maier, J. S. Barton, W. N. Macpherson, J. D. C. Jones, K. E. Chisholm, L. Zhang, I. Bennion, I. Read, and P. D. Foote, "Quadratic behavior of fiber Bragg grating temperature coefficients," *Appl. Optics* vol. 43, pp. 2744-2751, (2004).

[23] T. L. Lowder, J. A. Newman, W. M. Kunzler, J. D. Young, R. H. Selfridge, and S. M. Schultz, "Temporal response of surface-relief fiber Bragg gratings to high temperature CO2 laser heating," *Appl. Opt.* vol. 47, pp. 3568-3573, (2008).

[24] M. Sumetsky, Y. Dulashko, J. M. Fini, A. Hale, and D. J. DiGiovanni, "The microfiber loop resonator: theory, experiment, and application," *J. Lightwave Technol.* vol. 24, pp. 242-250 (2006).

[25] A. J. C. Grellier, N. K. Zayer, and C. N. Pannell, "Heat tranfer modeling in

CO2 laser processing of optical fibers," *Opt. Commun.* vol. 152, pp. 324-328, (1998).

[26] G. Rego, L. M. N. B. F. Santos, and B. Schröder, "Estimation of the fiber temperature during an arc-discharge," *Microw, Opt. Technol. Lett.* vol. 50, pp. 2020-2025, (2008).

# Chapter 4

# Fiber Gratings in All Solid Photonic Bandgap Fiber

PCFs are optical fibers in which the RI profile of the cladding is periodic in one or two dimensions, typically with a silica/air hole microstructure. When the air holes of a solid core index guiding PCF are filled with the material which has RI of larger than that of the background material, an AS-PBGF can be realized [1-3]. In this case, total internal refraction is forbidden and the core modes are confined by anti-resonant scattering from the high index inclusion, manifesting in discrete frequency transmission bands; this type of guidance is referred to as anti resonant refraction optical waveguiding (ARROW) [4-6].

In recent years, AS-PBGF has attracted intense research interests due to its bandgap mechanism, all-solid structure and useful properties such as dispersion control. When compared with the hollow-core PBGF (HC-PBGF), AS-PBGF has the advantages of easy fabrication and convenient splicing to the conventional SMFs without discharge induced air-hole collapse. Moreover, with suitable rare-earth doping in its solid core, an amplifier or laser can be readily constructed [7]. By introducing an index depressed layer around the high-index rods, an ultralow-loss transmission of 2dB/km can be achieved [3]. In addition, the all-solid fiber structure brings a lot of convenience in fiber grating inscription, as the total flux at the fiber core can be substantially reduced due to air-hole cladding scattering of light at various air-interfaces [8]. One may expect that the grating devices inscribed in this novel fiber should have interesting and beneficial properties in many applications.

# 4.1 Operation Principle of AS-PBGF

The RI of the high-index cylinders in AS-PBGF is assumed to be identical. At given frequency, a single cylinder has a finite set of guided modes. We first consider a single mode. When N high-index cylinders are brought together, the coupling between the cylinders lifts the degeneracy of the mode, which is split in N modes with different effective indices and field profiles [9]. The difference between effective indices is proportional to the strength of the coupling. Formation of bands is illustrated in Fig. 4.1.

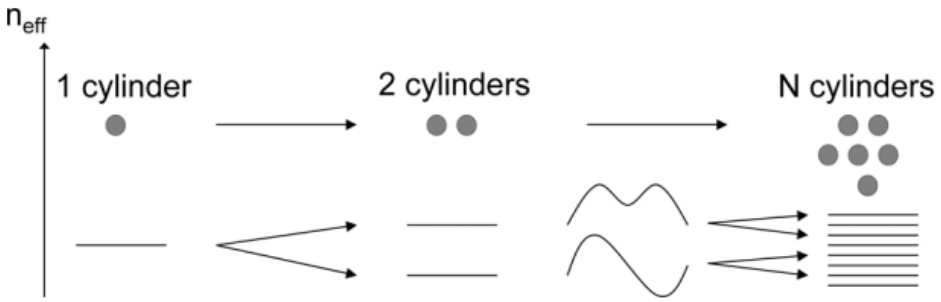


Fig. 4.1 Formation of bands: coupling of modes. When coupling two cylinders, each mode splits into two modes, in essence being the odd and even superposition of the modes of the single cylinders in isolation. When coupling N cylinders, N different modes are formed. The width in $n_{eff}$ of the splitting is proportional to the overlap between modes of adjacent cylinders [9].

The propagation diagram of a finite AS-PBGF thus consists of many curves clustering around the dispersion curves of a single high-index cylinder, with clusters being broader when the cylinders are more strongly coupled. The mechanism of band formation in the cladding of AS-PBGF is illustrated in Fig. 4.2. In the case of a single high-index cylinder, modes are guided for $n_{eff} > n_{bg}$, leaky otherwise. Increasing to N cylinders, the coupling among the N cylinders makes each dispersion curves split in N ones. If number N is increased to large enough, the cluster of split modes from (b) form band. Between the thus formed bands of dispersion curves, there are large regions in which no cladding modes exist and these are bandgaps of the cladding.

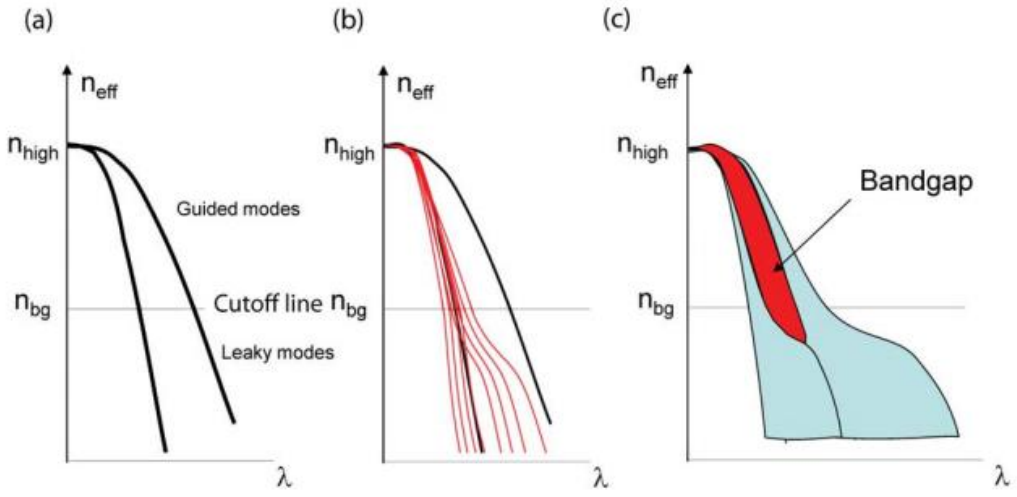


Fig. 4.2 Band formation in the cladding of AS-PBGF.

The schematic diagram of AS-PBGF's dispersion map is shown in Fig. 4.3. There are two types of modes in AS-PBGF, i.e. core mode and cladding mode. Core mode is confined to be the defect core by the bandgap effect discussed above; its effective indices are lower than background. Cladding mode is the mode of the microstructured cylinder lattice. Unlike the index-guided fibers, these cladding modes can be guided or radiative. The energy of the guided cladding modes is almost entirely confined in the high-index cylinders and their effective indices are above background. While a significant portion of energy of the radiative cladding modes is spread out into the low-index region due to the strong coupling between cylinders, being lossy modes and thus their corresponding indices are below background. The lossy or "radiative" cladding mode is in a continuous or quasi-continuous state. Different cylinder modes lead to different bands. The cylinder-mode bands are distinguished by modal profile (such as $LP_{01}$, $LP_{11}$, $LP_{02}$……) in the individual cylinder. Modes of azimuthal order decay more rapidly away from the cylinders, and thus couple weakly, leading to very narrow bands [10]. In practice only the cylinder modes of azimuthal orders 0 and 1 ($LP_{lm}$ mode with $l$=0 or $l$=1) couple strongly and create wide bands. Higher-order cylinder modes give rise to very narrow bands so that they are usually neglected in practice.

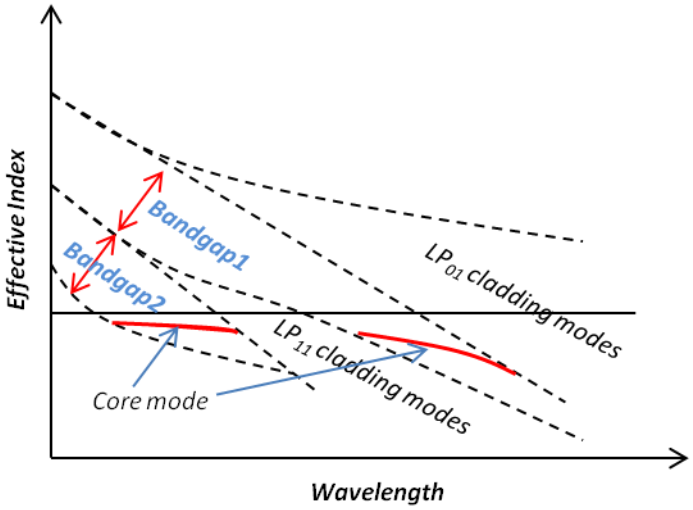


Fig. 4.3 Schematic diagram of dispersion map of AS-PBGF.

## 4.2 Theoretical Mode

The AS-PBGF (Yangtze Optical Fiber and Cable Corporation) used in our experiment is a new type PBGF [3]. Its microstructure is shown in Fig. 4.4. Triangularly arrayed germanium-doped cylinders of five layers (including 90 cylinders totally) are embedded in pure silica background and the cylinders is surrounded by an index depressed layer (fluorine doped). It has been shown that by introducing the depressed layer around the high-index cylinders, the confinement and bend loss of the AS-PBGF would be greatly improved [11]. The maximum RI differences of the germanium-doped and fluorine-doped area are approximately $3.67\times10^{-2}$ and $-8.4\times10^{-3}$, respectively, compared with the pure silica background. The fiber core is formed by omitting a single cylinder from the array. The outside diameter of the fiber is 123μm. The pitch of the cylinder lattice is 9.21μm and the relative diameters of the high- and low-index layer in the unit cell of the cladding are $d_h/\Lambda = 0.37$ and $d_l/\Lambda = 0.70$, respectively.

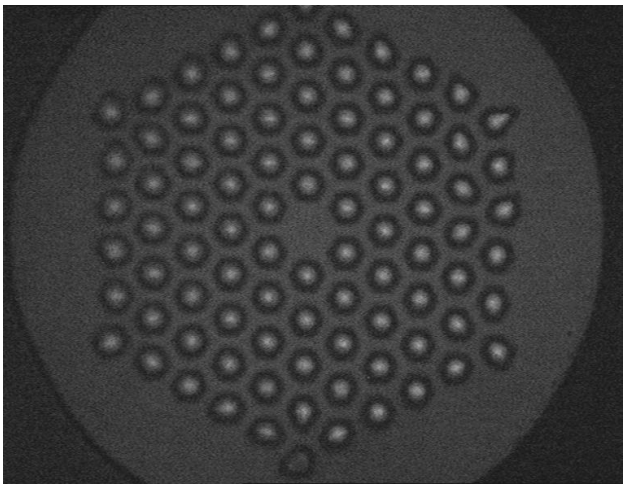

Fig. 4.4 Optical microscope image of the AS-PBGF end facet.

Mode profiling for the AS-PBGF is carried out with the commercial FEM software package COMSOL. A quarter model shown in Fig. 4.5(a) is used to decrease the required finite elements. Proper boundary conditions for the two orthogonal radiuses are set up to obtain both symmetric and antisymmetric modes. PML condition is used at the outer boundary of the fiber to calculate the confinement loss. The boundary condition used to simulate $LP_{01}$ core mode is shown in Fig. 4.5(b) where the dash-dot edge is perfect magnetic conductor; the dashed-line edge are perfect electric conductor and the solid-line edge is continuity. Fig. 4.5(c) describes the boundary condition to simulate $LP_{11}$ core mode in which the dashed-line and solid-line edges stand for perfect magnetic conductor and continuity respectively.

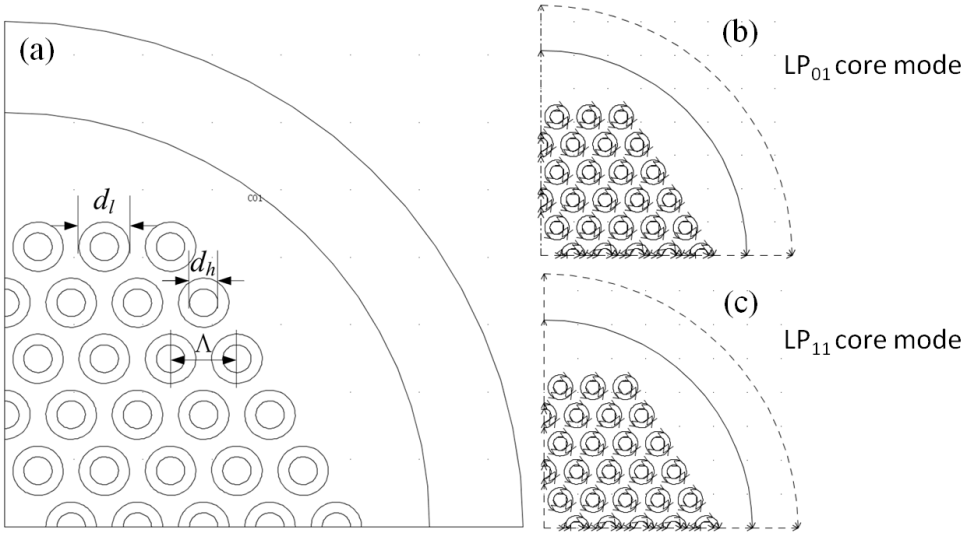


Fig. 4.5 A quarter model of the used AS-PBGF and the boundary conditions used in simulation.

The modal field profiles of the core modes and cladding modes at 1550nm are simulated and demonstrated in Fig. 4.6. The simulation results obtained indicate that there are two core modes being supported by the fiber i.e. $LP_{01}$ and $LP_{11}$ core mode. The effective indices of modes are calculated to be 1.4417 for $LP_{01}$ core mode and 1.4392 for $LP_{11}$ core mode. Fig. 4.6(c) shows one guided cladding mode with an effective index of 1.4447 and for comparison one radiated cladding mode is illustrated in Fig. 4.6 (d) whose effective index is 1.4377.

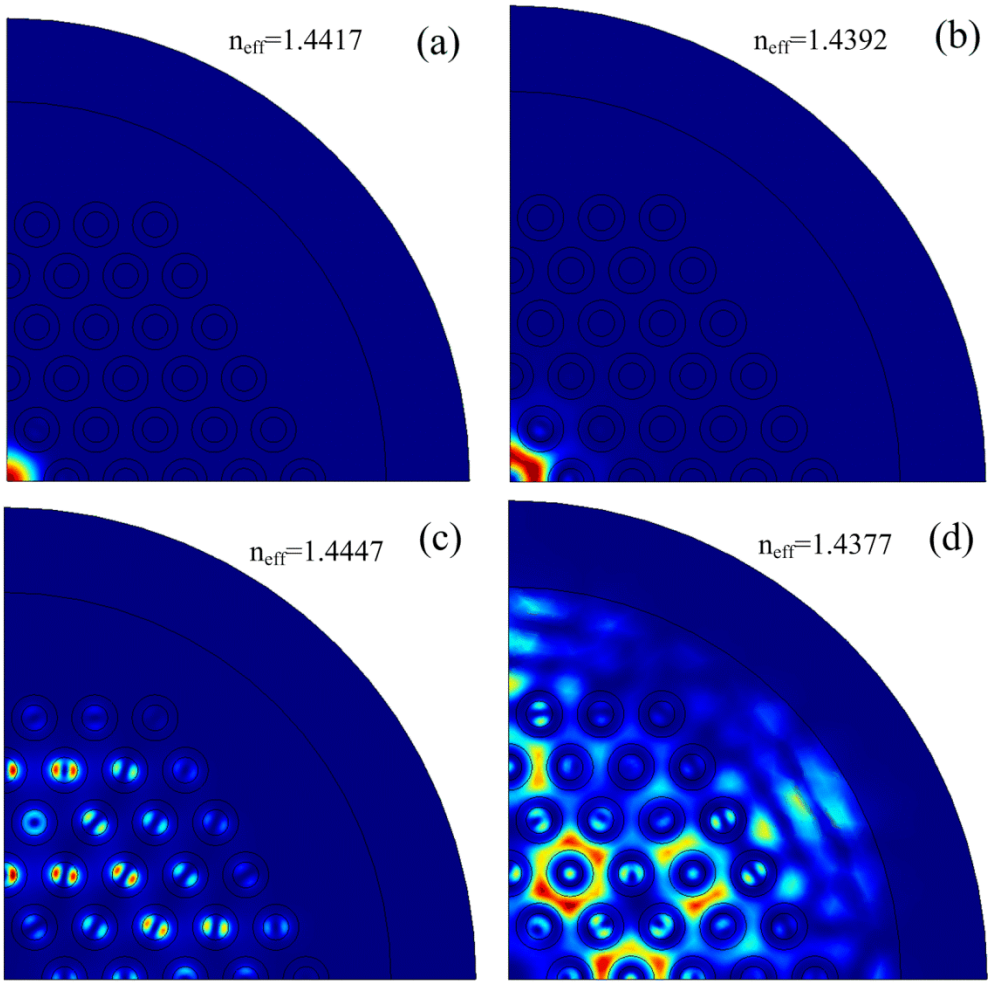


Fig. 4.6 Modal field profiles of (a) $LP_{01}$ core mode (b) $LP_{11}$ core mode (c) guided cladding mode (d) radiated cladding mode.

## 4.3 FBG Inscribed in AS-PBGF

Recently, FBGs have been successfully inscribed into the Ge-doped cladding

cylinders in all-solid PBG hydrogen loaded fibers by use of KrF excimer laser and the grating resonance coupling to the guided $LP_{01}$ cladding mode has been observed, which is much stronger than that between the core modes [12].

We intend to fabricate FBGs around 1550nm based on the resonance between the forward and backward core modes. In this wavelength range, the mode indices of $LP_{01}$ and $LP_{11}$ core modes are calculated to be 1.4417 and 1.4392 *via* COMSOL. Therefore two resonance wavelengths should be observed as long as there is RI modulation in the core. The phase mask used has a pitch value of 1080nm and due to the interference of the ±1 order diffracted beams the obtained fiber grating has a period of 540nm. Thus Bragg resonance is estimated to take place at 1557.0nm and 1554.3nm.

In the experiment, one piece of 3cm length of the PBGF is spliced to the conventional SMFs which are well aligned to minimize the insertion loss and to avoid complicated mode couplings between the high-index cylinders and the fiber core. Owing to the mode field mismatch, the total insertion loss obtained is ~6dB. After splicing, the fiber is exposed to 800nm 120fs laser pulses from a Spectra-Physics spitfire Ti:sapphire amplifier with the repetition rate of 1kHz and the 1/e Gaussian beam radius of 2mm. The experimental setup has been introduced in chapter 3 (see Fig. 3.1). By carefully adjusting the focal line to be located in the fiber core, the grating structure is successfully formed owning to RI modulation in the fiber core.

The transmission spectrum of the FBG is shown in Fig. 4.7. The background loss of the FBG is measured to be ~1dB. Two obvious attenuation peaks A (1563.2nm, 10dB) and B (1564.4nm, 8dB) are observed. The longer wavelength (peak A) can be identified to arise from coupling between the forward $LP_{01}$ core mode and the backward $LP_{01}$ core mode. Peak B attributes to the coupling between the forward $LP_{11}$ core mode and the backward $LP_{11}$ core mode. In the reflection spectrum there is only one reflection peak at 1564.4nm which can be explained by the fact that the reflected

$LP_{11}$ core mode at 1563.2nm is filtered out by the SMF spliced with the AS-PBGF. The small deviations between theoretical and experimental results arise from uncertainties of the geometric parameters of the microstructure. Besides the two strong peaks, a weak one is found in the shorter wavelength of peak A and this peak could be resulting from the radiative cladding mode coupling. The background fluctuation in the spectrum can be explained by the mode interference which is excited by AS-PBGF being spliced with SMFs.

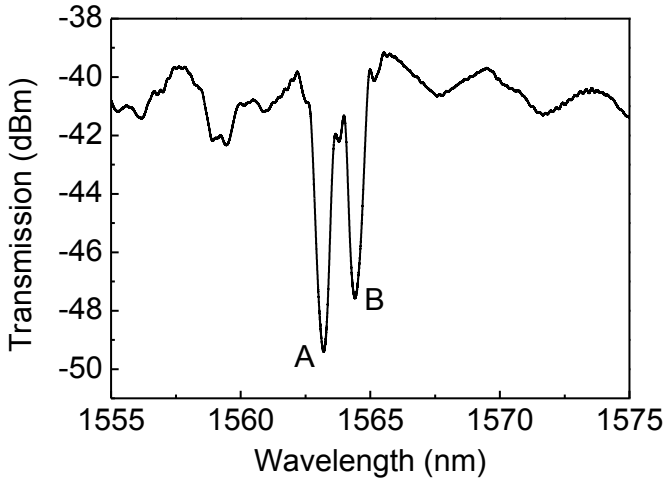


Fig. 4.7 Transmission spectrum of FBG inscribed in AS-PBGF.

Being different from the FBGs inscribed in Ge-doped SMFs, the index modulation is successfully written in the all-silica core of AS-PBGF *via* fs laser irradiation. The damaged index change in pure silica material could be thermally stable at ultrahigh temperature of >1000$^{o}$C. High temperature annealing test has been carried out on the similar FBGs in AS-PBGF, which exhibit good thermal stability [7]. Therefore, this type of FBG might become a superior candidate in the high temperature sensing. Another useful application of AS-PBGF is working as fiber laser cavity by doping some rare-earth element like Er and Yb [13]. The FBG inscribed in the AS-PBGF might become a high-performance reflecting mirror for fiber laser cavity.

## 4.4 LPG Inscribed in AS-PBGF

Recently, LPGs have been successfully fabricated in the cladding cylinders of AS-

PBGF by point-by-point UV illumination and the cladding mode resonance has been observed [14]. Lázaro et al. inscribed LPG in hydrogen loaded AS-PBGFs by mechanical imprinting method and the grating could be tuned by an UV exposure to alter the RI of Ge-doped cylinders [15]. In this part, the LPG is inscribed in AS-PBGF by use of fs laser with line-scanning method, which allows high index modulation in the pure silica without photosensitive doping.

Schematic diagram of the experimental setup for LPG fabrication is shown in Fig. 4.8. One piece of 5cm of the PBGF is spliced to the conventional SMFs with a total insertion loss of ~ 6dB. The fs laser pulses (120fs, 1kHz and 0.8μJ) are employed to fabricate the gratings. The features produced during grating inscription are observed through a CCD camera mounted upon a microscope. The beam is focused into the fiber core by a 20× microscopic objective lens (NA=0.5) and the fiber is fixed on a computer controlled XYZ-translation stage with 40nm resolution. During the inscription process, the stage is moved at a constant speed of along the designed pattern, translating the fiber with respect to the focal point of the beam.

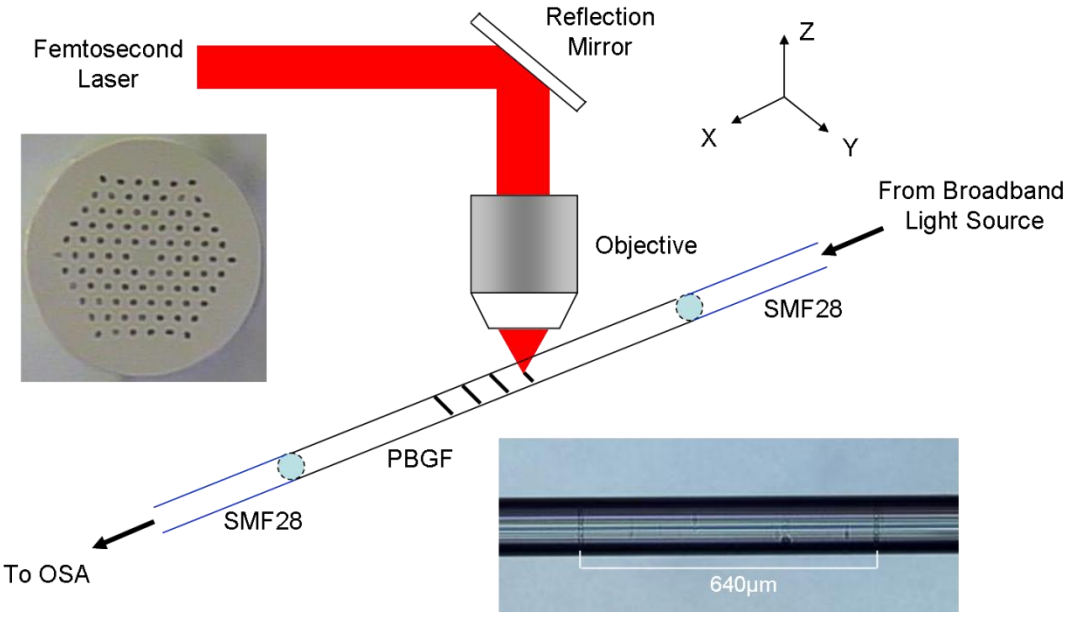


Fig. 4.8 Schematic diagram of the experimental setup for LPG fabrication by use of fs laser with line-scanning method. Insets, optical microscope image of the AS-PBGF end facet and side view of the LPG.

Based on the model analysis, the AS-PBGF used supports both $LP_{01}$ and $LP_{11}$

bandgap-guided core modes. At 1550nm, $n_{eff}$ of the fundamental mode ($LP_{01}$) and higher order core mode ($LP_{11}$) are calculated to be 1.4417 and 1.4392. In order to satisfy phase matching condition between the two core modes around 1550nm, the period of the LPG is chosen to be 640 μm and the grating length is 24mm. One piece of SMF is spliced onto the AS-PBGF to prevent the higher order core mode ($LP_{11}$) coupling from $LP_{01}$ and thus the LPG attenuation band can appear. The transmission spectrum of the LPG is measured in situ by a broadband source and an optical spectral analyzer.

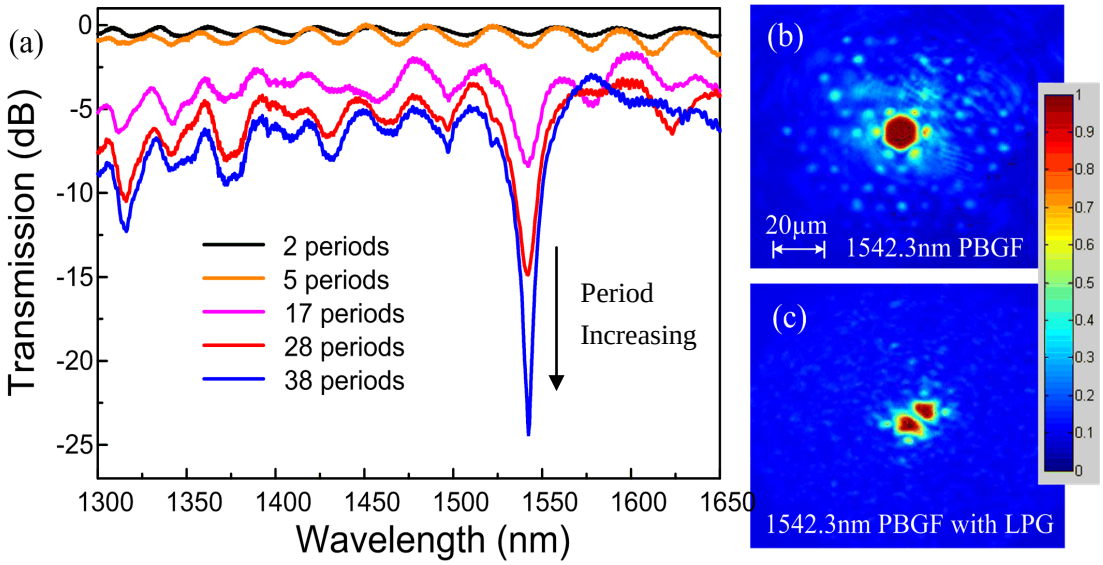


Fig. 4.9 (a) Evolution of the transmission spectrum of LPG with the increase of period number (2~38), the grating pitch is 640 μm. (b) Near-field image in an AS-PBFG without LPG. (c) Near-field image of a LPG at the resonant wavelength of 1542.3 nm with the period number of 38.

Fig. 4.9 shows the transmission spectrum evolution of the LPG within 38 periods. The resonance wavelength of the LPG created is located at 1542.3nm, with a full-width at half-maximum (FWHM) value of ~24nm, and the strongest resonance is measured as ~19dB. The background loss is measured to be around 3dB. At the beginning stage of the inscription (with period number <~5), the interference phenomenon is predominant in the transmission spectrum. The LPG resonance gradually emerges when the period number is increased to ~17, then the mode-coupling efficiency increases rapidly with the increase of the period number. During the inscription process, the interference background and the insertion loss are both enhanced. The

interference fringes are produced by the mode interference between the core mode and the cladding modes in high-index cylinders. To alleviate the interference effect, a longer piece of AS-PBGF can be used in the experiment to weaken the cladding modes by bending the fiber.

From the coupled-mode theory, the intensity of the resonance in an LPG is measured by use of coupling coefficient, which is a function of the index modulation and the mode overlap integral of the coupling mode pairs, as

$$K = \frac{\omega}{4} \iint_{\infty} \Delta\varepsilon \cdot \vec{e}_{core} \cdot \vec{e}_{res}^{*} dxdy \tag{4.1}$$

where $\Delta\varepsilon$ is the perturbation to the permittivity, $\vec{e}_{core}$ and $\vec{e}_{res}^{*}$ denote the transverse mode field of fundamental core mode and resonant mode. In our experiment the region of index modulation is only located in the fs laser focusing point due to multi-photon absorption and avalanche ionization [16]. As displayed in Fig. 4.8, the LPG contained several narrow damage lines across the core as a result of stage movement. The mode overlap between the fundamental core mode and the cladding modes in high-index cylinders over the index-modulation region is too weak to induce resonance. On the contrast, for the energy coupling between guided core modes ($LP_{01}$, $LP_{11}$), the mode overlap is large. Although the electrical field of $LP_{11}$ mode is anti-symmetrical, a large overlap integral can still be achieved as the fs laser induced index modulation is non-uniform in laser - matter interaction region [17]. Thus, only one strong resonance is obtained in the transmission spectrum.

Figs. 4.9 (b) and 4.6(c) illustrate the near-field images of the AS-PBGF at 1542.3nm before and after the LPG inscription, respectively. This is taken by an IR camera and a tunable laser. Before the LPG is inscribed, the light intensity is mainly in the fundamental mode ($LP_{01}$) with a small part (cladding mode) being distributed in the high- index cylinders, especially in the six cylinders being close to the core (Fig. 4.9 (b)). The cladding-mode excitation might be due to the mismatch between PBGF and

the spliced SMF and that is also why the interference fringes can be observed in the transmission spectrum. After the LPG is inscribed most energy in the fundamental mode is coupled to the second order core mode ($LP_{11}$) and the intensity of cladding mode in the high index cylinders is still weak (Fig. 4.9 (c)). The results obtained can further verify the absence of core mode – cladding mode coupling.

Fig. 4.10 shows the polarization dependent loss of the LPG measured by an Agilent 81910A photonic all-parameter analyzer. Being similar to the results reported in the Ref. [18], the PDL graph reveals the peak-trough-peak shape and the two peaks are not equal, which is due to the strong asymmetry of energy deposition in the fiber core. In our case the PDL value reaches 13.2dB around the resonant wavelength, which is much higher than those reported previously by using different fabrication methods and various types of fibers [18-20]. The high PDL is believed to be resulted from a strong azimuthally asymmetric RI change, which is due to the side illumination of the fs laser. Strong PDL is also observed in $CO_2$ laser-induced LPG on air-core PBF that results from collapse of air holes at one fiber side [21].

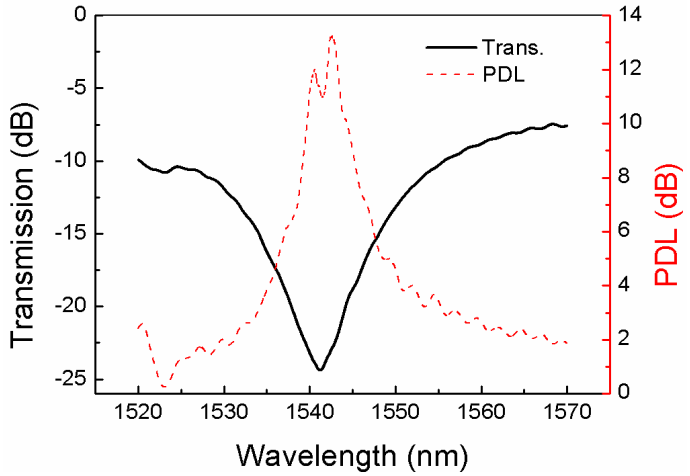


Fig. 4.10 Transmission spectrum and polarization dependent loss of the LPG.

Fig. 4.11 demonstrates the temperature responses of the LPG. The temperature sensitivity of the resonant wavelength is measured to be 17.8pm/$^{o}$C, being much less than those of LPGs written in conventional SMFs [22]. The temperature sensitivity of resonant wavelength can be described as,

$$\frac{d\lambda}{dT}=\left(\frac{d_{neff,1}}{dT}-\frac{d_{neff,2}}{dT}\right)\Lambda+\left(n_{eff,1}-n_{eff,2}\right)\frac{d\Lambda}{dT} \tag{4.2}$$

where $n_{eff,1}$ and $n_{eff,2}$ are the effective indices of two coupling modes and $\Lambda$ is grating pitch. The first part of the right side of the equation describes the thermal-optic effect of material. The two coupling modes are both reside in the same material (all-silica core) so that their effective refractive index change induced by the temperature variation is almost indistinctive. This part is of a very small value so that 'thermal-optic effect' makes little contribution to the increase of temperature sensitivity.

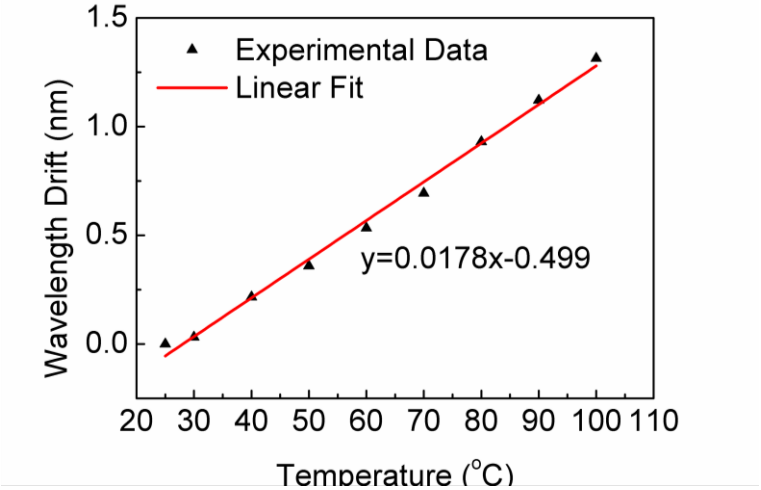


Fig. 4.11 Temperature response.

The wavelength shift as a function of curvature in four orientations is presented in Fig. 4.12. The sign of the change in wavelength shift is determined by bending direction due to one-side writing process; however, the overall sensitivity is very small. When the curvature is increased to 6.5m$^{-1}$, from the initial state of free of bending, the maximum wavelength shift was only 0.96 nm in the most sensitive orientation (270 $^{o}$), which is at least one order of magnitude lower than that of the LPG in conventional SMFs [23, 24]. When the LPG is bent, a strain gradient is established over the fiber cross section however, the fiber core is at the neutral plane where the strain is almost zero. Hence the 'elastic-optic effect' is very weak for the core modes coupling.

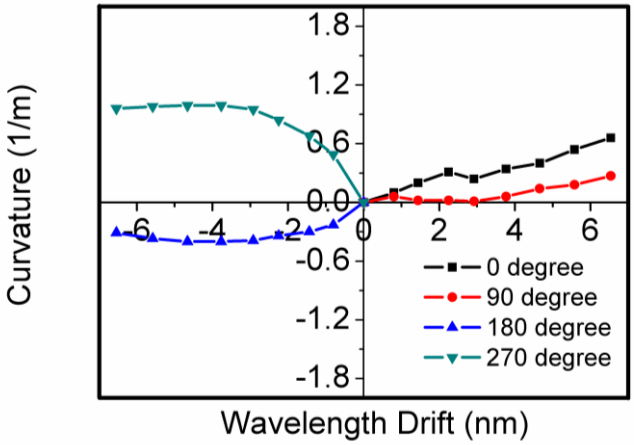


Fig. 4.12 Curvature response.

For tensile strain test as shown in Fig. 4.13, there is a linear 'blue' shift for the resonant wavelength with the increase of applied tensile strain and the measured sensitivity is -1.8 nm/mε.

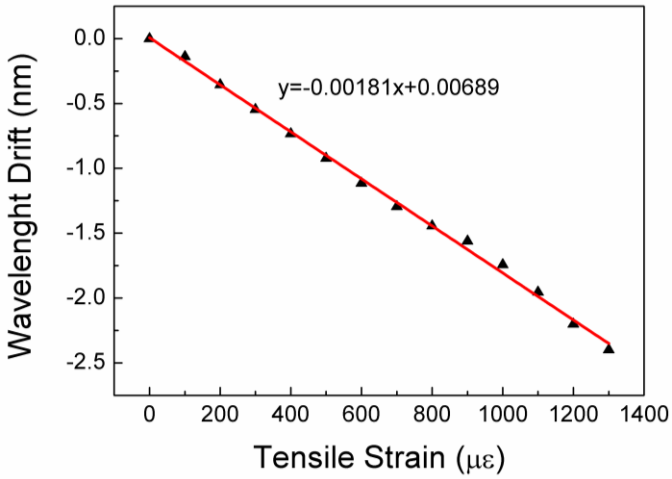


Fig. 4.13 Tensile strain response.

In the external RI test, the LPG was sequentially immerged into the index matching oils with index of 1.30, 1.40, and 1.64. After each test, the LPG was cleaned by using Isopropanol. The results obtained indicate that the resonant wavelength and the peak transmission attenuation are both unchanged. The LPG is insensitive to the external RI because both the $LP_{01}$ and $LP_{11}$ core modes are established by the bandgap effects of the cladding cylinders, which are not affected by the external index. Such insensitivity to external index was also found in $CO_2$ laser induced LPG on air-core PBF for the similar coupling mechanism [21].

## 4.5 Summary

We have investigated the mode profiling for the AS-PBGF *via* the commercial FEM software package COMSOL. The refractive indices of different order core modes are calculated to guide the following experimental fabrication of FBGs and LPGs in the AS-PBGF. FBG was successfully inscribed into the fiber core with no RI modulation on the high-index cylinder lattice. Therefore, we observed only two Bragg resonance peaks corresponding to backward $LP_{01}$ and $LP_{11}$ core modes. In succession LPG was successfully fabricated in AS-PBGF by use of fs laser with line-scanning method. The grating created is precisely located in the core plane with the aid of high precision positioning stage and notable coupling from the fundamental core mode to $LP_{11}$ core mode is achieved without cladding-mode resonances. The LPG fabricated is highly sensitive to tensile strain while being nearly insensitive or only slightly sensitive to temperature, curvature, and external RI.

# Reference

[1] F. Luan, A. K. George, T. D. Hedley, G. J. Pearce, D. M. Bird, J. C. Knight, and P. St. J. Russell, "All-solid photonic bandgap fiber," *Opt. Lett.* vol. 29, pp. 2369-2371 (2004).

[2] A. Argyros, T. A. Birks, S. G. Leon-Saval, C. M. B. Cordeiro, F. Luan, and P. St. J. Russell, "Photonic bandgap with an index step of one percent," *Opt. Express*, vol. 13, pp. 309-314 (2005).

[3] G. B. Ren, P. Shum, L. R. Zhang, X. Yu, W. J. Tong, and J. Luo, "Low-loss all-solid photonic bandgap fiber," *Opt. Lett.*, vol. 32, no. 9, pp. 1023-1025 (2007).

[4] N. M. Litchinitser, A. K. Abeeluck, C. Headley, and B. J. Eggleton, "Anti-resonant reflecting photonic crystal optical waveguides," *Opt. Lett.* vol. 27 pp. 1592-1594 (2002).

[5] T. P. White, R. C. McPhedran, and C. Martijn de Sterke, "Resonance and scattering in microstructured optical fibers," *Opt. Lett.*, vol. 27, no. 22, pp. 1977-1979 (2002).

[6] P. Steinvurzel, B. Kuhlmey, T. White, M. Steel, C. de Sterke, and B. Eggleton, "Long wavelength antiresonant guidance in high index inclusion microstructured fibers," *Opt. Express* vol. 12, pp. 5424-5433 (2004).

[7] Pureur, L. Bigot, G. Bouwmans, Y. Quiquempois, M. Douay, and Y. Jaouen, "Ytterbium-doped solid core photonic bandgap fiber for laser operation around 980 nm," *Appl. Phys. Lett.*, vol. 92, pp. 061113 (2008).

[8] Y. H. Li, D. N. Wang, and L. Jin, "Single-mode grating reflection in all-solid photonic bandgap fibers inscribed by use of femtosecond laser pulses irradiation through a phase mask," *Opt. Lett.*, vol. 34, pp. 1264-1266 (2009).

[9] R: J. Laegsgaard, "Gap formation and guided modes in photonic bandgap fibres with high-index rods," *J. Optics A-Pure Appl. Opt.*, vol. 6, pp.798-804 (2004).

[10] R: T. A. Birks, F. Luan, G. J. Pearce, A. Wang, J. C. Knight, and D. M. Rird, "Bend loss in all-solid bandgap fibers," *Opt. Exp.*, vol. 14, pp. 5688-5698

(2006).

[11] R: G. Ren, P. Shum, L. Zhang, M. Yan, X. Yu, W. Tong, and J. Luo, “Design of all-solid bandgap fiber with improved confinement and bend losses,” *IEEE Photon. Technol. Lett.*, vol. 18, pp. 2560-2562 (2006).

[12] L. Jin, Z. Wang, Q. Fang, Y. Liu, B. Liu, G. Kai, and X. Dong, “Spectral characteristics and bend response of Bragg gratings inscribed in all-solid bandgap fibres,” *Opt. Express*, vol. 15, pp. 15555-15565 (2007).

[13] C. B. Olausson, A. Shirakawa, J. K. Lyngsø, K. P. Hansen, J. Broeng, and K. Ueda, "All-solid photonic bandgap fiber lasers," in Specialty Optical Fibers, OSA Technical Digest (CD) (Optical Society of America, 2011), paper SOWA3.

[14] L. Jin, Z. Wang, Y. Liu, G. Kai, and X. Dong, “Ultraviolet-inscribed long period gratings in all-solid photonic bandgap fibers,” *Opt. Express.*, vol. 16, pp. 21119-21131 (2008).

[15] J. M. Lázaro, B. T. Kuhlmey, J. C. Knight, J. M. Lopez-Higuera, and B. J. Eggleton, “Ultrasensitive UV-tunable grating in all-solid photonic bandgap fibers,” *Opt. Commun.*, vol. 282, pp. 2358-2361 (2009).

[16] J. W. Chan, T. Huser, S. Risbud, and D. M. Krol, “Structural changes in fused silica after exposure to focused femtosecond laser pulses,” *Opt. Lett.*, vol. 26, pp. 1726-1728 (2001).

[17] F. Dürr, H. G. Limberger, R. P. Salathé, F. Hindle, M. Douay, E. Fertein, and C. Przygodzki, “Tomographic measurement of femtosecond-laser induced stress changes in optical fibers,” *Appl. Phys. Lett.*, vol. 84, pp. 4983-4985, (2004).

[18] B. L. Bachim and T. K. Gaylord, “Polarization-dependent loss and birefringence in long-period fiber gratings,” *Appl. Opt.*, vol. 42, pp. 6816-6823 (2003).

[19] C. Caucheteur, A. Fotiadi, P. Mégret, S. A. Slattery, and D. N. Nikogosyan, “Polarization Properties of Long-Period Gratings Prepared by High-Intensity Femtosecond 352-nm Pulses,” *Photon. Technol. Lett.*, vol. 17, pp. 2346-2348, (2005).

[20] G. M. Rego, J. L. Santos, and H. M. Salgado, "Polarization dependent loss of arc-induced long-period fibre gratings," *Opt. Commun.*, vol. 262, pp. 152-156 (2006).

[21] Y. Wang, W. Jin, J. Ju, H. Xuan, H. L. Ho, L. Xiao, and D. N. Wang, "Long period gratings in air-core photonic bandgap fibers," *Opt. Express.*, vol. 16, pp. 2784-2790 (2008).

[22] Bhatia and A. M. Vengsarkar, "Optical fiber long-period grating sensors," *Opt. Lett.*, vol. 21, pp. 692-694 (1996).

[23] T. Allsop, M. Dubov, A. Martinez, F. Floreani, I. Khrushchev, D. J. Webb, and I. Bennion, "Bending Characteristics of Fiber Long-Period Gratings With Cladding Index Modified by Femtosecond Laser," *J. Lightwave Technol.*, vol. 24, pp. 3147-3154 (2006).

[24] Y. J. Rao, Y. P. Wang, Z. L. Ran, and T. Zhu, "Novel Fiber-Optic Sensors Based on Long-Period Fiber Gratings Written by High-Frequency CO2 Laser Pulses," *J. Lightwave Technol.*, vol. 21, pp. 1320-1327 (2003).

# Chapter 5

# Optical Microfiber based Refractive Index Sensors

There has been increased research interest in optical micro and nano fibers in recent years [1-10], because of their many unique and interesting properties. One of the important and advantageous applications of the micro and nano fiber based devices is RI sensing due to the large evanescent wave outside the fiber, which directly interacts with the surrounding environment. Various approaches and configurations have been exploited in recent years such as straight micro and nano fiber [6], twisted polymer nano wires [11], looped and coiled MF [8-10], MZI [12], optical liquid ring resonator [7] and MF based LPG [13, 14].

In this chapter we demonstrate two types of novel RI sensors based on MF. One configuration is the FBG inscribed in MF by using fs laser pulses radiation through a phase mask. The higher-order mode reflection owns a higher RI sensitivity due to its larger evanescent field outside the MF [15]. While the other one is based on a pair of twisted silica MFs which essentially form a coupling device with highly sensitive transmission spectrum to the external RI.

## 5.1 FBG Inscribed in Optical Microfiber

### 5.1.1 Operation Principle

The MF can be regarded as an optical waveguide with a circular cross-section, an infinite thickness air cladding, and a step-index profile [16]. Similar to the weak

guidance optical fibers, the single-mode condition of an air-cladding "strong guiding" MF can be obtained as [17]:

$$V = \frac{\pi \cdot d_{SM}}{\lambda_0} \cdot \sqrt{(n_1^2 - n_2^2)} \approx 2.40 \tag{5.1}$$

The $d_{sm}$ for single mode condition for typical wavelength is listed in Table 5.1.

Table 5.1 $d_{sm}$ for air-cladding silica MFs at typical wavelengths.

| Wavelength (nm) | 325 | 633 | 1064 | 1550 |
|---|---|---|---|---|
| RI of silica | 1.482 | 1.457 | 1.450 | 1.444 |
| RI of air | 1.00 | 1.00 | 1.00 | 1.00 |
| $d_{sm}$ in air (nm) | 228 | 457 | 776 | 1139 |

We take the MF with a diameter of 5μm for example to study its mode property at 1550nm. In this case, tens of higher-order modes besides the fundamental mode can be supported as well. While introducing an FBG in the MF, the periodical index perturbations bring the couplings between the modes. The mode coupling relies on the phase synchronism and the sufficient mode field overlaps in the MF grating region. The phase-matching condition, ensuring a coherent exchange of energy between the modes, is described as [18]:

$$\lambda = (n_{eff,1} + n_{eff,2})\Lambda \tag{5.2}$$

where $\lambda$ denotes the reflected resonance wavelength, $\Lambda$ is the grating period, $n_{eff,1}$ is the effective modal index of incident wave, $n_{eff,2}$ is the effective modal index of grating-coupled reflected wave. The spectrum of MF FBG is due to the grating region in the MF. Only if there is enough modal field overlaps, these modes can be coupled effectively.

## 5.1.2 Fabrication Method

The MF is produced by the use of flame brushing method [19-21] in a simple optical coupler manufacturing system, where a small flame moves slowly under a SMF stretched by two moving vacuum absorption holders. The torch flame intensity can be adjusted by controlling the flux of $H_2$, which is optimized at approximately 134sccm (standard cubic centimeters per minute) in our experiment, just enough to support the flame to soften the glass without inducing a large loss. The scanning length of the torch is ~7mm, which limits the length of the MF. The relative speed of the torch and holders plays an important role in the formation of the MF and its insertion loss. If the speed is high, the fiber diameter becomes large, owing to the limited softening time of the fiber. When the speed is low, a high insertion loss will result, due to the large fiber deformation. Thus, by appropriately control the speed of the flame and the holders, MFs of different diameters exhibiting a loss of less than 0.1dB can be achieved. The scanning speed of torch is set as 1.5mm/s and the moving speed of two holders is set to be 0.225mm/s. Fig. 5.1 clearly shows the SEM image of the tapered silica MF with a diameter of ~3.5μm.

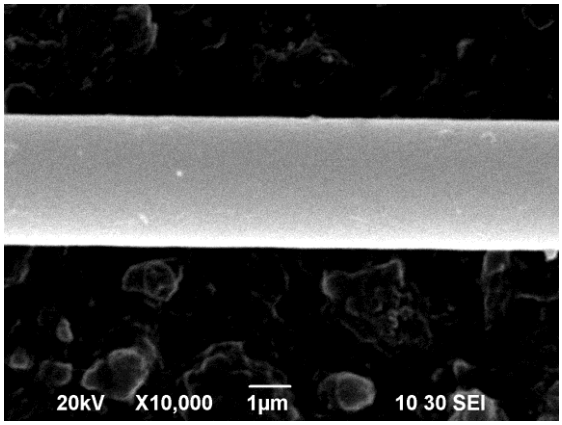


Fig. 5.1 SEM image of a silica MF with a diameter of ~3.5μm.

The fs laser system used for FBG fabrication has been introduced in chapter 3. During the FBG fabrication, the MF is placed in front of a chirped phase mask (Stocker Yale), which is optimized for 800nm illumination, currently available in our laboratory. The microscope image of the FBG fabricated in the MF with diameter of

10 μm is shown in Fig. 5.2.

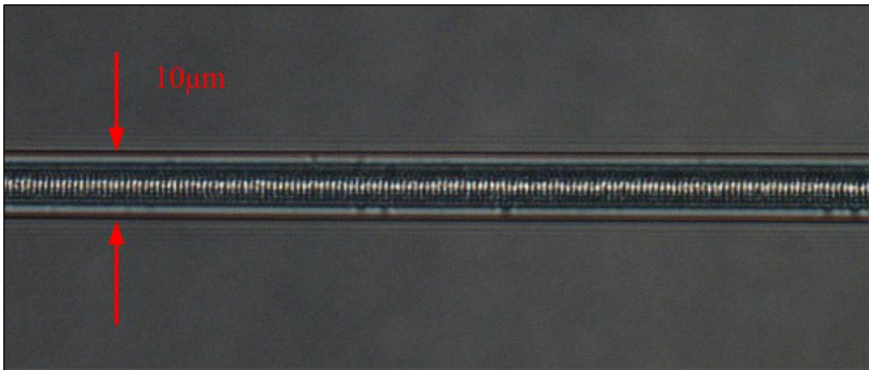


Fig. 5.2 Microscope image of the MF with a diameter of ~10 μm.

Fig. 5.3 demonstrates the reflection spectra of the FBGs in the MFs with different diameters down to 2 μm. The OSA used has the minimum resolution of 0.01nm. It can be seen from the figure that the center wavelength of the FBG is blue shifted with the decrease of the fiber diameter, as more propagating mode energy goes outside the fiber, which causes the reduction of the fiber effective RI [22]. The 3dB bandwidth of the FBG varies from 0.67 to 1.8nm, owing to the variation of fabrication conditions such as the changes in fiber position, laser exposure time and pulse spot size, as well as the chirped phase mask used.

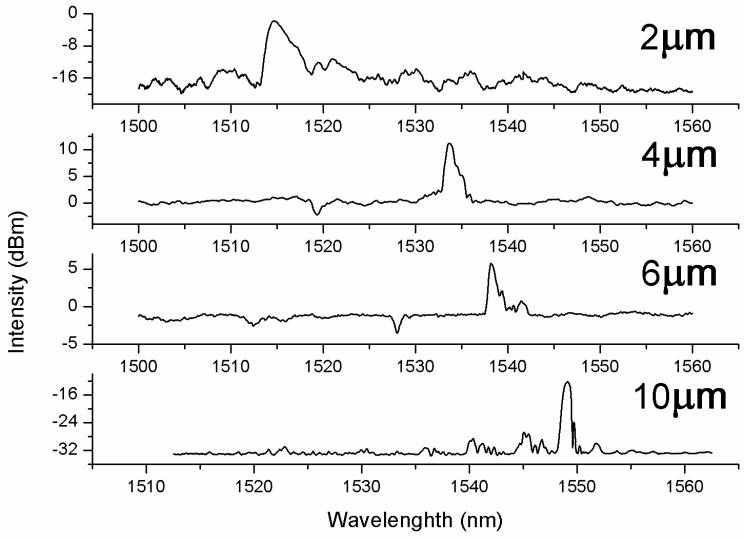


Fig. 5.3 Reflection spectra of the FBGs in MF with diameter of 2, 4, 6 and 10 μm, respectively.

Fig. 5.4 shows the transmission spectrum of the FBG with diameter of 10 μm. Compared with its reflection spectrum shown in Fig. 5.3, where only one fundamental reflection mode appears, nine modes exist in the range between 1512 and 1562nm. The small burrs near the resonance modes may be due to the chirped phase mask used.

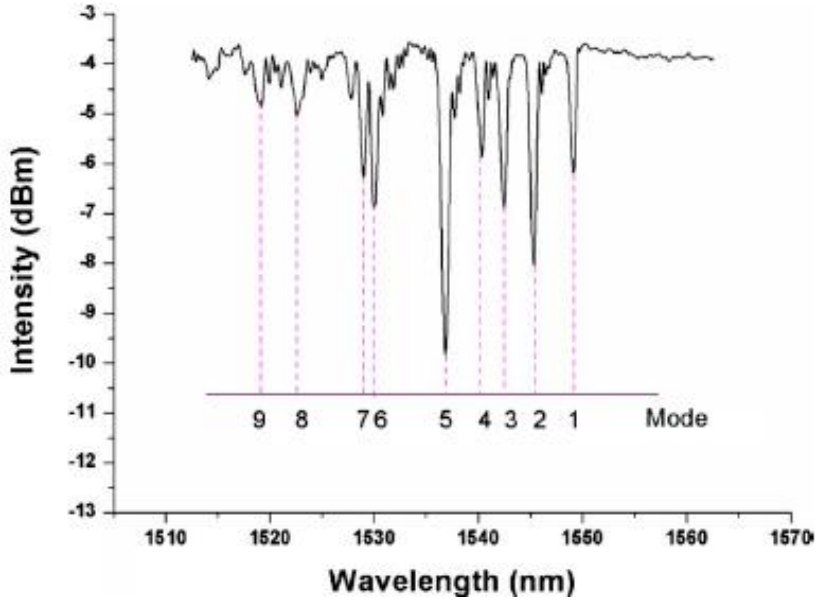


Fig. 5.4 Transmission spectrum of the FBG in MF with a diameter of ~10 μm.

## 5.1.3 Refractive Index Measurement

The external RI measurement by use of the FBG in MF is carried out at the room temperature by immersing the FBG into the liquid with RI values varying from 1.32 to 1.46. Each time after the measurement, the device is rinsed with methanol carefully until the original spectrum is restored and no residue liquid is left. Fig. 5.5 shows the red shift of the transmission wavelength when the ambient RI increases. When the RI is close to the fiber index value, a relative high sensitivity can be obtained, owing to the enhanced influence of the external RI on the propagation mode, which becomes less confined in the fiber.

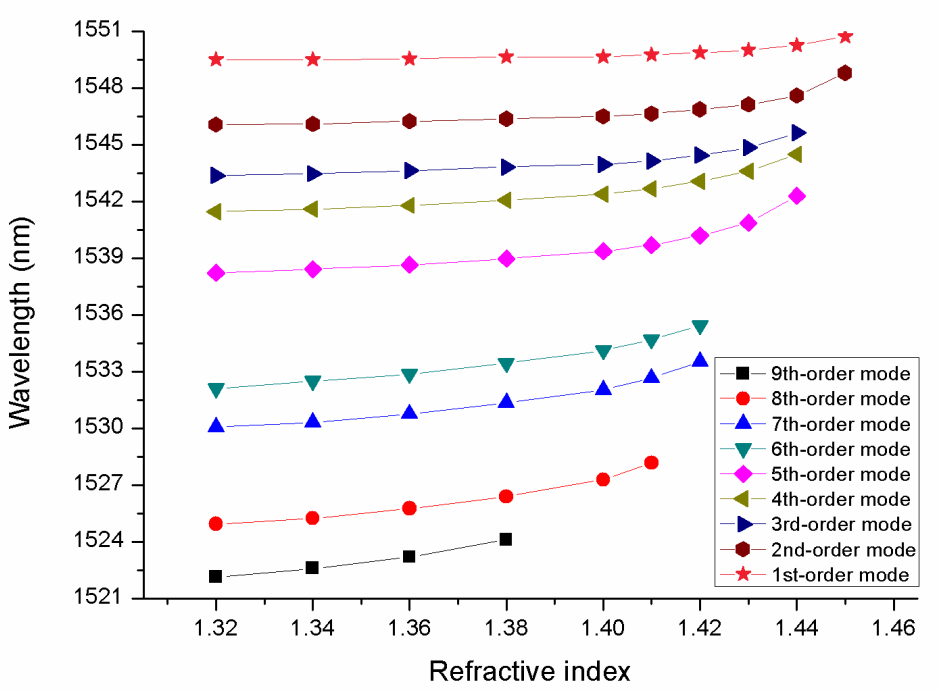


Fig. 5.5 Wavelength change with the external RI at different orders of resonance mode.

The higher order mode which has more energy distributed outside the fiber exhibits the higher sensitivity to the ambient RI. Fig. 5.6 shows the RI sensitivity for different orders of fiber mode when the fiber diameter is ~10 μm. The sensitivity is obtained by calculating the first order derivation of the wavelength shift curve shown in Fig. 5.5, followed by an exponential curve fitting. According to Fig. 5.6, with the same ambient RI, the higher order resonance mode has higher sensitivity compared with the lower order mode. The maximum sensitivity obtained is ~184.6nm/RIU, for the fifth order mode, at the RI value of 1.44. Some higher order modes are disappeared or hardly observed when the ambient RI is increased, as the resonance effect is reduced owing to the less propagation mode energy confined in the fiber.

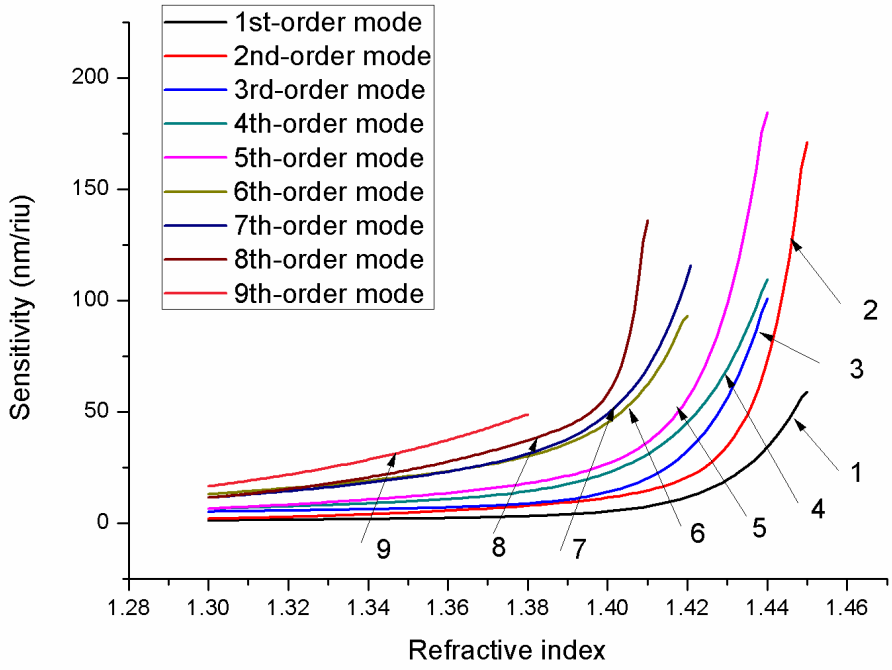


Fig. 5.6 RI sensitivity of different orders of mode for the FBG in MF with a diameter of ~10 μm.

The RI response of the FBG with a diameter of ~2 μm was also investigated. The result, as shown in Fig. 5.7, indicates the maximum sensitivity obtained is ~231.4nm/RIU for the first order mode at the RI value of 1.44.

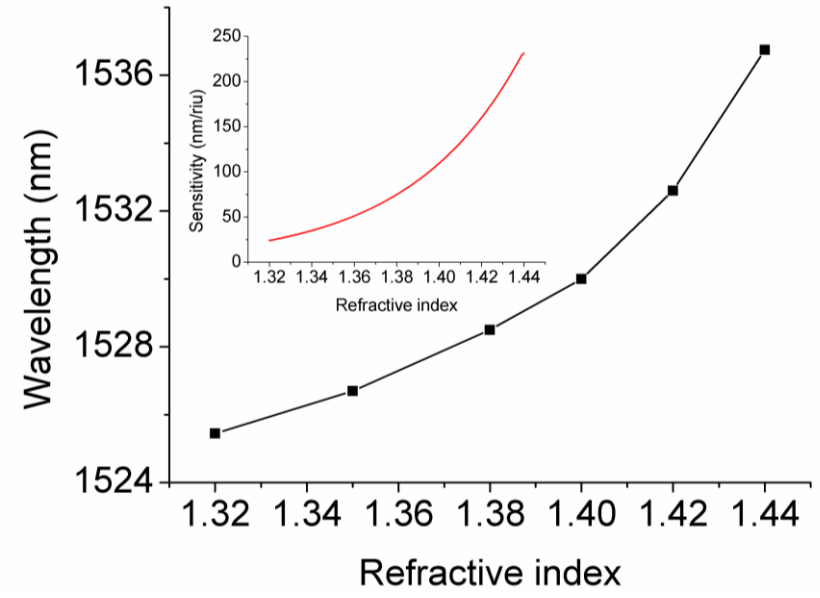


Fig. 5.7. Wavelength shift with the external RI at the first order mode for the FBG in MF with a diameter of ~2 μm. Inset, RI sensitivity of the first order mode.

The proposed RI sensor based on the different-order mode reflection of an MF FBG owns compact size, high sensitivity, low cost and great multiplexing capability, as well as the convenience of sensing head operating. In the development of proposed idea into practical devices, some challenges need to be addressed. The grating structure is formed based on damage of silica MF which has a very small diameter so that the mechanical strength of the device is weak and easily cracked in practical use. Moreover, their optical performance quickly degrades after fabrication due to surface scattering from dust particles and from cracks induced by water vapor, resulting in large irrecoverable increases in loss. An effective encapsulation method is needed to overcome these key impediments and researchers have done many tries in this field, including encapsulation in polymers such as Teflon and in transparent hydrophobic silica aerogel.

## 5.2 Twisted Optical Microfiber Coupler

### 5.2.1 Fabrication Method

The MFs were fabricated by flame-heated taper-drawing of a SMF. To construct a coupling device, a section of straight MF was mounted between two fiber holders, and another section of MF of the same size was twisted along the straight MF by means of micromanipulation. Due to the van der Waals force and the electrostatic force, the two MFs were tightly attracted by each other and as a result, an energy coupling region was created. Such a coupler was placed on an aluminum substrate and fixed by use of adhesive at both ends. Fig. 5.8(a), (b) and (c) show the schematic diagram of the twisted MF coupler, the microscope image and the SEM image of the twisted region, respectively.

By adjusting the number of turns of twist, the coupling length could be changed until

a desired transmission spectrum was obtained for sensor use. Since the periodic length of the twist is not exactly a constant, the variation of coupling condition along our coupler may lead to inhomogeneous spectrum. The reproducibility problem is commonly existed in the MF based devices. The power coupling between the two MFs is sensitive to their twist structure. In order to ensure a high degree of reproducibility, a more accurate twist device and a better control of the MF size are required. A similar MF coupler has been achieved by tapering two SMFs and fused them together to maintain the operation stability. The price paid, however, is the lack of structure flexibility [3]. On contrary, our device has a flexible structure as the fiber size and the twist length are both adjustable for different applications.

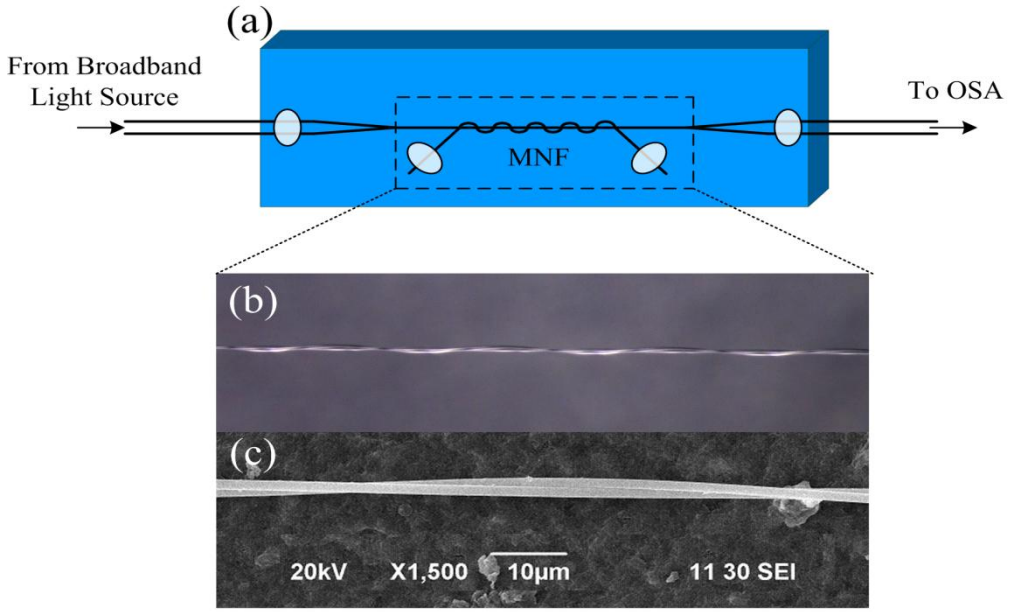


Fig. 5.8. (a) Schematic diagram of the twisted MF coupler; (b) Optical microscope image of the twist region in magnification of ×200; (c) SEM image of the twist region.

## 5.2.2 Operation Principle

The MF is fabricated by adiabatically tapering of SMF, which supports single-mode guidance [23]. Therefore the operating principle of the twisted MF coupler is similar

to that of the well-established fused-type optical fiber coupler, the power oscillation between the two arms of the coupler results from the modal interference between the lower-order symmetric and the anti-symmetric supermodes. For the pair of MFs with the same diameter, the period of the sinusoidal modulation in the transmission spectra decreases with the increase of twist length. This can be explained by the evanescent field coupling equation

$$P(\lambda) = P_0 \cos^2(\kappa L) \tag{5.3}$$

where $P_0$ and $P(\lambda)$ denote the input and output power respectively, $L$ is the coupling length, i.e. the twist length, and $\kappa$ represents the coupling coefficient. When the coupler structure is fixed, its transmission spectrum becomes a function of external RI, with the dip wavelengths satisfying the relation

$$\kappa(\lambda_{dip}) = (2m-1)\pi/2L \tag{5.4}$$

Where $\lambda_{dip}$ stands for the dip wavelength and m is a positive integer.

When the MF coupler is immerged in liquid for RI measurement, the index difference between silica waveguide and liquid environment is rather small and the weak guidance can be used. Thus, the empirical formula of the coupling coefficient can be described as [24]

$$\kappa(\lambda) = \frac{\pi V}{2k_0 n_1 a^2} \exp[-(c_0 + c_1 \bar{d} + c_2 \bar{d}^2)] \tag{5.5}$$

$$c_0 = 5.2789 - 3.663V + 0.3841V^2$$

$$c_1 = -0.7769 + 1.2252V - 0.0152V^2$$

$$c_2 = -0.075 - 0.0064V - 0.0009V^2$$

where $V = k_0 a\sqrt{n_1^2 - n_2^2}$, $n_1$ and $n_2$ are the RI of the fiber material and the external medium, $a$ is the fiber radius, $d$ is the absolute distance between the

two fibers and $\bar{d} \equiv d / a$.

There is a linear relationship between the dip wavelength shift and the coupling coefficient whereas the coupling coefficient and the external RI exhibit a complicated nonlinear relationship. Thus the dip wavelength is varied nonlinearly with the RI.

## 5.2.3 Refractive Index measurement

The experimental setup is shown schematically in Fig. 5.9. The packaged sensor head was immersed into a container with prepared isopropanol solution whose RI could be reduced by adding amount of pure water and increased by adding pure isopropanol. The temperature of liquids needs to be kept identical in the experiment to avoid any temperature impact. Firstly, these two solutions were placed in room temperature for some time to ensure the same initial temperature. Secondly, after mixture, the solution container was deposed in a closed environment to prevent temperature fluctuation resulting from air flow. The RI of the solution was measured by a refractometer (Sino TDR095C) with a resolution of 0.001RIU. During each of the measurement steps, the solution was kept at a standstill for 5 minutes, to ensure the uniformity of the solution concentration.

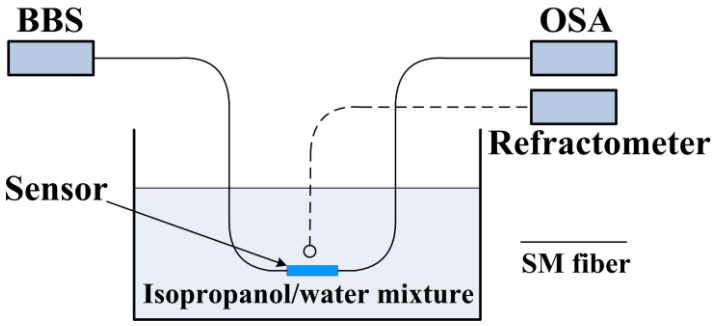


Fig. 5.9 Schematic diagram of experimental setup for RI measurement.

It is well-known that when the fiber diameter is decreased, a larger fraction of

guided mode field appears as the evanescent wave, which makes the optical energy exchange between the two fibers be easily taken place. Thus, MFs with different diameters were used in our system to compare their RI sensitivities.

The sensor was firstly assembled by two twisted MFs with the diameter of ~4.2μm. The transmission spectra corresponding to different twist lengths are demonstrated in Fig. 5.10(a). It can be found that when the twist length reaches ~4.5mm, a spectral modulation envelop is clearly observed, resulting from the coupling of two polarization eigenstates [25]. The inset of Fig. 5.10(a) shows the SEM image of the twisted MFs.

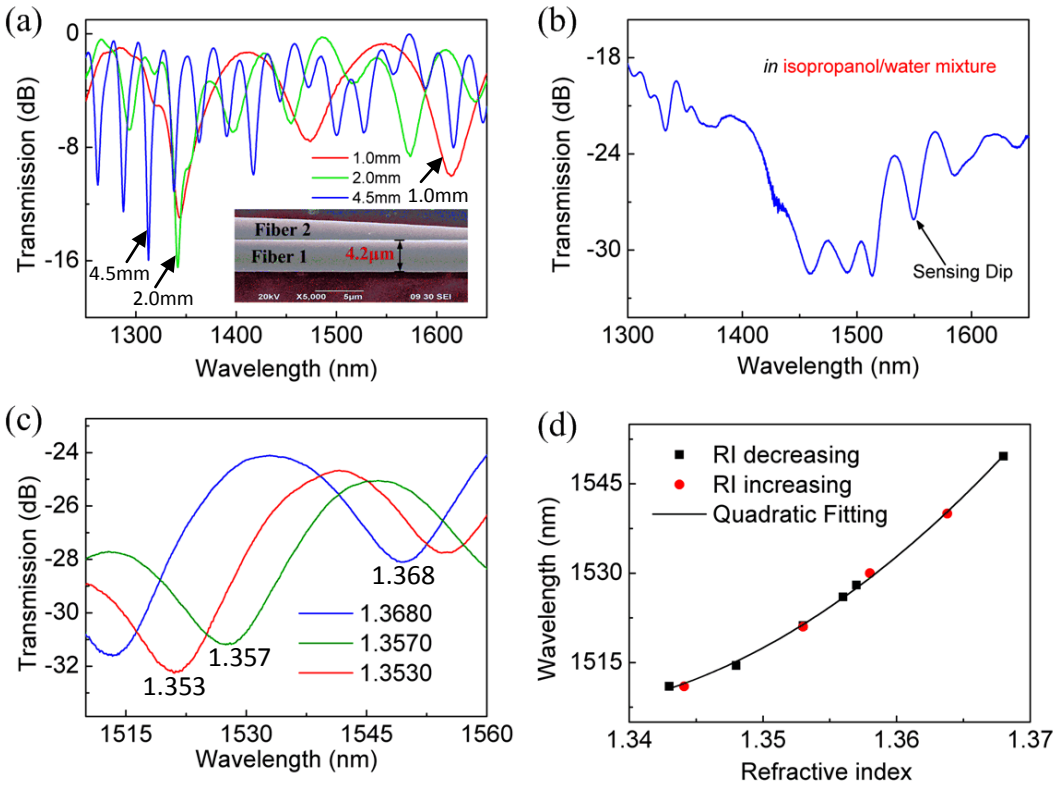


Fig. 5.10 (a) Transmission spectra of the twisted MFs with the diameter of ~4.2μm corresponding to different coupling lengths of 1, 2 and 4.5mm, respectively. Inset, SEM image of the sensor; (b) Transmission spectrum in isopropanol / water solution with the RI of 1.3680 and the volumetric proportion of 15:1; (c) Transmission spectra for different values of RI; (d) Quadratic fitting showing the relationship between the dip wavelength and the RI.

The transmission spectrum of the sensor in the isopropanol / water solution is shown in Fig. 5.10(b), where the sinusoidal modulation is largely submerged and one spectral dip at ~1550nm is used for RI measurement. When the device is immerged into the solution, the insertion loss induced is ~18dB. In Fig. 5.10(c) the transmission spectra in various RI solutions are demonstrated. The shift of dip wavelength as a function of external RI is displayed in Fig. 5.10(d) where the measurement is performed in a cycle, by decreasing and increasing the RI respectively, and the results obtained confirm the reproducibility of the measurement. The black line in Fig. 5.10(d) is a quadratic fitting for the data labeled by black squares (correlation coefficient R = 0.9984). The maximum sensitivity is estimated to be -2377nm/RIU at the RI value of 1.3680.

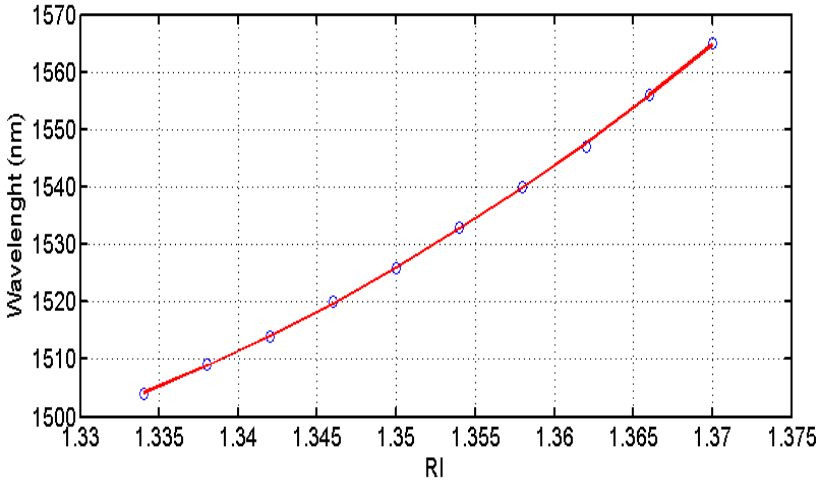


Fig. 5.11 Simulated relationship between surrounding RI and wavelength shift of the dip around 1550nm in a twisted MF coupler with fiber radius of 2.1μm and coupling length of 4.5mm.

Theoretical calculation is carried out based on the evanescent field coupling equation (5.3), where fiber radius ($a$) is set as 2.1μm; RI of fiber material ($n_1$) is 1.444; coupling length ($L$) is 4.5mm; absolute distance between two fibers is 4.2μm. Fig. 5.11 shows the simulated relationship between surrounding RI and wavelength shift of the dip that is closest to the sensing dip in the experiment.

The simulation result shows a similar wavelength-shift trend and RI sensitivity comparing with the experiment result in Fig. 5.10(d).

In the second experiment, the MFs have the diameter of ~2.8μm and the twist length is ~6mm. The SEM image appearing in the inset of Fig. 5.12(a) clearly demonstrates the details of twist. It can be found from the RI measurement that a large insertion loss of ~23dB exists in the isopropanol / water solution as shown in Fig. 5.12(b). This is due to the fact that with the decrease of MF diameter, the guided mode effective RI goes down, which reduces the RI difference between the guided mode and the surrounding medium, hence weakens the confinement of the guided light in MF and results in the large insertion loss. The transmission spectra in various RI solutions are displayed in Fig. 5.12(c) while the results of RI measurement are demonstrated in Fig. 5.12(d). Similarly, a quadratic fitting (black line) of the recorded data corresponding to the decrease of RI (black squares) yields a good correlation coefficient R = 0.9931. The maximum sensitivity obtained is -2735nm/RIU at the RI value of 1.3680.

The enhanced RI sensitivity attributes to the reduced MF diameter. Since the physical overlap between the guided mode field and the surrounding liquid increases with the decrease of MF diameter, the coupling condition, i.e. the coupling coefficient, should be more susceptible to the external RI change for the MF with a smaller diameter. However, with the decrease of MF diameter, the insertion loss of the device increases.

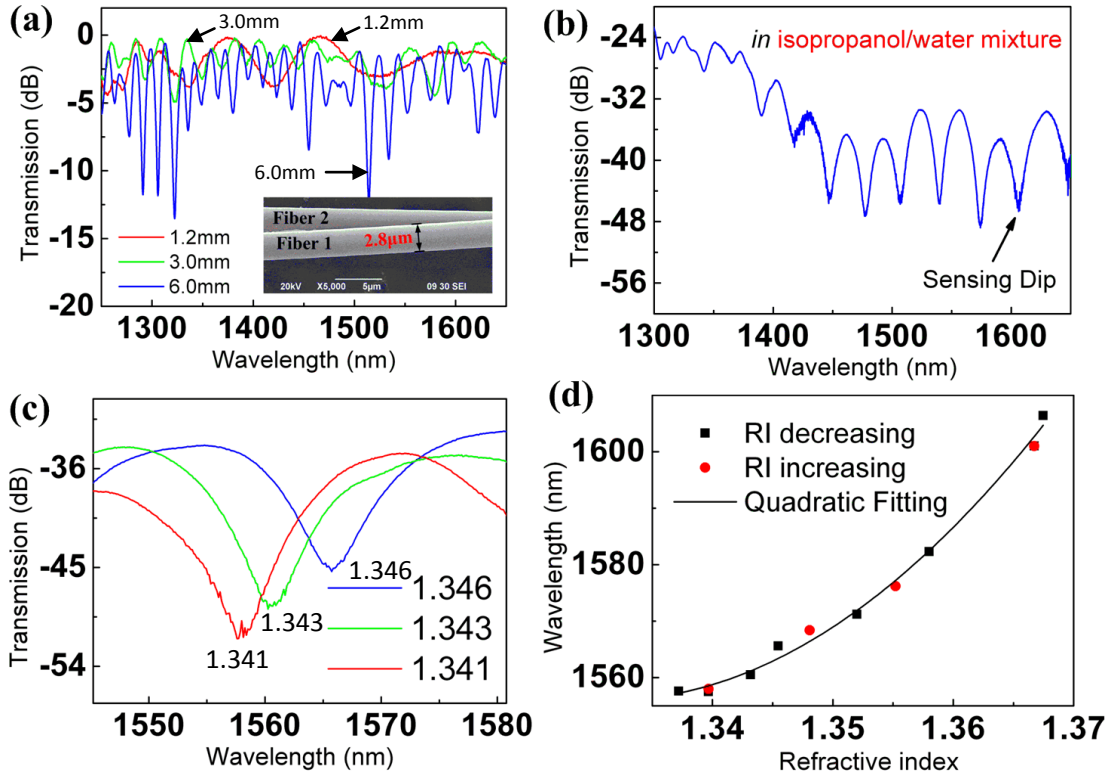


Fig. 5.12 (a) Transmission spectra of the twisted MFs with the diameter of 2.8μm corresponding to different coupling lengths of 1.2, 3 and 6mm, respectively. Inset: SEM image of the sensor; (b) Transmission spectrum in isopropanol / water solution whose RI is 1.3680 and volumetric proportion is about 15:1; (c) Transmission spectra for different values of RI; (d) Quadratic fitting showing the relationship between the dip wavelength and the RI.

The result of theoretical simulation of such MF coupler is shown in Fig. 5.13. The calculated dip-wavelength shift is in an acceptable agreement with experiment data just with a small difference that can be explained by the error in parameters setting.

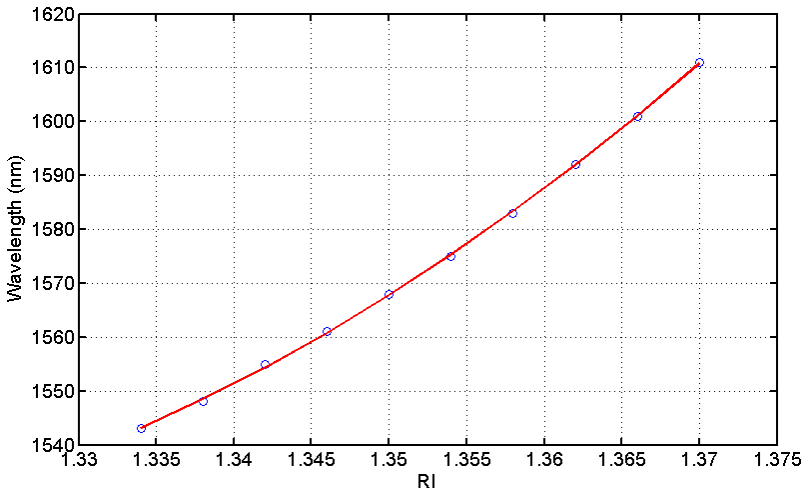


Fig. 5.13 Simulated relationship between surrounding RI and wavelength shift of the dip around 1550nm in a twisted MF coupler with fiber radius of 1.4μm and coupling length of 6mm.

Various approaches based on MF have been exploited for RI sensing, including microfluidic channel, optical liquid ring resonator, MF loop and coil, as well as twisted polymer nanowires. The RI sensitivity values of these MF based devices are summarized in Table 5.2.

Table 5.2 Different types of MF refractometric sensors

| Sensor configuration | RI sensitivity |
|---|---|
| Optical liquid ring resonator [7] | 800 nm/RIU |
| MF loop [8] | 109.7 nm/RIU |
| MF coil resonator [9] | 160 nm/RIU |
| MF coil resonator with a fluidic channel [10] | 40 nm/RIU |
| Twisted polymer nanowires [11] | 26.96 mW/RIU |

Comparing with the above refractometric sensors, our design is featured with easy fabrication, compact size and high RI sensitivity. In the other side, the sensor cannot provide absolute RI value but a relative one so that this scheme is more suitable for measurement of known liquids like salinity of sea water. Furthermore, the bare MFs are easily contaminated by environment and the

increased propagation loss from each RI test will dramatically shorten its lifetime. This is one problem crying out for solutions for all MF-based devices. In practical sensor system the spectrum needs to be well demodulated to obtain measurand information. The transmission spectrum of this sensor is complicated and contains many peaks that will involve certain difficulties in demodulation.

## 5.3 Summary

Two RI sensors based on MF is proposed and demonstrated experimentally. The first sensor configuration is an FBG inscribed in MF by use of fs laser radiation through a phase mask. The maximum sensitivity obtained for the first order mode is ~231.4nm/RIU, at the RI value of ~1.44, when the fiber diameter is ~2μm. To the best of our knowledge it is the first time to obtain FBG in a MF.

The second one is developed by twisting a pair of silica MFs to form a coupling device. The transmission spectrum of the device is highly sensitive to the surrounding RI and the highest sensitivity obtained is -2377nm/RIU, at the RI value of 1.3680, for the fibers with diameter of ~4.2μm, and the sensitivity can be further increased to -2735nm/RIU for a smaller fiber diameter of ~2.8μm. Such a device is featured with easy fabrication, compact size and much higher RI sensitivity.

For RI sensing in real field applications, the temperature cross-sensitivity would lead to an unreliable measurement and so it is critical that temperature and RI should be simultaneously and unambiguously measured. In the next chapter a dual-parameter sensor is developed.

# Reference

[1] J.C. Knight, G. Cheung, F. Jacques, T. A. Birks, “Phase matched excitation of whispering-gallery mode resonances by a fiber taper,” *Opt. Lett.* vol. 22, pp. 1129-1131, (1997).

[2] L. M. Tong, R. R. Gattass, J. B. Ashcom, S. L. He, J. Y. Lou, M. Y. Shen, I. Maxwell, E. Mazur, “Subwavelength-diameter silica wires for low-loss optical wave guiding,” *Nature* vol. 426, pp. 816-819, (2003).

[3] Y. M. Jung, G. Brambilla, D. J. Richardson, “Optical microfiber coupler for broadband single-mode operation,”*Opt. Express* vol. 17, pp. 5273-5278, (2009).

[4] X. Jiang, Y. Chen, G. Vienne, L. M. Tong, “All-fiber add-drop filters based on MNF knot resonators,” *Opt. Lett.* vol. 32, pp. 1710-1712, (2007).

[5] M. Sumestsky, “Optical MNF coil delay line,” *Opt. Express* vol. 17, pp. 7196-7205, (2009).

[6] P. Polynkin, A. Polynkin, N. Peyghambarian, M. Mansuripur, “Evanescent field-based optical fiber sensing device for measuring the refractive index of liquids in microfluidic channels,” *Opt. Lett.* vol. 30, pp. 1273-1275, (2005).

[7] M. Sumetsky, R. S. Windeler, Y. Dulashko, X. Fan, “Optical liquid ring resonator sensor,” *Opt. Express* vol. 15, pp. 14376-14381, (2007).

[8] X. Guo, L. M. Tong, “Supported MNF loops for optical sensing,” *Opt. Express* vol. 16, pp. 14429-14434, (2008).

[9] M. Sumetsky, Y. Dulashko, S. Ghalmi, “Fabrication of miniature optical fiber and MNF coils,” *Opt. Laser Eng.* vol. 48, pp. 272-275, (2010).

[10] F. Xu, G. Brambilla, “Demonstration of a refractometric sensor based on optical MNF coil resonator,” *Appl. Phys. Lett.* vol. 92, pp. 101126 (2008).

[11] H. Zhu, Y. Q. Wang, B. J. Li, “Tunable refractive index sensor with ultracompact structure twisted by poly(trimethylene terephthalate)

nanowires," *ACS Nano* vol. 3, pp. 3110-3114, (2009).

[12] P. H. Wu, C. H. Sui, and B. Q. Ye, "Modelling nanofiber Mach-Zehnder interferometers for refractive index sensors," *J. Mod. Opt.* vol. 56, pp. 2335-2339, (2009).

[13] H. F. Xuan, W. Jin, M. Zhang, "$CO_2$ laser induced long period gratings in optical MNFs," *Opt. Express* vol. 17, pp. 21882-21890, (2009).

[14] H. F. Xuan, W. Jin, S. J. Liu, "Long-period gratings in wavelength-scale microfibers," *Opt. Lett.* vol. 35, pp. 85-87, (2010).

[15] X. Fang, C. R. Liao, D. N. Wang, "Femtosecond laser fabricated fiber Bragg grating in MNF for refractive index sensing," *Opt. Lett.* vol. 35, pp. 1007-1009, (2010).

[16] L. M. Tong, J. Y. Lou, and E. Mazur, "Single-mode guiding properties of subwavelength-diameter silica and silicon wire waveguides," *Opt. Express* vol. 12, pp. 1025-1035, (2004).

[17] A. W. Snyder, J. D. Love, "Optical waveguide theory," *Chapman and Hall*, New York, (1983).

[18] T. Erdogan, "Fiber grating spectra," *J. Lightwave Technol.* vol. 15, pp. 1277-1294, (1997).

[19] G. Brambilla, V. Finazzi, and D. Richardson, "Ultra-low-loss optical fiber nanotapers," *Opt. Express* vol. 12, pp. 2258-2263, (2004).

[20] Y. lizé, E. Mägi, V. Ta'eed, J. Bolger, P. Steinvurzel, and B. Eggleton, "Microstructured optical fiber photonic wires with subwavelength core diameter," *Opt. Express* vol. 12, pp. 3209-3217, (2004).

[21] F. Bilodeau, K. O. Hill, S. Faucher, and D. C. Johnson, "Low-loss highly overcoupled fused couplers: fabrication and sensitivity to external pressure," J. *Lightwave Technol.* vol. 6, pp. 1476-1482, (1988).

[22] A. Iadicicco, A. Cusano, A. Cutolo, R. Bernini, and M. Giordano, "Thinned

fiber Bragg gratings as high sensitivity refractive index sensor," *IEEE Photon. Technol. Lett.* vol. 16, pp. 1149-1151, (2004).

[23] Y. M. Jung, Y. C. Jeong, G. Brambilla, D. J. Richardson, "Adiabatically tapered splice for selective excitation of the fundamental mode in a multimode fiber," *Opt. Lett.* vol. 34, pp. 2369-2371, (2009).

[24] R. Temari, K. Thyagarajan, "Analysis of tunable single-mode fiber directional couplers using simple and accurate relations," *IEEE J. Lightwave Technol.* vol. 4, pp. 386-390, (1986).

[25] M. S. Yataki, D. N. Payne, M. P. Varnham, "All-fiber polarizing beam splitter," *Electron. Lett.* vol. 21, pp. 249-251, (1985).

# Chapter 6

# Mach-Zehnder Interferometer embedded in an FBG

Optical fiber sensors for simultaneous RI and temperature measurement can be achieved by: (a) employing single sensing element such as slanted FBG [1], high birefringence D-type fiber loop mirror [2] and intrinsic Fabry-Perot interferometer [3], with the disadvantages of small RI sensitivity [1, 2], or low measurement accuracy [3]; (b) adopting a combination of multiple sensor elements such as a hybrid structure of FBG and LPG [4], a sandwiched structure of LPGs [5], dual FBGs connected by a multi-mode fiber taper [6], or a pair of FBGs coated with different polymers [7], with the price paid of large system size and hence inaccurate sensing location. In general, the desirable properties such as extremely high RI sensitivity, low temperature cross-sensitivity, precise sensing location and compact sensor head cannot be simultaneously achieved in the above mentioned systems.

An efficient technique for miniaturized fiber sensor fabrication is using fs laser micromachining, which can create interferometer cavity inside the fiber with ultra-high accuracy [8, 9]. In this chapter, we present a compact optical fiber RI sensor based on a MZI embedded in an FBG. Since the MZI fringe is extremely sensitive to the cavity RI [10, 11] and the resonant wavelength of the FBG is essentially insensitive to the RI change, while both are temperature dependent, a simultaneous and unambiguous RI and temperature sensing can be achieved.

# 6.1 Operation Principle

FBG is widely used in temperature sensors and its temperature response can be described as:

$$d\lambda_{FBG}/dT = \lambda_{FBG} \cdot (\xi_{core} + \alpha) \tag{6.1}$$

Where $\xi_{core}$ is the thermo-optic coefficient, ~ $8.6\times10^{-6}$/°C and $\alpha$ is the thermal-expansion coefficient, ~$0.55\times10^{-6}$/°C for Corning SMF-28 fiber. But the FBG on single mode fiber is usually insensitive to ambient RI for the working mode being confined in the core.

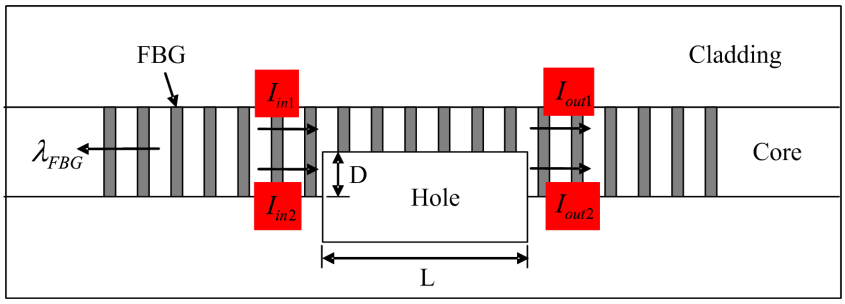


Fig. 6.1 Schematic diagram of the sensor based on a MZI embedded in FBG

By removing part of the core near the core and cladding interface, a fiber in-line MZI can be constructed and schematic diagram of the sensor is shown in Fig. 6.1. The light wave propagating along the fiber core is split into two beams, denoted by $I_{in1}$ and $I_{in2}$. One beam remains propagating in the core while the other travels through the cavity. When the two output beams, $I_{out1}$ and $I_{out2}$, are recombined in the core, interference takes place due to the phase difference ($\delta$) induced by the effective RI difference between the fiber core and the cavity. The output intensity can be described as:

$$I = I_{out1} + I_{out2} + 2\sqrt{I_{out1}I_{out2}}\cos(\delta + \phi_0) \tag{6.2}$$

Where $\phi_0$ is the initial phase, and $\delta = 2\pi L\Delta n/\lambda$ is the phase difference of the interferometer, $L$ is the path length and $\Delta n$ is the RI difference between the two arms, i.e. $\Delta n = n_{eff}^{core} - n_{eff}^{cavity}$, and $\lambda$ is the wavelength. Considering the bottom-peak value of the interference signal, we obtain

$$2\pi L\Delta n/\lambda_{m(MZI)} + \phi_0 = (2m+1)\pi \tag{6.3}$$

where $m$ is an integer and $\lambda_{m(MZI)}$ is the central wavelength of the $m$-th order interference dip.

Assuming $L$ is a constant, i.e. ignoring the small thermal expansion and contraction of interferometer cavity, the temperature response of the MZI device can be obtained as:

$$\frac{d\lambda_{m(MZI)}}{dT} = \frac{\lambda_{m(MZI)}}{n_{eff}^{core} - n_{eff}^{cavity}}(\xi_{core} - \xi_{cavity}) \tag{6.4}$$

where $\xi_{core}$ and $\xi_{cavity}$ are thermo-optic coefficients of fiber core and the cavity medium respectively. Similarly, the RI response can be described as:

$$\frac{d\lambda_{m(MZI)}}{dn} = \frac{\lambda_{m(MZI)}}{n_{eff}^{core} - n_{eff}^{cavity}}\left(\frac{dn_{eff}^{core}}{dn} - \frac{dn_{eff}^{cavity}}{dn}\right) \tag{6.5}$$

## 6.2 Fabrication Method

An FBG was firstly inscribed in SMF by use of fs laser irradiation through a phase mask and the length of the inscribed grating was ~4 mm. In succession a MZI cavity was drilled by fs laser micromachining. Fig. 6.2 shows the experimental setup for MZI fabrication.

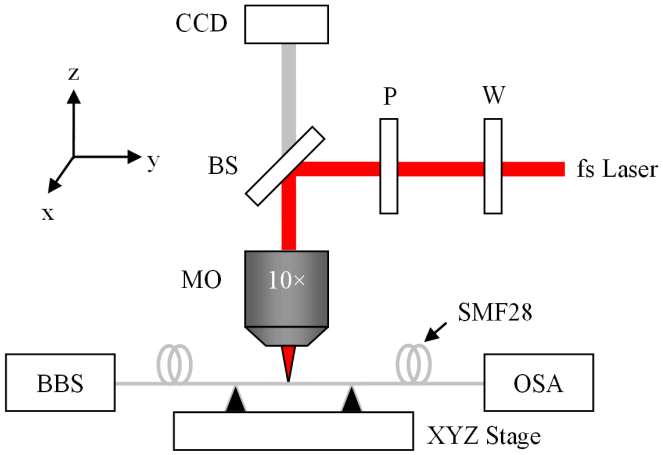


Fig. 6.2 Experimental setup. CCD: charge-coupled device camera; W: half wave plate; P: polarizer; BS: beam splitter; MO: microscopic objective; BBS: broadband light source; OSA: optical spectrum analyzer; XYZ Stage: computer controlled three-dimensional translation stage.

The pulse energy is adjustable in the range between 0 and 1mJ by the attenuator (including a half wave plate and a polarizer) and the average on-target laser power is maintained at ~12mW. The fiber with the FBG was mounted on a PC-controlled three-axis translation stage of 40nm resolution, in parallel with the Y-axis. The laser focal spot is located at the centre of the fiber core, along the Y-axis. During the fabrication process, the fiber is shifted by 20μm away from the Y-axis and this position is set to be the jumping-off point. The micro-cavity of the fiber MZI is created by direct fs laser pulse ablation, scanning in parallel with the Y-axis at a speed of 20μm/s, with the scanning distance of 40μm and then returned to the starting point. This formed one scanning cycle.

A CCD camera is used to monitor the micromachining process and the morphology of the cavity. After each scanning cycle, the focal point of the laser beam is moved towards to the fiber core along the X-axis with a step of 400nm before the next cycle started, until the expected transmission spectrum is obtained. The micro-cavity created was cleaned by use of Isopropanol. Fig. 6.3 (a) and (b) are the microscope

images of the achieved structure in top view and cross section. The relatively large surface roughness implies that the laser power used was somewhat too high. A better surface quality could be achieved by optimizing the processing parameters such as pulse energy and scanning speed [12].

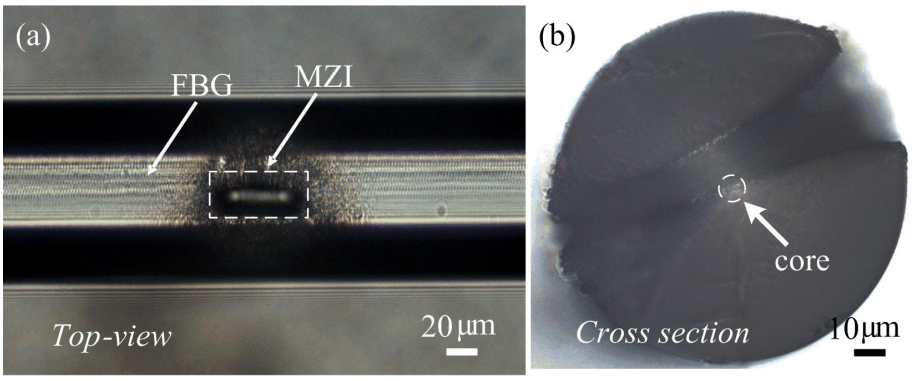


Fig. 6.3 Optical microscope image of the sensor in top-view (a) and cross section (b)

The sensor spectrum was measured in line by a broadband light source ranging from 1270 to 1620nm (Amonics) and an OSA with a resolution of 0.01nm (Yokogama, AQ6319). As shown in Fig. 6.4(a), the resonant wavelength of the FBG is ~1570nm and the reflection is larger than 99%. Fig. 6.4(b) shows the transmission spectrum of the MZI integrated with the FBG. The insertion loss of the device is measured to be around 16dB and this loss mainly comes from laser induced damage on the fiber in the fabrication of MZI.

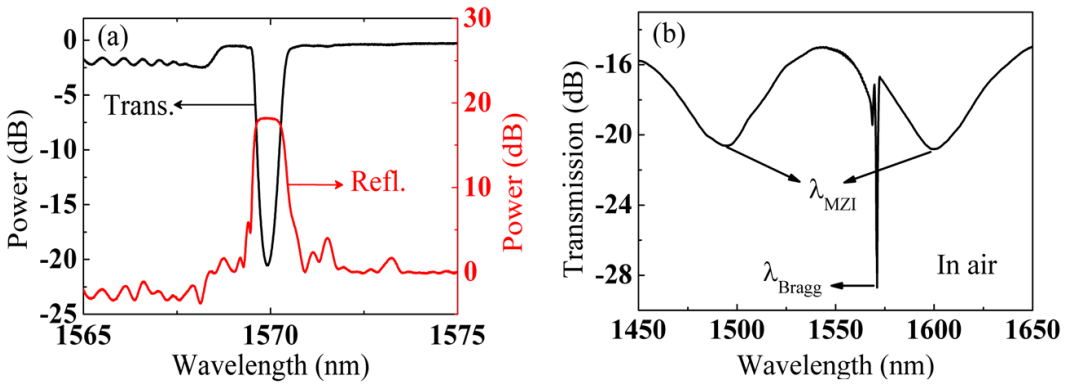


Fig. 6.4 (a) Transmission and reflection spectra of the FBG; (b) Transmission spectrum of the sensor (in air)

## 6.3 Simultaneous Refractive Index and Temperature Measurement

In principle the temperature and RI information can be recovered simultaneously by use of a standard matrix inversion method. The matrix elements can be determined by separately measuring the temperature and RI responses.

The temperature performance was examined by placing the sensor in a tubular oven with temperature control range of 22-100$^{o}$C and resolution of 0.1$^{o}$C. Fig. 6.5 illustrates the spectral response of the sensor with temperature. It is seen from this figure that both $\lambda_{FBG}$ and $\lambda_{m}$ increase linearly with temperature. A linear fitting to the measured data gives the temperature sensitivities of ~12pm/$^{o}$C with a measurement uncertainty of ~ $5\times10^{-2}$ pm/$^{o}$C for $\lambda_{FBG}$ and ~15pm/$^{o}$C with a measurement uncertainty of ~1pm/$^{o}$C for $\lambda_{m}$, respectively.

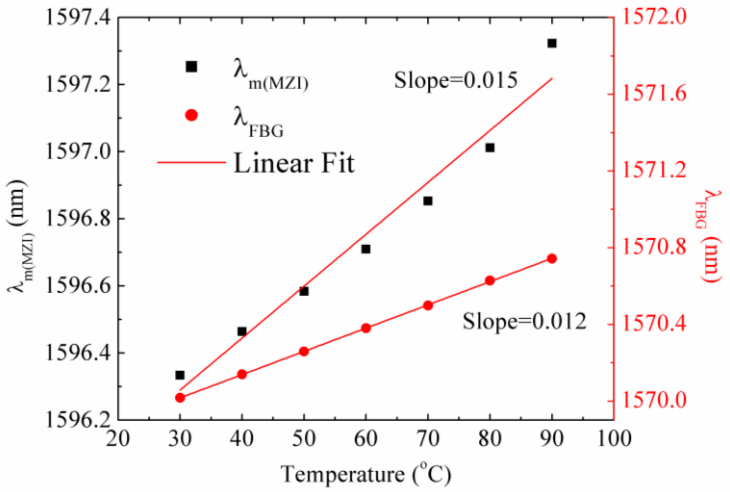


Fig. 6.5 Spectral response of the sensor with temperature

To investigate RI performance, the room temperature of 22$^{o}$C was maintained, and the sensor was sequentially immersed into a set of index matching oils (Cargille

Laboratory) ranging from 1.300 to 1.400 (@489.3nm) with a step of 0.005. After each test, a careful procedure was taken by use of Isopropanol to remove the residual index oil and make it dry in air till the spectrum comes back to the original one in air. Fig. 6.6(a) depicts, with offset, the transmission spectrum of the sensor for different RI values, i.e. n = 1 (air), 1.30, 1.31 and 1.32. It can be clearly observed that an increase of the RI value leads to a 'blue shift' of $\lambda_{m(MZI)}$, while $\lambda_{FBG}$ is essentially unchanged. Fig. 6.6(b) shows that $\lambda_{m(MZI)}$ is extremely sensitive to the RI change with an almost linear response, whereas $\lambda_{FBG}$ remains to be a constant. The sensitivity coefficient obtained is 9148nm/RIU, with a measurement uncertainty of 162nm/RIU, within the range between 1.30 and 1.325. This technique cannot determine the order of interference peak so that it cannot provide absolute RI value but a relative one. Thus, this scheme is more suitable for measurement of known liquids, i.e. salinity of sea water.

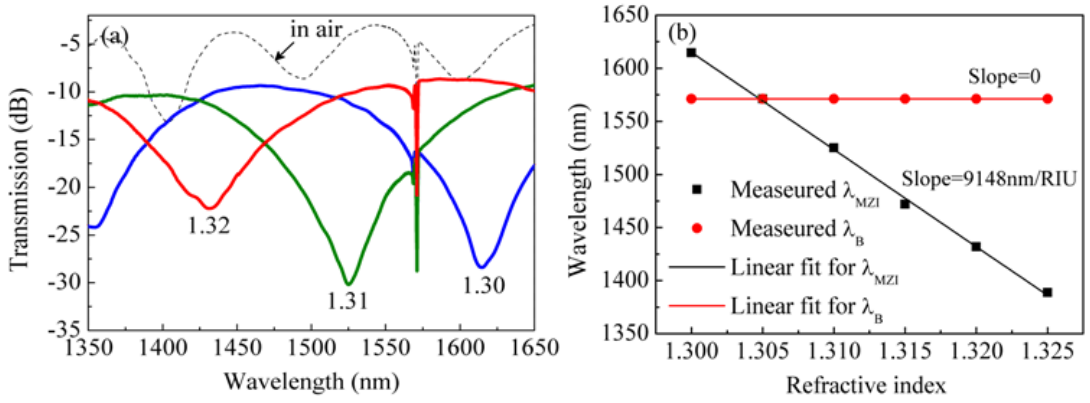


Fig. 6.6 (a) Transmission spectrum of the sensor in different RI (air, 1.30, 1.31 and 1.32); (b) Relationship between $\lambda_{FBG}$, $\lambda_m$ and RI.

According to the two separate temperature and RI measurements, the two equations for $\Delta\lambda_{FBG}$ and $\Delta\lambda_m$ can be obtained:

$$\Delta\lambda_{FBG} = 0.012\Delta T + 0\Delta n \tag{6.6}$$

$$\Delta\lambda_m = 0.015\Delta T - 9148\Delta n \tag{6.7}$$

Thus $\Delta T$ and $\Delta n$ can be determined from the matrix

$$\begin{bmatrix} \Delta T \\ \Delta n \end{bmatrix} = \frac{1}{110}\begin{bmatrix} 9148 & 0 \\ 0.015 & -0.012 \end{bmatrix}\begin{bmatrix} \Delta\lambda_{FBG} \\ \Delta\lambda_{m(MZI)} \end{bmatrix} \tag{6.8}$$

The unit for $\Delta\lambda_{FBG}$ and $\Delta\lambda_{m(MZI)}$ is nanometer, for $\Delta T$ and $\Delta n$ are degree centigrade and RIU, respectively.

The capability of the sensor for simultaneous temperature and RI measurement has also been evaluated. The sensor is immerged in a mini water bath with distilled water which was heated in the tubular oven. The RI of water is a function of temperature, with temperature RI coefficient in the order of $10^{-4}$ /$^{o}$C [13]. The RI of water was calibrated at 30$^{o}$C as 1.33243. Fig. 6.7 presents the results of simultaneous temperature and RI measurement of water, calculated by using matrix method, which is in a good agreement with that reported in Ref. [13]. However the condition number of the 2-by-2 sensitivity matrix is $\sim 7\times10^{5}$ that is a large value in conventional dual-parameter sensors and this means the sensor is sensitive to inaccuracies in experimental measurements [14, 15]. To eliminate the effect of matrix being ill conditioned, some algorithms in data processing are effective to largely reduce the error i.e. pretreatment of matrix and residual iteration method.

In experiment the OSA was working at the resolution of 0.01nm therefore the temperature and RI resolution can be estimated to be around 0.8$^{o}$C and $3.2\times10^{-4}$ RIU. We assume the primary measurement error comes from the accuracies in determining wavelengths. The standard deviation in detecting wavelength is estimated to be $6.25\times10^{-3}$ nm for $\lambda_{FBG}$ and 0.98nm for $\lambda_{m(MZI)}$ due to the different FWHM. Therefore the transferred errors in $\Delta T$ and $\Delta n$ are calculated to be

approximately 0.5°C and $2.4\times10^{-4}$ RIU [15], which are acceptable in practical use.

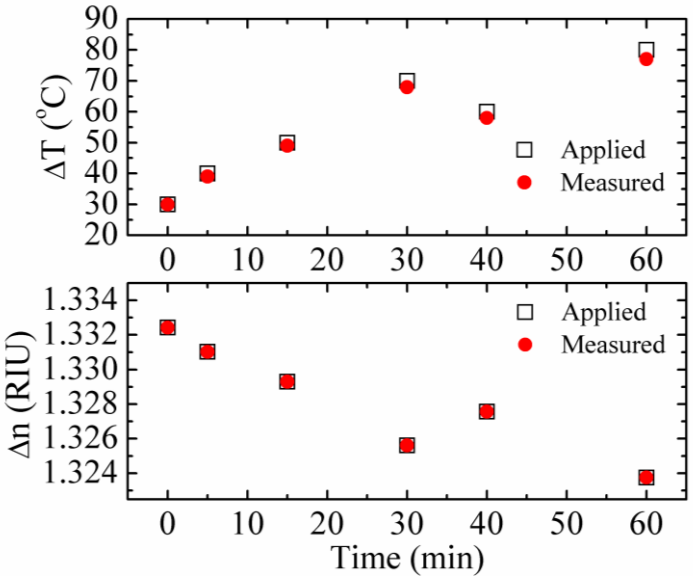


Fig. 6.7 Results of simultaneous RI and temperature measurement.

Comparing with the existed dual-parameter (RI / temperature) sensors, this optical sensor is all-in-fiber structure without external element so that it is convenient to connect it with the other optical fiber system with negligible connection loss. The ultra-compact size of the MZI cavity guarantees a precise sensing location. What is more, the sensor exhibits an ultrahigh RI sensitivity. But the sensor is easily cracked because the cavity of MZI destroys fiber structure. It is necessary to make an encapsulation of the sensor in practical use. In addition, this sensor cannot provide absolute RI value but a relative one. Thus, this scheme is more suitable for measurement of known liquids.

## 6.4 Summary

We have demonstrated a novel optical fiber sensor based on an MZI embedded in an FBG which is used for simultaneous RI and temperature measurement. For the MZI one arm contains a micro-cavity created by fs laser micromachining to remove part

of the fiber core and cladding and the other remains to be confined to the fiber core. The RI sensitivity of 9148nm/RIU is obtained within the range between 1.30 and 1.325, and the temperature sensitivity achieved is 12pm/$^{o}$C, ranging from 30 to 90$^{o}$C. The developed sensor system is suitable for extremely sensitive, precisely localized and highly reliable RI measurement.

# Reference

[1] C. L. Zhao, X. F. Yang, M. S. Demokan, and W. Jin, "Simultaneous Temperature and Refractive index Measurements Using a 3o Slanted Multimode Fibre Bragg grating," *J. Lightwave Technol.*, vol. 24, pp. 879-883, (2006).

[2] O. Fraz ão, B. V. Marques, P. Jorge, J. M. Baptista, and J. L. Santos, "High birefringence D-type fibre loop mirror used as refractometer," *Sens. Actuator B-Chem.*, vol. 135, pp. 108-111, (2008).

[3] Y. J. Rao, M. Deng, D. W. Duan, and T. Zhu, "In-line fibre Fabry-Perot refractive-index tip sensor based on endlessly photonic crystal fibre," *Sens. Actuator A-Phys.*, vol. 148, pp. 33-38, (2008).

[4] X. W. Shu, B. A. L. Gwandu, Y. Liu, L. Zhang, and I. Bennion, "Sampled fibre Bragg grating for simultaneous refractive-index and temperature measurement," *Opt. Lett.*, vol. 26, pp. 774-776, (2001).

[5] A. P. Zhang, L. Y. Shao, J. F. Ding, and S. L. He, "Sandwiched Long-Period Gratings for simultaneous Measurement of Refractive Index and Temperature," *Photon. Technol. Lett.*, vol. 17, pp. 2397-2399, (2005).

[6] L. Y. Shao, A. P. Zhang, W. S. Liu, H. Y. Fu, and S. L. He, "Optical Refractive Index Sensor Based on Dual Fibre-Bragg Gratings Interposed With a Multimode-Fibre Taper," *Photon. Technol. Lett.*, vol. 19, pp. 30-32, (2007).

[7] L. Q. Men, P. Lu, and Q. Y. Chen, "A multiplexed fibre Bragg grating sensor for simultaneous salinity and temperature measurement," *J. Appl. Phys.*, vol. 103, pp. 053107, (2008).

[8] Y. J. Rao, M. Deng, D. W. Duan, X. C. Yang, T. Zhu, and G. H. Cheng, "Micro Fabry-Perot interferometers in silica fibers machined by femtosecond laser," *Opt. Express*, vol. 15, pp. 14123-14128, (2007).

[9] M. Park, S. Lee, W. Ha, J. Kim, Y. Jung, W. Shin, I. Sohn, and K. Oh, "All-fiber micro air cavity Mach-Zehnder interferometer formed by femtosecond laser micromachining," *OECC/ACOFT,* Sydney, (2008).

[10] C. Grillet, P. Domachuk, V. Ta'eed, E. Mägi, J. A. Bolger, B. J. Eggleton, L. E. Rodd, and J. C. White, "Compact tunable microfluidic interferometer," *Opt. Express,* vol. 12, pp. 5440-5447, (2004).

[11] Y. Wang, M. W. Yang, D. N. Wang, S. J. Liu, and P. X. Lu, "Fibre in-line Mach-Zehnder interferometer fabricated by femtosecond laser micromachining for refractive index measurement with high sensitivity," *J. Opt. Soc. Am. B-Opt. Phys.*, vol. 27, pp. 370-374, (2010).

[12] I. M. White and X. D. Fan, "On the performance quantification of resonator refractive index sensors," *Opt. Express,* vol. 16, pp. 1020-1028, (2008).

[13] P. Schiebener, J. Straub, J. M. H. Levelt Sengers, and J. S. Gallagher, "Refractive index of water and steam as function of wavelength, temperature and density," *J. Phys. Chem. Ref. Data*, vol. 19, pp. 677-717, (1990).

[14] P. Sivanesan, J. S. Sirkis, Y. Murata, and S. G. Buckley, "Optimal wavelength pair selection and accuracy analysis of dual fibre grating sensors for simultaneously measuring strain and temperature," *Opt. Eng.*, vol. 41, pp. 2456-2463, (2002).

[15] W. Jin, W. C. Michie, G. Thursby, M. Konstantaki, and B. Culshaw, "Simultaneous measurement of strain and temperature: error analysis," *Opt. Eng.*, vol. 36, pp. 598-609, (1997).

# Chapter 7

# Conclusion and Further Work

## 7.1 Conclusion

In this thesis, the results of investigation on a number of fiber grating based sensors have been reported.

Different from UV-laser induced index change, modification of dielectrics with fs laser pulses is resulting from multi-photon ionization. The nature of multiphoton ionization makes fs laser be able to inscribe FBGs in a broader range of optical fibers than UV writing process. UV-laser method is limited to photosensitive fiber core material, which is unsuitable for high power applications. This limitation can be overcome by using fs laser pulses for grating inscription. Based on ultrahigh peak power of fs laser pulses, damaged FBGs can be easily achieved and these gratings show a much better thermal stability than conventional UV-gratings. However, due to the high threshold intensity of the nonlinear absorption, the index change is confined to the confocal region of the focused fs laser beam. For the inscription of FBG, careful alignment of the writing beam is mandatory.

Two types of FBGs can be achieved by use of fs laser irradiation. Type I-IR is formed through an intermediate level of electron generation, below that necessary to strong ionize the medium. The induced index change has temperature stability similar to that of UV-written Type I with a difference which can be explained by different categories of the formed colour centers. Type II-IR appears to result from a damage process similar to what would be expected from a highly ionized absorbing

medium. These gratings have high temperature stability that is similar to that of UV-written Type II.

FBGs inscribed in SMFs by fs laser pulses have been used as the ultrahigh temperature sensors. The morphology and thermal stability of these gratings with different fabrication conditions have been investigated in detail, building on and developing from work published in the literature. The excellent thermal stability the $H_2$-free Type II-IR grating that is reported makes it ideally suited to very high temperature monitoring i.e. furnace temperature control and in other situations where extreme and often prolonged temperatures are experienced e.g. in engine testing and monitoring. However, when considering the design of a strain sensor, the Type I-IR grating is better suited than the damage grating due to its greater tensile strength.

We have investigated the effect of optical heating on optical fibers that are used for optical fiber sensor systems. The experimental results show that the temporal thermal response of this grating is $230 \pm 25$ms in the heating phase and $275 \pm 25$ms in the cooling phase, which is independent of the heating power and the heating direction. Finally, the simulation results obtained are somewhat different from the experimental data and the possible error sources were analyzed in detail. The model produced has been validated and could be used to predict the temporal performance of a range of fibers of different diameters (and masses) for various sensor applications.

We have studied the FBGs and LPGs those are inscribed in AS-PBGF by fs laser pulses irradiation. The AS-PBGF is not a single mode fiber but supports two core modes which are $LP_{01}$ and $LP_{11}$ core modes. Hence, in the fabrication of FBGs, there are two Bragg reflection peaks being observed in the reflection spectrum. The longer

wavelength is due to the coupling between the forward $LP_{01}$ core mode and the backward $LP_{01}$ core mode while the other one is resulting from the coupling between the forward $LP_{11}$ core mode and the backward $LP_{11}$ core mode. Later LPGs have been fabricated based on the coupling from $LP_{01}$ core mode to $LP_{11}$ core mode without cladding mode coupling. The LPGs developed exhibit interesting properties such as large PDL, low sensitivity to temperature and curvature, insensitivity to external RI and high sensitivity to tensile strain, and have high potentials in tunable spectral filters and optical fiber sensors with reduced cross-sensitivity.

We have also fabricated a novel FBG in MF by fs laser pulse irradiation. Such an FBG can be directly exposed to the surrounding medium without etching treatment of the fiber and has high RI sensitivity especially when the higher order of fiber mode is utilized. The maximum sensitivity obtained for the first order mode is ~231.4nm/RIU, at the RI value of 1.44, when the fiber diameter is ~2μm. The proposed RI sensor based on the different-order mode reflection of an MF FBG owns compact size, high sensitivity, low cost and great multiplexing capability, as well as the convenience of sensing head operating. However, mechanical strength of this grating is weak and easily cracked. Its optical performance quickly degrades due to surface scattering from dust particles and from cracks induced by water vapour. An effective encapsulation method is needed to overcome these key impediments.

Due to the strong evanescent field of MFs, we have constructed a simple, compact and robust RI sensor based on a pair of twisted MFs. The spectral characteristics of the device have been investigated both theoretically and experimentally. The highest sensitivity is obtained for the MFs with the diameter of ~4.2μm is 2377nm/RIU, at the RI value of 1.3680. A further sensitivity improvement to 2735nm/RIU can be achieved when the diameter of MFs is reduced to ~2.8μm. This design is featured

with easy fabrication, compact size and high RI sensitivity. However, the sensor cannot provide absolute RI value but a relative one. Bare MFs are easily contaminated by environment and the increased propagation loss from each RI test will dramatically shorten its lifetime. Moreover, transmission spectrum of the sensor is complicated and contains many peaks that will involve certain difficulties for demodulation in practical system.

To overcome the temperature cross-sensitivity in RI sensing, a novel sensor configuration based on a fiber in-line MZI embedded in an FBG has been developed for simultaneous RI and temperature measurement. The RI sensitivity of 9148nm/RIU is obtained within the range between 1.30 and 1.325, and the temperature sensitivity achieved is 12pm/$^{o}$C, ranging from 30 to 90$^{o}$C. The developed sensor system is all-in-fiber structure without external element and is convenient to connect it to other fiber system with negligible connection loss. The ultra-compact size of the MZI cavity guarantees a precise sensing location and the sensor exhibits an ultrahigh RI sensitivity. However, the sensor is easily cracked and requires an encapsulation of the structure in practical use. In addition, this sensor cannot provide absolute RI value but a relative one.

## 7.2 Further Work

During the Ph. D. study, some promising directions have been identified and could be followed up in a future project.

Fiber gratings have been successfully fabricated in the AS-PBGF with the help of the all-solid fiber structure. However, it is still difficult to directly inscribe fiber gratings in the all silica PCF with the air-hole cladding because the total flux at the fiber core is substantially reduced due to air-hole scattering of light at various air-interfaces.

Further research will be carried out in the fabrication of FBGs in the air-hole PCF by means of filling the air holes with some specified liquid, which has a similar RI value with silica, to eliminate light scattering loss. After grating inscription, the filling liquid can be totally removed by high temperature evaporation. The FBGs achieved in all silica PCF will be a promising candidate for high temperature applications.

We have fabricated FBGs in the common MFs which are taper-drawn from standard optical fiber. But the MFs are typically not Hi-Bi and therefore have no capability of maintaining the polarization state that is a crucial factor to determine the stability of phase sensitive fiber devices. Recently Hi-Bi MFs have been achieved in experiment and the birefringence of the MFs is extraordinarily high. In the next step we plan to inscribe FBGs in the Hi-Bi MFs by use of fs laser irradiation. Such FBGs would be more valuable and attractive in optical fiber sensors, precision optical instruments and optical fiber communication systems.

Another issue that values further investigation is to develop more complicated fiber devices based on the FBGs inscribed in MFs. For example, The MF based FBG is to be incorporated into the MF based Sagnac interferometer to form an ultracompact comb filter. The Sagnac interferometer can be assembled by twisting the MF with an FBG into a loop and the FBG is required to be asymmetrically located in the loop. The proposed comb filter, which is totally constructed by MF and MF based devices, will be promising in the miniaturization of optical fiber systems.

The MF based FBGs have demonstrated a great capability in measuring the RI of liquids. In the next stage we want to combine thin film coating technique with the MF based FBGs to develop highly sensitive gas sensor. Now hydrogen gas is fast

becoming the most important player in solving future energy problems. Generating power from hydrogen in industrial and household applications is rapidly expanding and increasing in popularity. We plan to fabricate a novel hydrogen sensor by coating $Pd/WO_3$ thin film, which has a good response to hydrogen concentration, on the surface of the MF based FBG. The RI change of thin film will affect the effective RI of the propagation modes in the MF resulting in the change of Bragg condition. The combination of materials science with MFs would be meaningful in micro and nano photonics.